

Marie Eugenie Edvardsen

# Crevice corrosion of AISI 316L and 22Cr - the effect of temperature, chloride concentration, pH and oxygen content

Master's thesis in Chemical Engineering and Biotechnology

Supervisor: Andreas Erbe

Co-supervisors: Roy Johnsen, Jan Ivar Skar and Sven Morten Hesjevik

June 2020





Marie Eugenie Edvardsen

# **Crevice corrosion of AISI 316L and 22Cr - the effect of temperature, chloride concentration, pH and oxygen content**

Master's thesis in Chemical Engineering and Biotechnology

Supervisor: Andreas Erbe

Co-supervisors: Roy Johnsen, Jan Ivar Skar and Sven Morten Hesjevik

June 2020

Norwegian University of Science and Technology

Faculty of Natural Sciences

Department of Materials Science and Engineering



Norwegian University of  
Science and Technology



# Preface

This master thesis was written at the Norwegian University of Science and Technology (NTNU), at the Department of Materials Science and Engineering as a part of the integrated master's degree Chemical Engineering and Biotechnology. The work was performed in collaboration with Equinor. The project was supervised by Professor Roy Johnsen and Professor Andreas Erbe from NTNU, and Jan Ivar Skar and Sven Morten Hesjevik from Equinor.

The experimental work has been performed at the Department of Mechanical and Industrial Engineering at NTNU. The work has been performed by the author, in accordance with rules and regulations at NTNU. The data analysis conducted in Unscrambler and Design-Expert was performed by the author together with Marion Duparc from Equinor.

*Marie E. Edvardsen*

---

Marie Eugenie Edvardsen  
29.06.2020  
Trondheim, Norway



## Acknowledgements

I would like to thank my supervisor, Professor Andreas Erbe and co-supervisors, Professor Roy Johnsen, Jan Ivar Skar and Sven Morten Hesjevik for all the guidance provided. I am particularly grateful for the excellent guidance provided by Professor Roy Johnsen. His enthusiasm and availability during my master thesis have been highly appreciated. I would also like to thank Cristian Torres for the assistance both inside and outside the laboratory, whenever needed. I am grateful as well for the guidance and help with the use of Unscrambler and Design-Expert provided by Marion Duparc.

I am also grateful for all the friends I have made throughout my studies. Finally, I would like to thank my family for all the support and encouragement they have given me.



# Abstract

Corrosion resistant alloys, such as stainless steels are often used in offshore installations due to their high resistance towards general corrosion. Stainless steels are however susceptible to localized corrosion, such as crevice corrosion at specific conditions. Crevice corrosion resistance is affected by various environmental parameters, such as temperature, chloride concentration, pH and oxygen content. Oxygen ingress in the process and production systems can be damaging for corrosion resistant alloys and an oxygen application limit of 10 ppbw is used as a general practice. Recent research has indicated that the oxygen limit may be higher. An increased limit would be beneficial in terms of economy, operation and material selection.

The aim of this thesis is to investigate the effect of different environmental parameters on crevice corrosion of AISI 316L stainless steel and 22% Cr duplex stainless steel in a low oxygen environment. Both materials are considered to be important stainless steels and are widely used. A review of literature on the effect of different environmental parameters on crevice corrosion of stainless steels and the oxygen limit were conducted, in addition to experimental work.

The experimental work included recording of anodic cyclic potentiodynamic polarization curves and open circuit potential measurements. By using ASTM G61 standard, anodic cyclic potentiodynamic polarization curves at different temperatures, chloride concentrations and pH were recorded. Both materials were tested in electrolytes with 600 ppmw, 5000 ppmw and 120 000 ppmw chloride at both 30 °C and 95 °C in the pH region 4.1 - 8.5. The results showed that the crevice corrosion potential and the repassivation potential of both the materials decreased with increasing chloride concentration and temperature. The crevice corrosion resistance of both AISI 316L stainless steel and 22% Cr duplex stainless steel are lower at higher temperatures and chloride concentrations. Higher chloride concentration and temperature made it more difficult for the surface to repassivate as well. 22% Cr duplex stainless steel showed the highest corrosion resistance of the two materials. pH had little effect on the crevice corrosion potential and repassivation potential in the tested pH range. The open circuit potential increased with increasing oxygen content and decreased with increasing temperature. Both materials had an oxygen application limit of < 10 ppbw oxygen in solution with 120 000 ppmw chloride at 95 °C. Open circuit potential measurements with different oxygen contents should be conducted to establish oxygen application limits at the other test conditions.





# Sammendrag

Korrosjonsresistente legeringer, som for eksempel rustfrie stål, blir ofte brukt i offshore-installasjoner på grunn av deres høye motstand mot generell korrosjon. Rustfrie stål er imidlertid utsatt for lokal korrosjon, som spaltekorrosjon under spesifikke forhold. Spaltekorrosjonsmotstand påvirkes av forskjellige miljøparametere, som temperatur, kloridkonsentrasjon, pH og oksygeninnhold. Oksygeninntrengning i prosess- og produksjonssystemer kan være skadelig for korrosjonsresistente legeringer, og en oksygenapplikasjonsgrense på 10 ppbw brukes som en generell praksis. Nyere forskning har indikert at oksygen grensen kan være høyere. En høyere grense vil være lønnsomt med tanke på økonomi, drift og materialvalg.

Målet med denne avhandlingen er å undersøke effekten av forskjellige miljøparametere på spaltekorrosjon av AISI 316L rustfritt stål og 22% Cr dupleks rustfritt stål i et miljø med lite oksygen. Begge materialene anses å være viktige rustfrie stål og er mye brukt. En gjennomgang av litteratur om effekten av forskjellige miljøparametere på spaltekorrosjon av rustfritt stål og oksygen grensen ble gjennomført, i tillegg til eksperimentelt arbeid.

Det eksperimentelle arbeidet inkluderte opptak av anodisk syklisk potensiodynamisk polariseringskurver og målinger av åpen krets potensialet. Ved å bruke ASTM G61-standard ble anodisk syklisk potensiodynamisk polariseringskurver ved forskjellige temperaturer, kloridkonsentrasjoner og pH tatt opp. Begge materialene ble testet i elektrolytter med 600 ppmw, 5000 ppmw og 120 000 ppmw klorid ved både 30 °C og 95 °C i pH-området 4.1 - 8.5. Resultatene viste at spaltekorrosjonspotensialet og repassiveringspotensialet til begge materialene avtok med økende kloridkonsentrasjon og temperatur. Spaltekorrosjonsmotstanden til både AISI 316L rustfritt stål og 22% Cr dupleks rustfritt stål er lavere ved høyere temperaturer og kloridkonsentrasjoner. Høyere kloridkonsentrasjon og temperatur gjorde det også vanskeligere for overflaten å repassivere. 22 % Cr dupleks rustfritt stål viste den høyeste korrosjonsmotstanden av de to materialene. pH hadde liten effekt på spaltekorrosjonspotensialet og repassiveringspotensialet i det testede pH-området. Åpen krets potensialet økte med økende oksygeninnhold og avtok med økende temperatur. Begge materialene hadde en oksygen grense på < 10 ppbw oksygen i løsning med 120 000 ppmw klorid ved 95 °C. Åpen krets potensial målinger med ulike oksygen innhold bør gjennomføres for å etablere oksygenapplikasjonsgrenser ved de andre testforholdene.



# Table of Contents

|   |           |
|---|-----------|
| Preface   | i         |
| Acknowledgements  | iii       |
| Abstract  | v         |
| Sammendrag  | vii       |
| Table of Contents   | ix        |
| List of Tables  | xiii      |
| List of Figures   | xvii      |
| Abbreviations   | xxi       |
| Symbol list   | xxiii     |
| <b>1 Introduction</b>                                       | <b>1</b>  |
| 1.1 Background . . . . .                                    | 1         |
| 1.2 Objective . . . . .                                     | 2         |
| <b>2 Theoretical background</b>                             | <b>3</b>  |
| 2.1 Austenitic and duplex stainless steels . . . . .        | 3         |
| 2.1.1 Metallurgy . . . . .                                  | 3         |
| 2.1.2 Microstructure . . . . .                              | 4         |
| 2.1.3 Composition and alloying elements . . . . .           | 4         |
| 2.2 Passive film . . . . .                                  | 6         |
| 2.3 Crevice corrosion . . . . .                             | 8         |
| 2.3.1 Crevice corrosion mechanism . . . . .                 | 9         |
| 2.4 Parameters affecting crevice corrosion . . . . .        | 9         |
| 2.4.1 Temperature . . . . .                                 | 10        |
| 2.4.2 Chloride content . . . . .                            | 11        |
| 2.4.3 pH . . . . .  | 11        |
| 2.4.4 Fluid flow . . . . .                                  | 12        |
| 2.5 Produced water systems . . . . .                        | 13        |
| 2.6 Test methods for crevice corrosion . . . . .            | 13        |
| 2.6.1 Cyclic potentiodynamic polarization curves . . . . .  | 14        |
| 2.7 Design of experiments . . . . .                         | 17        |
| <b>3 State of the art</b>                                   | <b>21</b> |
| 3.1 Effect of oxygen . . . . .                              | 21        |
| 3.1.1 Alteration of the passive film . . . . .              | 22        |
| 3.1.2 Oxygen reduction reaction . . . . .                   | 22        |
| 3.2 Oxygen application limit . . . . .                      | 23        |
| 3.3 OCP measurements at different oxygen contents . . . . . | 24        |
| <b>4 Experimental</b>                                       | <b>25</b> |

|          |   |           |
|----------|---|-----------|
| 4.1      | Test materials and material preparation . . . . . | 25        |
| 4.2      | ASTM G61 . . . . .                                | 27        |
| 4.2.1    | Chemicals and test conditions . . . . .           | 27        |
| 4.2.2    | Crevice assembly . . . . .                        | 28        |
| 4.2.3    | Procedure and apertures . . . . .                 | 28        |
| 4.2.4    | Differences between the two setups . . . . .      | 31        |
| 4.3      | Open circuit potential measurements . . . . .     | 31        |
| 4.3.1    | Chemicals and test conditions . . . . .           | 31        |
| 4.3.2    | Procedure and apertures . . . . .                 | 32        |
| 4.4      | Infinite Focus Microscope . . . . .               | 33        |
| <b>5</b> | <b>Results</b>                                    | <b>35</b> |
| 5.1      | Effect of temperature . . . . .                   | 35        |
| 5.1.1    | AISI 316L stainless steel . . . . .               | 35        |
| 5.1.2    | 22% Cr duplex stainless steel . . . . .           | 39        |
| 5.2      | Effect of chloride concentration . . . . .        | 42        |
| 5.2.1    | AISI 316L stainless steel . . . . .               | 42        |
| 5.2.2    | 22% Cr duplex stainless steel . . . . .           | 46        |
| 5.3      | Effect of pH . . . . .                            | 50        |
| 5.3.1    | AISI 316L stainless steel . . . . .               | 51        |
| 5.3.2    | 22% Cr duplex stainless steel . . . . .           | 55        |
| 5.4      | Surface characterization . . . . .                | 60        |
| 5.4.1    | AISI 316L stainless steel . . . . .               | 60        |
| 5.4.2    | 22% Cr duplex stainless steel . . . . .           | 64        |
| 5.5      | OCP measurements . . . . .                        | 68        |
| <b>6</b> | <b>Discussion</b>                                 | <b>73</b> |
| 6.1      | Effect of temperature . . . . .                   | 73        |
| 6.1.1    | AISI 316L stainless steel . . . . .               | 73        |
| 6.1.2    | 22% Cr duplex stainless steel . . . . .           | 74        |
| 6.2      | Effect of chloride concentration . . . . .        | 75        |
| 6.2.1    | AISI 316L stainless steel . . . . .               | 75        |
| 6.2.2    | 22% Cr duplex stainless steel . . . . .           | 77        |
| 6.3      | Effect of pH . . . . .                            | 79        |
| 6.3.1    | AISI 316L stainless steel . . . . .               | 79        |
| 6.3.2    | 22% Cr duplex stainless steel . . . . .           | 80        |
| 6.4      | Data analysis by DOE . . . . .                    | 81        |
| 6.5      | Surface characterization . . . . .                | 81        |
| 6.5.1    | AISI 316L stainless steel . . . . .               | 81        |
| 6.5.2    | 22% Cr duplex stainless steel . . . . .           | 82        |
| 6.6      | Material comparison . . . . .                     | 82        |
| 6.7      | OCP measurements . . . . .                        | 83        |
| <b>7</b> | <b>Conclusion</b>                                 | <b>87</b> |
| <b>8</b> | <b>Further work</b>                               | <b>89</b> |
| <b>A</b> | <b>Appendix</b>                                   | <b>97</b> |

|     |   |    |
|-----|---|----|
| A.1 | Material certificate AISI 316L samples . . . . .  | 97 |
| A.2 | Material certificate 22% Cr DSS samples . . . . . | 98 |
| A.3 | Percentage crevices . . . . .                     | 99 |



## List of Tables

|            |   |    |
|------------|---|----|
| Table 2.1  | Alloy composition in wt% for AISI 316L stainless steel (UNS S31603).  | 5  |
| Table 2.2  | Alloy composition in wt% for 22% Cr duplex stainless steel (UNS S32205).  | 5  |
| Table 2.3  | Water conditions for produced water from oil and gas platforms in the North Sea.  | 13 |
| Table 4.1  | Chemical composition of AISI 316L stainless steel [wt%] used in the experiments.  | 25 |
| Table 4.2  | Chemical composition of 22% Cr duplex stainless steel [wt%] used in the experiments.  | 25 |
| Table 4.3  | Calculated $PRE_N$ values for the test materials.   | 26 |
| Table 4.4  | Test conditions used to record the anodic CPP curves.   | 28 |
| Table 4.5  | Test conditions used to measure OCP.  | 32 |
| Table 5.1  | Parameters obtained from the CPP curves for 316L recorded in electrolytes with 600 ppm chloride and purged with $N_2$ at different temperatures, all potentials are vs. Ag/AgCl.      | 36 |
| Table 5.2  | Parameters obtained from the CPP curves for 316L recorded in electrolytes with 5000 ppm chloride and purged with $N_2$ at different temperatures, all potentials are vs. Ag/AgCl.     | 36 |
| Table 5.3  | Parameters obtained from the CPP curves for 316L recorded in electrolytes with 120 000 ppm chloride and purged with $N_2$ at different temperatures, all potentials are vs. Ag/AgCl.  | 36 |
| Table 5.4  | Parameters obtained from the CPP curves for 316L recorded in electrolytes with 600 ppm chloride and purged with $CO_2$ at different temperatures, all potentials are vs. Ag/AgCl.     | 38 |
| Table 5.5  | Parameters obtained from the CPP curves for 316L recorded in electrolytes with 120 000 ppm chloride and purged with $CO_2$ at different temperatures, all potentials are vs. Ag/AgCl. | 38 |
| Table 5.6  | Parameters obtained from the CPP curves for DSS recorded in electrolytes with 600 ppm chloride and purged with $N_2$ at different temperatures, all potentials are vs. Ag/AgCl.       | 41 |
| Table 5.7  | Parameters obtained from the CPP curves for DSS recorded in electrolytes with 600 ppm chloride and purged with $CO_2$ at different temperatures, all potentials are vs. Ag/AgCl.      | 41 |
| Table 5.8  | Parameters obtained from the CPP curves for DSS recorded in electrolytes with 120 000 ppm chloride and purged with $N_2$ at different temperatures, all potentials are vs. Ag/AgCl.   | 41 |
| Table 5.9  | Parameters obtained from the CPP curves for DSS recorded in electrolytes with 120 000 ppm chloride and purged with $CO_2$ at different temperatures, all potentials are vs. Ag/AgCl.  | 41 |
| Table 5.10 | Parameters obtained from the CPP curves for 316L recorded in electrolytes purged with $N_2$ at 30 °C with different chloride concentrations, all potentials are vs. Ag/AgCl.          | 43 |
| Table 5.11 | Parameters obtained from the CPP curves for 316L recorded in electrolytes purged with $N_2$ at 95 °C with different chloride concentrations, all potentials are vs. Ag/AgCl.          | 43 |

|   |    |
|---|----|
| Table 5.12 Parameters obtained from the CPP curves for 316L recorded in electrolytes purged with CO <sub>2</sub> at 30 °C with different chloride concentrations, all potentials are vs. Ag/AgCl. . . . . | 45 |
| Table 5.13 Parameters obtained from the CPP curves for 316L recorded in solution purged with CO <sub>2</sub> at 95 °C with different chloride concentrations, all potentials are vs. Ag/AgCl. . . . .     | 45 |
| Table 5.14 Parameters obtained from the CPP curves for DSS recorded in electrolytes purged with N <sub>2</sub> at 30 °C with different chloride concentrations, all potentials are vs. Ag/AgCl. . . . .   | 48 |
| Table 5.15 Parameters obtained from the CPP curves for DSS recorded in electrolytes purged with CO <sub>2</sub> at 30 °C with different chloride concentrations, all potentials are vs. Ag/AgCl. . . . .  | 49 |
| Table 5.16 Parameters obtained from the CPP curves for DSS recorded in electrolytes purged with N <sub>2</sub> at 95 °C with different chloride concentrations, all potentials are vs. Ag/AgCl. . . . .   | 49 |
| Table 5.17 Parameters obtained from the CPP curves for DSS recorded in electrolytes purged with CO <sub>2</sub> at 95 °C with different chloride concentrations, all potentials are vs. Ag/AgCl. . . . .  | 49 |
| Table 5.18 Parameters obtained from the CPP curves for 316L recorded in electrolytes with 600 ppm chloride at 30 °C with different pH, all potentials are vs. Ag/AgCl. . . . .                            | 53 |
| Table 5.19 Parameters obtained from the CPP curves for 316L recorded in electrolytes with 120 000 ppm chloride at 30 °C with different pH, all potentials are vs. Ag/AgCl. . . . .                        | 54 |
| Table 5.20 Parameters obtained from the CPP curves for 316L recorded in electrolytes with 600 ppm chloride at 95 °C with different pH, all potentials are vs. Ag/AgCl. . . . .                            | 54 |
| Table 5.21 Parameters obtained from the CPP curves for 316L recorded in electrolytes with 5000 ppm chloride at 95 °C with different pH, all potentials are vs. Ag/AgCl. . . . .                           | 54 |
| Table 5.22 Parameters obtained from the CPP curves for 316L recorded in electrolytes with 120 000 ppm chloride at 95 °C with different pH, all potentials are vs. Ag/AgCl. . . . .                        | 55 |
| Table 5.23 Parameters obtained from the CPP curves for DSS recorded in electrolytes with 600 ppm chloride at 30 °C with different pH, all potentials are vs. Ag/AgCl. . . . .                             | 58 |
| Table 5.24 Parameters obtained from the CPP curves for DSS recorded in electrolytes with 120 000 ppm chloride at 30 °C with different pH, all potentials are vs. Ag/AgCl. . . . .                         | 58 |
| Table 5.25 Parameters obtained from the CPP curves for DSS recorded in electrolytes with 600 ppm chloride at 95 °C and different pH-values, all potentials are vs. Ag/AgCl. . . . .                       | 59 |
| Table 5.26 Parameters obtained from the CPP curves for DSS recorded in electrolytes with 5000 ppm chloride at 95 °C and different pH-values, all potentials are vs. Ag/AgCl. . . . .                      | 59 |



|   |    |
|---|----|
| Table 5.27 Parameters obtained from the CPP curves for DSS recorded in electrolytes with 120 000 ppm chloride at 95 °C and different pH-values, all potentials are vs. Ag/AgCl. . . . . | 59 |
| Table 5.28 Percentage crevices on the 316L sample surfaces, at each test condition.   | 61 |
| Table 5.29 Average weight loss for 316L samples after the anodic CPP measurements at the different tests conditions. . . . .  | 64 |
| Table 5.30 Percentage crevices on the DSS sample surfaces, at each test condition.  | 65 |
| Table 5.31 Average weight loss for DSS samples after the anodic CPP measurements at the different tests conditions. . . . .   | 68 |



# List of Figures

|            |  |    |
|------------|--|----|
| Figure 2.1 | Microstructure of Fe-22Cr-5.5Ni-3Mo-0.15N DSS etched in 40% NaOH, made of a ferrite matrix (dark phase) with austenite islands (light phase). . . . .  | 4  |
| Figure 2.2 | Illustration of the relationship between the passive film, corrosion resistance and composition of the alloy. . . . .  | 6  |
| Figure 2.3 | Composition of the passive film often created on austenitic stainless steel. . . . .   | 7  |
| Figure 2.4 | The chemistry that develops inside the crevice during crevice corrosion. . . . .   | 8  |
| Figure 2.5 | Example of how the potentiodynamic polarization curves to stainless steels are influenced by different environmental parameters. . . . .   | 10 |
| Figure 2.6 | An example of a typical cyclic potentiodynamic polarization curve for pitting corrosion for a sample exhibiting protection potential. . . . .  | 14 |
| Figure 2.7 | $E_{crev}$ is determined as the potential at the inflection point, illustrated as $E_P$ . . . . .  | 16 |
| Figure 2.8 | $E_{rep}$ is determined as the potential where hysteresis loop closes, illustrated as $E_{RP}$ . . . . .   | 16 |
| Figure 2.9 | Schematic illustration of the CCD method, including the different points; factorial (F), center (C) and start (S) points. . . . .  | 18 |
| Figure 3.1 | OCP development as a function of dissolved oxygen (DO) content, for stainless steel in solution with 19 000 ppm chloride and pH 7.5 at 45 °C. . . . .  | 24 |
| Figure 4.1 | 316L samples used in the experiments . . . . .   | 26 |
| Figure 4.2 | DSS samples used in the experiments . . . . .  | 26 |
| Figure 4.3 | Illustration of the DSMCA. . . . .   | 29 |
| Figure 4.4 | Schematic illustration of setup 2 used to record anodic CPP curves, made by the author. . . . .  | 30 |
| Figure 4.5 | Image of setup 2 used to record anodic CPP curves. . . . .   | 30 |
| Figure 4.6 | Schematic illustration of the setup used to record OCP, made by the author. . . . .  | 32 |
| Figure 4.7 | Image of the experimental setup used to record OCP. . . . .  | 33 |
| Figure 4.8 | Example on how to measure crevice depth (stated as delta z) in IFM. . . . .  | 34 |
| Figure 5.1 | Anodic CPP curves for 316L obtained in electrolytes with 600 ppm chloride and purged with CO <sub>2</sub> at different temperatures. . . . .   | 37 |
| Figure 5.2 | Anodic CPP curves for 316L obtained in electrolytes with 120 000 ppm chloride and purged with CO <sub>2</sub> at different temperatures. . . . .   | 37 |
| Figure 5.3 | Images of 316L samples after anodic CPP conducted at different temperatures in electrolytes with 120 000 ppm chloride and purged with CO <sub>2</sub> , obtained with IFM with 5X magnification. . . . . | 38 |
| Figure 5.4 | Anodic CPP curves for DSS obtained in electrolytes with 600 ppm chloride and purged with N <sub>2</sub> at different temperatures. . . . .   | 39 |
| Figure 5.5 | Anodic CPP curves for DSS obtained in electrolytes with 600 ppm chloride and purged with CO <sub>2</sub> at different temperatures. . . . .  | 39 |
| Figure 5.6 | Anodic CPP curves for DSS obtained in electrolytes with 120 000 ppm chloride and purged with N <sub>2</sub> at different temperatures. . . . .   | 40 |
| Figure 5.7 | Anodic CPP curves for DSS obtained in electrolytes with 120 000 ppm chloride and purged with CO <sub>2</sub> at different temperatures. . . . .  | 40 |

|   |    |
|---|----|
| Figure 5.8 Images of DSS samples after anodic CPP conducted at different temperatures in electrolytes with 120 000 ppm chloride and purged with N <sub>2</sub> , obtained with IFM with 5X magnification. . . . . | 42 |
| Figure 5.9 Anodic CPP curves for 316L obtained in electrolytes purged with CO <sub>2</sub> at 30 °C with different chloride concentrations. . . . .   | 44 |
| Figure 5.10 Anodic CPP curves for 316L obtained in electrolytes purged with CO <sub>2</sub> at 95 °C with different chloride concentrations. . . . .  | 44 |
| Figure 5.11 Images of 316L samples after anodic CPP conducted with different chloride concentrations in electrolytes purged with CO <sub>2</sub> at 95 °C, obtained with IFM with 5X magnification. . . . .       | 46 |
| Figure 5.12 Anodic CPP curves for DSS obtained in electrolytes purged with N <sub>2</sub> at 30 °C with different chloride concentrations. . . . .  | 47 |
| Figure 5.13 Anodic CPP curves for DSS obtained in electrolytes purged with CO <sub>2</sub> at 30 °C with different chloride concentrations. . . . .   | 47 |
| Figure 5.14 Anodic CPP curves for DSS obtained in electrolytes purged with N <sub>2</sub> at 95 °C with different chloride concentrations. . . . .  | 48 |
| Figure 5.15 Anodic CPP curves for DSS obtained in electrolytes purged with CO <sub>2</sub> at 95 °C with different chloride concentrations. . . . .   | 48 |
| Figure 5.16 Images of DSS samples after anodic CPP conducted with different chloride concentrations in electrolytes purged with CO <sub>2</sub> at 95 °C, obtained with IFM with 5X magnification. . . . .        | 50 |
| Figure 5.17 Anodic CPP curves for 316L obtained in electrolytes with 600 ppm chloride at 30 °C purged with N <sub>2</sub> and CO <sub>2</sub> . . . . .   | 51 |
| Figure 5.18 Anodic CPP curves for 316L obtained in electrolytes with 120 000 ppm chloride at 30 °C purged with N <sub>2</sub> and CO <sub>2</sub> . . . . .   | 52 |
| Figure 5.19 Anodic CPP curves for 316L obtained in solution at 95 °C with 600 ppm chloride purged with N <sub>2</sub> and CO <sub>2</sub> . . . . .   | 52 |
| Figure 5.20 Anodic CPP curves for 316L obtained in solution at 95 °C with 5000 ppm chloride purged with N <sub>2</sub> and CO <sub>2</sub> . . . . .  | 53 |
| Figure 5.21 Anodic CPP curves for 316L obtained in electrolytes with 120 000 ppm chloride at 95 °C purged with N <sub>2</sub> and CO <sub>2</sub> . . . . .   | 53 |
| Figure 5.22 Images of 316L samples after anodic CPP conducted in electrolytes with 600 ppm chloride at 30 °C and with different pH values, obtained with IFM with 5X magnification. . . . .                       | 55 |
| Figure 5.23 Anodic CPP curves for DSS obtained in electrolytes with 600 ppm chloride at 30 °C purged with N <sub>2</sub> and CO <sub>2</sub> . . . . .  | 56 |
| Figure 5.24 Anodic CPP curves for DSS obtained in electrolytes with 120 000 ppm chloride at 30 °C purged with N <sub>2</sub> and CO <sub>2</sub> . . . . .  | 56 |
| Figure 5.25 Anodic CPP curves for DSS obtained in electrolytes with 600 ppm chloride at 95 °C purged with N <sub>2</sub> and CO <sub>2</sub> . . . . .  | 57 |
| Figure 5.26 Anodic CPP curves for DSS obtained in electrolytes with 5000 ppm chloride at 95 °C with purged with N <sub>2</sub> and CO <sub>2</sub> . . . . .  | 57 |
| Figure 5.27 Anodic CPP curves for DSS obtained in electrolytes with 120 000 ppm chloride at 95 °C purged with N <sub>2</sub> and CO <sub>2</sub> . . . . .  | 58 |
| Figure 5.28 Images of DSS samples after anodic CPP conducted in electrolytes with 600 ppm chloride at 30 °C and with different pH values, obtained with IFM with 5X magnification. . . . .                        | 60 |

|  |    |
|--|----|
| Figure 5.29 Images of the surface of a 316L sample (both sides) tested in electrolyte with 600 ppm chloride and pH 4.2-5.0 at 30 °C, obtained with IFM and analyzed in ImageJ. . . . . | 61 |
| Figure 5.30 Crevice observed on a 316L sample after anodic CPP in 600 ppm chloride and pH 5.8-7.7 at 30 °C, imaged by IFM. . . . .   | 62 |
| Figure 5.31 Crevice observed on a 316L sample after anodic CPP in 600 ppm chloride and pH 4.2-5.0 at 30 °C, imaged by IFM. . . . .   | 62 |
| Figure 5.32 Crevice observed on a 316L sample after anodic CPP in 600 ppm chloride and pH 4.3-5.0 at 95 °C, imaged by IFM. . . . .   | 63 |
| Figure 5.33 Crevice observed on a 316L sample after anodic CPP in 5000 ppm chloride and pH 5.6 at 30 °C, imaged by IFM. . . . .  | 63 |
| Figure 5.34 Crevice observed on a 316L sample after anodic CPP in 120 000 ppm chloride and pH 5.3-5.9 at 30 °C, imaged by IFM. . . . .   | 64 |
| Figure 5.35 Images of the surface of a DSS sample (both sides) tested in electrolyte with 600 ppm chloride and pH 4.1-4.2 at 30 °C, obtained with IFM and analyzed in ImageJ. . . . .  | 65 |
| Figure 5.36 Crevice observed on a DSS sample after anodic CPP in 600 ppm chloride and pH 6.8-7.5 at 30 °C, imaged by IFM. . . . .  | 66 |
| Figure 5.37 Crevice observed on a DSS sample after anodic CPP in 600 ppm chloride and pH 4.1-4.2 at 30 °C, imaged by IFM. . . . .  | 66 |
| Figure 5.38 Crevice observed on a DSS sample after anodic CPP in 600 ppm chloride and pH 7.1-8.5 at 95 °C, imaged by IFM. . . . .  | 67 |
| Figure 5.39 Crevice observed on a DSS sample after anodic CPP in 120 000 ppm chloride and pH 7.2-8.5 at 30 °C, imaged by IFM. . . . .  | 67 |
| Figure 5.40 OCP development as a function of time for samples in an electrolyte without oxygen, with 600 ppm chloride and pH 7.0-7.4 at 30 °C. . . . .                                 | 69 |
| Figure 5.41 OCP development as a function of time for samples in an electrolyte without oxygen, with 600 ppm chloride and pH 7.2-8.0 at 95 °C. . . . .                                 | 69 |
| Figure 5.42 OCP development as a function of time for samples in an electrolyte without oxygen, with 19 000 ppm chloride and pH 7.1-7.8 at 45 °C. . . . .                              | 70 |
| Figure 5.43 OCP development as a function of time for samples in an electrolyte without oxygen, with 120 000 ppm chloride and pH 8.6-8.7 at 30 °C. . . . .                             | 70 |
| Figure 5.44 OCP development as a function of time for samples in an electrolyte without oxygen, with 120 000 ppm chloride and pH 6.5-7.0 at 95 °C. . . . .                             | 71 |
| Figure 5.45 OCP development as a function of time for samples in an electrolyte saturated with oxygen, with 120 000 ppm chloride and pH 7.3-8.1 at 30 °C, 60 °C and 95 °C. . . . .     | 71 |
| Figure 6.1 Change in $E_{crev}$ with chloride concentration and temperature for 316L at pH 6.05, created in Design-Expert. . . . .   | 76 |
| Figure 6.2 Change in $E_{rep}$ with chloride concentration and temperature for 316L at pH 6.05, created in Design-Expert. . . . .  | 77 |
| Figure 6.3 Change in $E_{crev}$ with chloride concentration and temperature for DSS at pH 6.0, created in Design-Expert. . . . .   | 78 |
| Figure 6.4 Change in $E_{rep}$ with chloride concentration and temperature for DSS at pH 6.0, created in Design-Expert. . . . .  | 79 |

|   |     |
|---|-----|
| Figure 6.5 Illustration of obtained $E_{crev}$ and $E_{rep}$ from anodic CPP measurements and OCP at different oxygen contents, created by the author. OCP at 100 ppb, 200 ppb and 500 ppb oxygen are obtained from measurements conducted by Equinor, presented in Figure 3.1. . . . . | 84  |
| Figure A.1 Images of the surface of a 316L sample (both sides) tested in electrolyte with 5000 ppm chloride and pH 5.7-7.0 at 95 °C, obtained with IFM and analyzed in ImageJ. . . . .  | 99  |
| Figure A.2 Images of the surface of a DSS sample (both sides) tested in electrolyte with 5000 ppm chloride and pH 7.2-8.2 at 95 °C, obtained with IFM and analyzed in ImageJ. . . . .   | 100 |
| Figure A.3 Images of the surface of a 316L sample (both sides) tested in electrolyte with 120 000 ppm chloride and pH 4.8-5.0 at 95 °C, obtained with IFM and analyzed in ImageJ. . . . .   | 100 |
| Figure A.4 Images of the surface of a DSS sample (both sides) tested in electrolyte with 120 000 ppm chloride and pH 4.9-5.0 at 95 °C, obtained with IFM and analyzed in ImageJ. . . . .  | 101 |

# Abbreviations

|         |   |  |
|---------|---|--|
| 2FI     | = | Two Factor Interaction                         |
| AES     | = | Auger electron spectroscopy                    |
| Ag/AgCl | = | Silver/Silver Chloride                         |
| AISI    | = | American Iron and Steel Institute              |
| ANOVA   | = | Analysis of variance                           |
| ASTM    | = | American Society for Testing and Materials     |
| C       | = | Carbon   |
| CCT     | = | Critical Crevice Temperature                   |
| CE      | = | Counter Electrode                              |
| Cr      | = | Chromium                                       |
| CRA     | = | Corrosion resistant alloy                      |
| CPP     | = | Cyclic Potentiodynamic Polarization            |
| CPT     | = | Critical Pitting Temperature                   |
| Cu      | = | Copper   |
| DSMC    | = | Disc Spring Multiple Crevice Assembly          |
| DSS     | = | Duplex Stainless Steel                         |
| Fe      | = | Iron   |
| IFM     | = | Infinite Focus Microscope                      |
| ISO     | = | International Organization for Standardization |
| MCA     | = | Multiple Crevice Assembly                      |
| Mn      | = | Manganese                                      |
| Mo      | = | Molybdenum                                     |
| N       | = | Nitrogen                                       |
| NaCl    | = | Sodium Chloride                                |
| Ni      | = | Nickel   |
| PEEK    | = | Polyether ether ketone                         |
| $PRE_N$ | = | Pitting Resistance Equivalent number           |
| ppb     | = | parts per billion                              |
| ppbw    | = | parts per billion by weight                    |
| ppm     | = | parts per million                              |
| ppmw    | = | parts per million by weight                    |
| PVC     | = | Polyvinyl chloride                             |
| RE      | = | Reference Electrode                            |
| SCC     | = | Stress Corrosion Cracking                      |
| SDSS    | = | Super Duplex Stainless Steel                   |
| SEM     | = | Scanning Electron Microscopy                   |
| SIMS    | = | Secondary ion mass spectrometry                |
| Ti      | = | Titanium                                       |
| WE      | = | Working Electrode                              |
| XPS     | = | X-ray photoelectron spectroscopy               |





## Symbol list

|            |   |   |
|------------|---|---|
| A          | = | Area [ $cm^2$ ]   |
| $E_{corr}$ | = | Corrosion potential [V vs. reference electrode]         |
| $E_{crev}$ | = | Crevice corrosion potential [V vs. reference electrode] |
| $E_{pit}$  | = | Pitting corrosion potential [V vs. reference electrode] |
| $E_{rep}$  | = | Repassivation potential [V vs. reference electrode]     |
| I          | = | Current [A]   |
| i          | = | Current density [ $A/cm^2$ ]                            |
| $i_{pass}$ | = | Passive current density [ $A/cm^2$ ]                    |
| OCP        | = | Open Circuit Potential [V vs. reference electrode]      |
| Q          | = | Charge [C]  |
| t          | = | Time [h]  |
| wt%        | = | Weight percentage                                       |



# 1 Introduction

The topic and objective of the specialization project preceding this thesis [1] has been maintained, and parts of this section have therefore been reused from the specialization project.

## 1.1 Background

Corrosion resistant alloys (CRAs) have a high resistance towards general corrosion and are therefore widely used in offshore installations. Stainless steels are often used in the process systems on oil and gas installations [2]. AISI 316L stainless steel (316L) is considered to be one of the most important stainless steels for marine atmosphere and is widely used. This is due to their good availability, low cost and acceptable corrosion resistance. 22% Cr duplex stainless steel (DSS) is the most used duplex stainless steel in the world. It offers high strength and good corrosion resistance. Compared to 316L the higher strength allow for weight savings and higher corrosion resistance can extend the lifetime, resulting in cost savings. By becoming more cost competitive, DSS has replaced 316L for many applications [3]. Although these stainless steels have good corrosion resistance, in a marine environment they will be exposed to humidity and chloride ions, which can lead to localized corrosion.

Localized corrosion, such as crevice corrosion, pitting corrosion and stress corrosion cracking (SCC) are the main corrosion challenges with using stainless steels in marine environment [4]. In worst case pitting and crevice corrosion can penetrate deep enough into the construction, resulting in leakage or fracture. 316L is a cheaper alternative than higher alloyed stainless steels, and therefore are the severity of the corrosion attacks and how it is affected by different environmental parameters of great interest. As DSS has become more cost competitive and has replaced 316L in different applications, their corrosion properties are of great interest as well [3].

Crevice corrosion can occur under specific conditions and crevice corrosion resistance is affected by various environmental parameters. Especially temperature, pH and chloride content play a key role, and several studies have been conducted to investigate the effect of these parameters [5][6]. Another parameter affecting the corrosion resistance is the dissolved oxygen content [7]. However, the role of the dissolved oxygen on localized corrosion has not been investigated to the same extent [6].

Today a limit of 10 ppbw oxygen in produced water during oil and gas production is used to avoid corrosion due to oxygen ingress, as a general practice among the oil and gas companies. Oxygen contamination can occur as a result of different industrial processes during operation, such as oxygen in production chemicals used, wash water used for desalting the oil, or oxygen in flare gas recovery. To avoid exceeding the maximum limit, the industry invests in oxygen removal technologies or choose to upgrade to higher corrosion resistant materials [2].

Recent tests have shown that the limit of oxygen may be higher than 10 ppbw. Increasing the oxygen application limit would be profitable in terms of material selection, operation and thereby be financially beneficial.

## 1.2 Objective

The main objective of this study is to investigate how different environmental parameters affect initiation of crevice corrosion on 316L and DSS in an environment with low oxygen content ( $< 10$  ppbw) through a literature survey and experimental work. In the experimental work the effect of chloride concentration, pH and temperature on the crevice corrosion properties of 316L and DSS are investigated. Through the experimental work, the crevice corrosion potential,  $E_{crev}$  and repassivation potential,  $E_{rep}$  shall be established. These results will then be used when conducting measurements of the open circuit potential (OCP) at different test conditions and oxygen contents, to establish a maximum acceptable oxygen content. Results obtained from these tests in addition to previous experimental results [1] will be used to discuss the oxygen application limit to avoid crevice corrosion of CRAs. In this study, Design of experiment (DOE) will be used as a method to evaluate the effect of the environmental parameters on crevice corrosion of the stainless steels, optimize number of tests and evaluate the experimental procedure.

## 2 Theoretical background

The theoretical background and relevant literature was reviewed and identified during the specialization project preceding this thesis [1]. No relevant new material was found during the work with this thesis, regarding Section 2.3, Section 2.5 and Section 2.6. The presentation of these sections from the project report is included below. In addition, parts of Section 2.1, Section 2.2, Section 2.4 and Section 2.7 are reused from the project report.

### 2.1 Austenitic and duplex stainless steels

Stainless steels can keep a "stainless" appearance unlike the rusty appearance common for carbon steels [8]. A rust layer will be formed on carbon or mild steels exposed to humidity. This layer is a complex hydroxide and is very porous, such that oxygen and humidity easily diffuses through the layer and create more rust [9].

Compared to carbon steels, stainless steels are more chemically complex due to their larger number of alloying elements, and belongs to the category of high alloy steels. They contain in general Fe and Cr, in addition to different alloying elements [9][10]. Stainless steels contain at least 12% Cr, which is the minimum amount to keep the stainless appearance. Cr will create a passive film on the metal surface in the presence of oxygen, and the Cr content in the alloy will therefore affect the alloys passivity a lot. This self-repairing, passive film will protect the metal from corrosion [8][9]. Compared to other alloys, stainless steels have a high corrosion resistance, as a result of the formation of the passive film. The composition and properties of the passive film are determined by the composition of the alloy. The corrosion resistance of stainless steels can therefore be enhanced by selecting a suitable alloy for the actual application conditions [11].

Stainless steels are divided into four main groups based on their microstructure; ferritic, austenitic, duplex and martensitic stainless steels [11]. DSSs consists of two phases; austenite and ferrite, in approximately equal amounts. Compared to their austenitic counterparts, DSSs have higher tensile and yield strength, and higher resistance towards stress corrosion cracking (SCC). The toughness of DSSs are between those of austenitic and ferritic stainless steels [12].

#### 2.1.1 Metallurgy

The composition of austenitic stainless steel is a balance between elements promoting ferrite formation, such as Cr and Mo and elements promoting austenite formation, such as Ni [12]. To remain austenitic in room temperature, iron alloys must contain about 17% Cr and 11% Ni (or its equivalence) [10]. In addition to Ni, C and N are also used to stabilize austenitic stainless steels, as they are easily soluble in the face-centered cubic (fcc) structure. By balancing the ferrite-promoting elements with the austenite-promoting elements, a great range of corrosion resistance can be obtained [12].

DSSs solidify mainly as ferrite. At high temperatures (1300 °C), austenite will first nucleate at ferrite grain boundaries and then grow. Diffusion of the alloying elements must take place during the transformation of ferrite to austenite. The austenite-stabilizing elements will concentrate in the austenite, while the ferrite-stabilizing elements will

concentrate in the ferrite. In DSSs, the ideal ferrite-austenite distribution is approximately 50/50, without other phases [10][12].

### 2.1.2 Microstructure

Austenitic stainless steels have a fcc atomic structure. The promoting of the fcc structure is done by adding elements such as Ni and Mn to the iron. Ferritic stainless steels on the other hand have a body-centered cubic (bcc) atomic structure, which is less dense than the fcc structure [10]. Since DSSs consists of both austenite and ferrite, it will have a mixed structure of fcc austenite and bcc ferrite. In DSSs, the matrix consists of ferrite with austenite islands, as illustrated in Figure 2.1 [12].

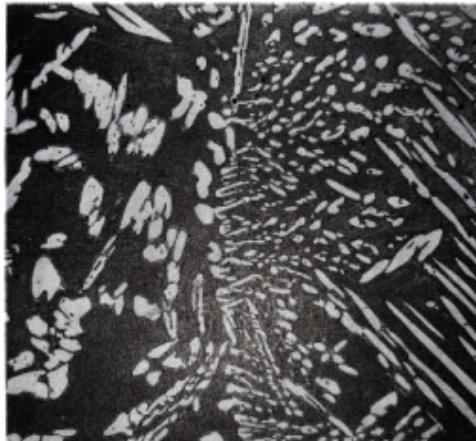


**Figure 2.1:** Microstructure of Cast Fe-22Cr-5.5Ni-3Mo-0.15N DSS etched in 40% NaOH, made of a ferrite matrix (dark phase) with austenite islands (light phase) [12].

### 2.1.3 Composition and alloying elements

Composition plays an important role in the corrosion resistance of stainless steels, and corrosion resistance can be altered by changing the alloy composition [12] [11]. The large number of alloying elements in stainless steels makes a large range of phases or crystal structures possible [10].

Cr is the only element that can by itself, create the passive film on stainless steels, and is therefor essential. Other elements can however contribute to maintenance of the film, or influence how effective it is formed. Increased Cr content increases the stability of the film. At the same time will higher Cr content also affect mechanical properties, weldability or how suitable the material is for certain thermal exposure. For that reason, it can be more beneficial to improve corrosion resistance by adjusting the content of other alloying elements in addition to the chromium content [12].

Ni as an alloying element gives an increased corrosion resistance, as it is a more noble element than iron. Especially in quantities above 8%, as it is in austenitic steels. In addition, Ni makes it easier to form the protective passive film, which gives faster repassivation in the event of damage [9]. Ferrite can not hold Ni in the solution, and can therefore not benefit from this element [10]. In austenitic stainless steels, Ni is one of the main stabilizing element [12].

Another important alloying element is Mo, which also improves the corrosion resistance especially in chloride environments. Together with Cr, Mo is very effective in terms of stabilizing the film in presence of chloride ions [12]. Mo added to stainless steels can increase the resistance towards localized corrosion, such as crevice and pitting corrosion. It can be added to both ferritic and austenitic stainless steels to improve the stability of the passive film [13]. Mo makes it easier to form the passive film and by stabilizing it, it will make the film break down more slowly [9].

Austenitic stainless steels seem to have a greater potential for aqueous corrosion resistance than their ferritic counterparts. The reason for this is that the most common used stabilizers in austenitic stainless steels; Ni, Mn, and N, all contribute to passivity [13]. Table 2.1 shows the alloying elements in the austenitic stainless steel, 316L.

**Table 2.1:** Alloy composition in wt% for AISI 316L stainless steel (UNS S31603) [14].

| <b>C</b> | <b>Mn</b> | <b>P</b> | <b>S</b> | <b>Si</b> | <b>Cr</b>   | <b>Ni</b>   | <b>Mo</b> |
|----------|-----------|----------|----------|-----------|-------------|-------------|-----------|
| 0.035    | 2.00      | 0.045    | 0.030    | 1.00      | 16.00-18.00 | 10.00-14.00 | 2.00-3.00 |

Cr and Ni are the main additives in DSSs. In addition to these elements, N, Mo, Cu, Si and W can be added to improve certain properties, such as corrosion resistance [12]. DSSs usually have high Cr and Mo contents, 22-27% and 2-4%, respectively [12][7]. Both the austenite and ferrite phase should have equal corrosion resistance, even though their composition is different. This is accomplished by utilizing the properties of different alloying elements. By balancing the amount of Cr and Mo with Ni, an approximately equal pitting corrosion resistance of the two phases is obtained and the austenite and ferrite ratio is kept nearly constant with temperature [10]. Table 2.2 shows the alloying elements in DSS.

**Table 2.2:** Alloy composition in wt% for 22% Cr duplex stainless steel (UNS S32205) [15].

| <b>C</b> | <b>Mn</b> | <b>P</b> | <b>S</b> | <b>Si</b> | <b>Cr</b>   | <b>Ni</b> | <b>Mo</b> | <b>N</b>  |
|----------|-----------|----------|----------|-----------|-------------|-----------|-----------|-----------|
| 0.030    | 2.00      | 0.030    | 0.020    | 1.00      | 22.00-23.00 | 4.50-6.50 | 3.00-3.50 | 0.14-0.20 |

The corrosion resistance of DSSs and austenitic stainless steels with similar alloying contents are almost equal [12]. Nevertheless, the least corrosion resistant DSS possess a greater corrosion resistance than one of the most common used austenitic stainless steels, 316L [16].

The pitting resistance equivalent ( $PRE_N$ ) is often used to determine the pitting corrosion resistance of a material in chloride solutions.  $PRE_N$  predicts the pitting corrosion resistance based on the alloy composition, and the calculation is based on percent mass fraction of the alloying elements Cr, Mo and N. The most commonly used formula to calculate  $PRE_N$ , according to [12], is presented in Equation 2.1:

$$PRE_N = \%Cr + 3.3(\%Mo) + 16(\%N) \quad (2.1)$$

## 2.2 Passive film

The key to the high corrosion resistance of stainless steels is the passivating and self-renewable protective film on the surface, referred to as the passive film [17]. Passive films are formed when the bare metal surface is exposed to an oxidizing environment [11]. When the surface comes in contact with the environment, it needs a period of time to form the passive film. The film will continue to grow until it has reached a steady state [18], and is typically only a few nanometers thick [13]. After the film is formed, the reaction rate between the metal and the environment will decrease significantly [11]. The passive film will contain the main metallic elements in the alloy, since its composition depends on the composition of the alloy. The fraction of the elements that is easy to oxidize will be higher than the elements that does not oxidize easily [18].

The corrosion resistance of stainless steel is determined by the stability of the passive film. The stability of the film is affected by the composition, structure and thickness, which is affected by the alloy composition. Figure 2.2 shows the relationship between the passive film, corrosion resistance and composition of the alloy [8].

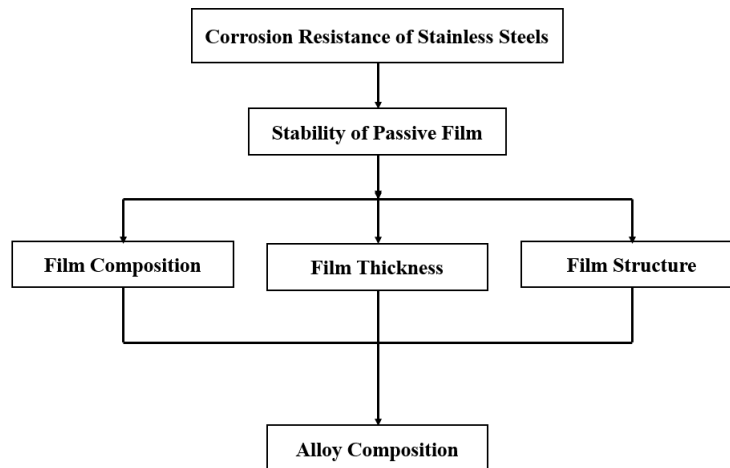


**Figure 2.2:** Illustration of the relationship between the passive film, corrosion resistance and composition of the alloy [8].

In general, it is believed that passivation takes place due to the following stages; first a rapid formation of hydrated complexes of metals, these are adsorbed on the surface. The complexes have to be stable enough on the alloy surface to enable the formation of a hydroxide phase when they react with water. Further on, this hydroxide phase will rapidly deprotonate to create an insoluble surface oxide film, referred to as the passive film. If the processes in any of these stages should fail, the active dissolution of the alloy will continue [18].

The passive film created on stainless steels is often duplex and is enriched in chromium. It consists of an inner chromium oxide/hydroxide layer and an outer iron oxide-enriched layer [17][19]. The outer layer composition depends on the film formation potential. At lower potentials it consists of  $\text{Fe}_3\text{O}_4$  and  $\text{Fe}(\text{OH})_2$ , while at higher it may consist of  $\text{Fe}_2\text{O}_3$  and  $\text{FeOOH}$  [17]. The passive film is formed on top of a nickel enriched layer, at the interface between the oxide layer and the bulk metal. Its origin is the selective oxidation of iron and chromium during anodic polarization. The passive film itself will however



contain almost no nickel [11], as shown in Figure 2.3.

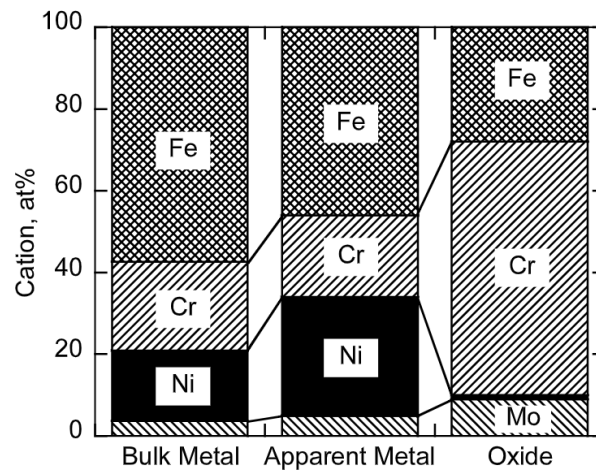


**Figure 2.3:** Composition of the passive film often created on austenitic stainless steel [11].

As illustrated in Figure 2.3, Mo is unlike Ni, enriched in the passive film. This is especially in the inner chromium oxide layer. The protective character of the passive film is mainly associate with the inner layer [19].

On DSS, a heterogeneous passive film is formed on both the austenite and ferrite phase, due to the different composition of the phases. Different alloying elements are partitioned to the two phases. In general, Cr and Mo to the passive film in the ferrite, and Ni and N to the passive film in the austenite [20].

To study the chemical composition of the passive films created on stainless steels, different surface analysis methods can be applied, such as auger electron spectroscopy (AES), X-ray photoelectron spectroscopy (XPS) and secondary ion mass spectrometry (SIMS) [21][22]. XPS can be used to study the composition and depth profiles of the passive film [19], and is widely used [17][19][21].

A breakdown of the passive film is either a result of mechanical damage or due to a chemical attack. This local breakdown often results in localized corrosion, such as pitting corrosion, crevice corrosion or SCC. Local breakdown of the passive film is therefore a very important reason for failure of stainless steels [8]. The passive film is not impenetrable to chlorine ions, and chloride ions may attack the passive film [9]. In the presence of chloride ions the passive film can therefore be broken, and the stainless steel is then susceptible to localized corrosion [23][24]. In addition to environmental parameters, such as chloride content and temperature, resistance to pitting and crevice corrosion of stainless steels are also dependent on alloying elements. As mentioned before, alloying elements such as Mo, Cr and Ni will improve the corrosion resistance. The synergistic effects of these alloying elements can both help stabilizing the passive film, and heal the passive film in case of damage through rapid repassivation [8].

## 2.3 Crevice corrosion

Localized corrosion is a very damaging type of corrosion since the corrosion current is limited to a small area and has a large penetration depth. The corrosion current density at the anode is often large, due to a large cathode area (the outside of the attacked area) and a small anode area (inside of the attacked area) [10].

The corrosion attack is called pitting corrosion if it is initiated at an open surface, and crevice corrosion if it is initiated at an occluded site [7]. Pitting and crevice corrosion are very similar. Some authors suggest that pitting corrosion is a special case of crevice corrosion, while others that crevices simply are large pits [25]. Metals and alloys that develop a passive film will be more prone to these localized attacks. The reason for this is that metals and alloys that does not develop a passive surface film usually corrode uniformly due to the high access of the oxidizing species that support the cathodic reaction [26].

Crevice corrosion is defined as the localized corrosion of a metal or alloy surface at, or right next to, an area that is not fully exposed to the environment because it is close to another metal or alloy surface, or next to another surface of the same material, according to [27]. Crevice corrosion develops in narrow openings or spaces between metal-metal or metal-non-metal intersections, such as joints, flanges, and welds [26].

Inside the crevice, mass diffusion is restricted and an environment with dissolved oxygen, decreased pH and chloride ions is established. This change in the chemical environment makes repassivation of the surface inside the crevice difficult. Since the rate of the anodic reaction inside the crevice is balanced with the rate of the cathodic reaction outside, the corrosion rate inside the crevice will be high [28]. The chemistry that develops inside an active crevice is illustrated in Figure 2.4 [29].

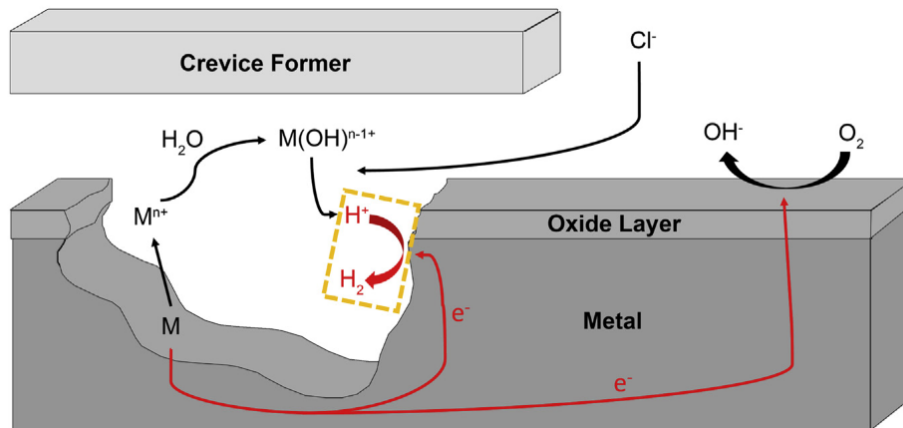


**Figure 2.4:** The chemistry that develops inside the crevice during crevice corrosion [29].

### 2.3.1 Crevice corrosion mechanism

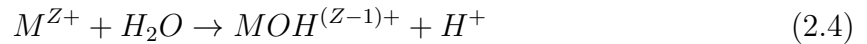
A well-established model for the crevice corrosion mechanism of stainless steels is the passive dissolution model [26]. When a passive metal or alloy is partially covered by a non-metallic surface and exposed to seawater the following reactions will take place:



and



Equation 2.2 and Equation 2.3 are the dissolution of the metal and the reduction of oxygen, respectively. The reactions occur both inside and outside the crevice initially, but after a while oxygen is depleted inside the cavity. The oxidation reaction continues inside the crevice, and results in an excess of metal cations,  $M^{Z+}$ . Further on, as this corrosion process continues, the metal cations in the crevice hydrolyze according to Equation 2.4. The reaction results in the formation of protons ( $H^+$ ) [26].



To balance the excess metal cations, anions such as chloride ions, moves from the bulk into the cavity of the crevice. This equalizes the charge difference and increases the concentration of metal chlorides inside the crevice. The acidic environment created by Equation 2.4 increases the dissolution rate of the metal in the crevice. This results in the production of more protons and further increase of the chloride content [26].

Even though the occurrence of localized corrosion depends on various factors, can how prone one specific type of stainless steel is to localized corrosion mainly be determined by the environmental conditions, such as temperature, chloride content, pH and oxygen content [4].

## 2.4 Parameters affecting crevice corrosion

Crevice corrosion of stainless steels is affected by several environmental parameters. Among these plays temperature, pH and chloride content an important role. As illustrated in Figure 2.5, corrosion resistance of stainless steels will in general decrease when temperature, chloride content and acidity of the electrolyte increase [5]. The curves show that the crevice corrosion potential decrease when the temperature and chloride concentration are high and pH is low. The location of the crevice corrosion potential,  $E_{crev}$  on the curves is illustrated in Figure 2.5c.

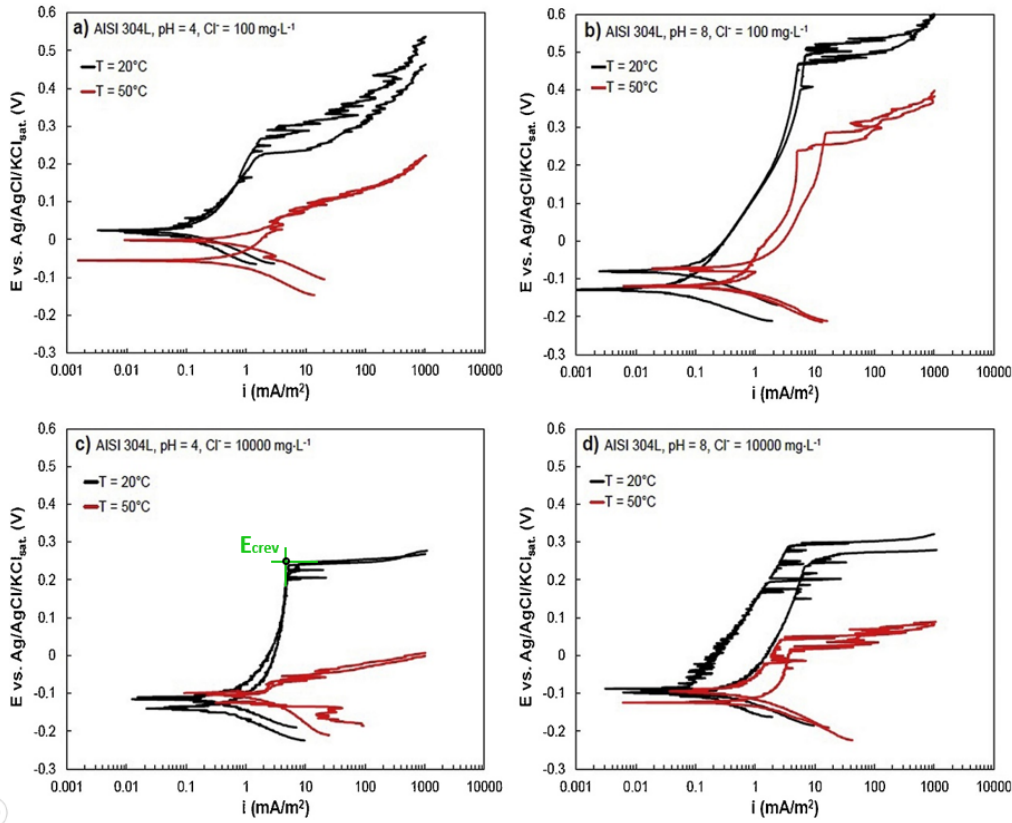


**Figure 2.5:** Example of how the potentiodynamic polarization curves to stainless steels are influenced by different environmental parameters [5].

### 2.4.1 Temperature

An increase in temperature, increases the rate of most chemical reactions [30]. In general, increased temperature will result in an increased tendency of local corrosion of metal and alloys, and faster pitting and crevice propagation. More positive pitting and crevice corrosion potentials are observed at lower temperatures, while more negative potentials are observed at higher temperatures [31]. In addition, increased temperature will result in faster diffusion and increased porosity of the passive film [32]. Increased porosity can lead to decreased resistance towards breakdown of the passive film and make the passive film less protective [33].

Temperature has a significant effect on corrosion of stainless steel in chloride solutions. It will affect the frequency distribution of the momentary variation in current, towards higher current. This indicates that a change in temperature can primarily increase the metastable pit growth, rather than activating new sites [31]. An increase in temperature will promote the corrosion tendency, because the corrosion process for the transition from metastable to stable corrosion is accelerated [31] or due to reduction in charge transfer resistance [33]. This also suggests that the transition from metastable to stable pit growth is easier accomplished at higher temperatures [31].

Most materials experience pitting and crevice corrosion above a certain threshold value, critical pitting temperature (CPT) and critical crevice temperature (CCT), respectively

[31]. In the same environment crevice corrosion will occur at a lower temperature than pitting corrosion. Consequently, CCT will in general be lower than CPT [10].

### 2.4.2 Chloride content

When chloride ions are present, stainless steels can be exposed to local attacks in the form of pitting or crevice corrosion. This is due to the breakdown of the protective passive film at random sites caused by the chloride ions [34]. The chloride ions have high diffusivity, a small size and a strong acidic anionic nature. Their small size allows the ions to penetrate through the passive film. Experiments have shown that an increase in the chloride concentration decreases the corrosion resistance of stainless steels [30].

The presence of chloride can be destructive to the stability of the passive film. Three models are frequently used to describe the effect of chloride ions presence; adsorption causing local dissolution of the film, anions penetrating the film causing weakening of the oxide bonds, and breakdown of the film at defects [11].

Higher chloride concentration increases the probability of chloride ions to be adsorbed or to penetrate through the passive film. In addition, a greater availability of chloride ions will make it easier for the ions to replace water molecules or hydroxide ions at undeveloped or damaged parts of the passive film [35]. If chloride ions are adsorbed at sufficient high chloride concentrations, further film formation will be prevented and anion vacancies can be created in the film and cause it to collapse [36].

### 2.4.3 pH

Change in pH would change the chemistry of a solution, and thereby affect the corrosion characteristics of stainless steels [37]. Increasing the pH leads to a lower dissolution rate, resulting in a thicker passive film with higher iron content, as iron oxides are more stable in an alkaline solution [11]. In an acidic solution, the passive film will be weakened and the passive film will become thermodynamic unstable if the solution is severely acidic, according to the Pourbaix diagram [5].

There are different explanations on why the passive film becomes unstable when the pH is low enough. While some authors believe that an acidic solution decreases the localized corrosion resistance due to the decreasing thickness and more defects in the passive film [38]. Other authors think it is due to the competition between chloride ions and hydroxide ion for the opportunity to be adsorbed on the metal surface. When the pH decreases, the chloride ions will become more predominant, and the passive film will become thinner. After local depassivation occurs, the chloride ions will continue to compete with the hydroxide ions. If chloride ions are adsorbed to the surface, it will prevent repassivation of the surface [39].

Dastgerdi et al. [4] observed that the breakdown potential increased with increasing pH. Higher pH values moved the potential in a more noble direction. In severe acidic solutions, with pH 2.7, the metal had an active behavior and the passive part of the polarization curves disappeared. The report states pH had a significant effect when the chloride concentration in the solution was low (100 ppmw chloride). At higher chloride concentrations (10 000 ppmw chloride), pH had a less significant effect. Additionally, in

the pH range 4-7, the breakdown potential showed little change with increasing pH. This was especially prominent when the chloride concentration was high [4]. Similar results was also observed by Tzaneva [40], which stated that the pH of the solution did not significantly influence the protective properties of the passive film on austenitic stainless steels at pH 2-10. The experiments included testing in 3.5% NaCl solutions with pH 1-12 [40].

#### 2.4.4 Fluid flow

Crevice corrosion tests are normally conducted in static solutions. For stainless steels, fluid velocity is an important parameter to include when determining the materials suitability in a specific environment [41]. Fluid velocity can alter the local composition inside pits and thereby affect pit growth rate or repassivation [42]. In addition, increased velocity can increase the cathodic reaction rate outside the pit or crevice. Less pitting has been observed on austenitic stainless steels, such as AISI 304 and 316 with increased fluid velocities. Velocities above 1.5 m/s is recommended to avoid pitting [41][43].

When studying the effect of different parameters on pitting corrosion of AISI 316L stainless steel in aqueous solution, Malik et al. [34] observed that static conditions were more suitable for pit initiation and propagation, compared to dynamic. Fewer pits were observed on the specimen surface under dynamic conditions [34]. Danek [44] also observed that dynamic flow increased the localized corrosion resistance of stainless steel in sea water [44].

Wharton and Wood [41] investigated how flow conditions influenced corrosion of AISI 304L stainless steel. The results showed that metastable pitting occurred at static, laminar and turbulent conditions. Laminar and turbulent flow showed little overall effect on the nucleation rate of metastable pits. By comparing laminar and turbulent flow the results showed that stable pits were more prominent at laminar flow, right before the transition to turbulent flow [41]. Brown et al. [45] observed that under laminar flow conditions, increased flow velocity stabilized the passive film on stainless steel and made it more resistant towards pit initiation [45].

Fabbricino and Korshin [46] studied the behavior of corrosion potential (otherwise referred to as open circuit potential (OCP)),  $E_{corr}$  of iron exposed to drinking water, sulfate solution and chloride solution in stagnation and flow conditions. The results showed that  $E_{corr}$  decreased during stagnation condition, and increased during flow conditions. This was the case for all the solutions tested. Presence of sulfate or chloride ions resulted in decreased  $E_{corr}$ , and  $E_{corr}$  decreased with increasing chloride concentration [46].

The effect of fluid flow on localized corrosion of stainless steel will not be a part of the experimental work in this thesis. A review of literature was performed to investigate the effect of different flow conditions. It was included as a part of the theoretical background as it proved to be an important parameter to consider when evaluating the suitability of a material in a corrosive environment.

## 2.5 Produced water systems

The term produced water is used for water that is trapped in underground formations and is brought up together with oil or gas. This by-product can consist of formation or condensate water. The physical and chemical properties vary, but produced water contains in general salts, organic acids, carbon dioxide and other organic compounds. Both produced water in oil wells and the condensate in some gas wells can contain a lot of salt and are usually more saline than seawater [47].

The sea water in the North Sea has an ambient pH of 8.1 and chloride concentration of about 19 000 ppmw. Conditions reported for produced water emissions from oil and gas platforms located in the North Sea are presented in Table 2.3.

**Table 2.3:** Water conditions for produced water from oil and gas platforms in the North Sea [48].

| Water type      | Chloride concentration [ppmw] | pH        |
|-----------------|-------------------------------|-----------|
| Sea water       | 19 000                        | 8.1       |
| Formation water | 12 000 - 100 000              | 6.0 - 7.7 |
| Condense water  | <1000 - 189 000               | 3.5 - 5.5 |

Formation water is produced water from crude oil production and condense water is produced water from natural gas production [48]. The material used for produced water, such as carbon or stainless steels can be prone to corrosion due to the high chloride content and low pH and the dissolved gases ( $\text{CO}_2$  and  $\text{H}_2\text{S}$ ) in gas wells [47].

## 2.6 Test methods for crevice corrosion

Different test methods can be used to characterize the localized corrosion resistance of stainless steels [49]. ASTM G48 is a commonly used standard to evaluate the corrosion resistance of stainless steels, and ASTM G48 method D and F can be used to determine the CCT of a material [50]. The standard is a non-electrochemical test method and determines corrosion resistance based on weight loss and visual observations for a sample exposed in a specific electrolyte at a fixed temperature. It can be used to qualitative rank crevice corrosion resistance [49].

Electrochemical methods can be used to obtain quantitative information about pitting and crevice mechanisms, in addition to rank localized corrosion resistance of different materials. Tests conducted with these methods can be used to quantify critical potentials, such as the crevice corrosion potential,  $E_{crev}$  and repassivation potential,  $E_{rep}$ . Several test methods can be used, but ASTM G61 standard is definitely the most common electrochemical method used to determine the susceptibility to localized corrosion of stainless steels [49].

Another electrochemical method is the ASTM G150 standard. ASTM G150 can be used to determine the CPT, and be modified to determine the CCT. The method can also be used to predict the condition resulting in stable crevices. This involves applying a fixed potential followed by measuring of the current response as a function of time when

increasing the temperature [51]. As the objective of this thesis is to establish  $E_{crev}$  and  $E_{rep}$ , ASTM G61 will be used as experimental method.

### 2.6.1 Cyclic potentiodynamic polarization curves

Recording anodic polarization curves is common practice to investigate the active-passive behavior of different alloys, and can be used to study the corrosion behavior of stainless steels. A common approach to record these curves is based on the potentiodynamic method. How to carry out this method is described in ASTM G61 [52] and will be presented in Section 4.2. Since the materials investigated in this thesis are expected to exhibit crevice corrosion at the chosen test conditions, an introduction to these curves is presented in this section.

The cyclic potentiodynamic polarization (CPP) technique uses a three electrode configuration cell [53]. The applied potential between the working and the reference electrodes are increased from a low value to a high value, until a predefined current density or potential is reached. Then the applied potential scan is reversed. The reversed scan is continued until the hysteresis loop is closed or the corrosion potential is reached [49]. The current through the working and counter electrode is measured, and after taking the working electrode area into account the current density is calculated. As a result of this test, the potential is plotted against the logarithm of the current density [53]. This technique can be used alone or combined with changing environmental parameters, such as chloride content, pH or temperature [49]. An example of a cyclic potentiodynamic polarization curve for pitting corrosion is presented in Figure 2.6.

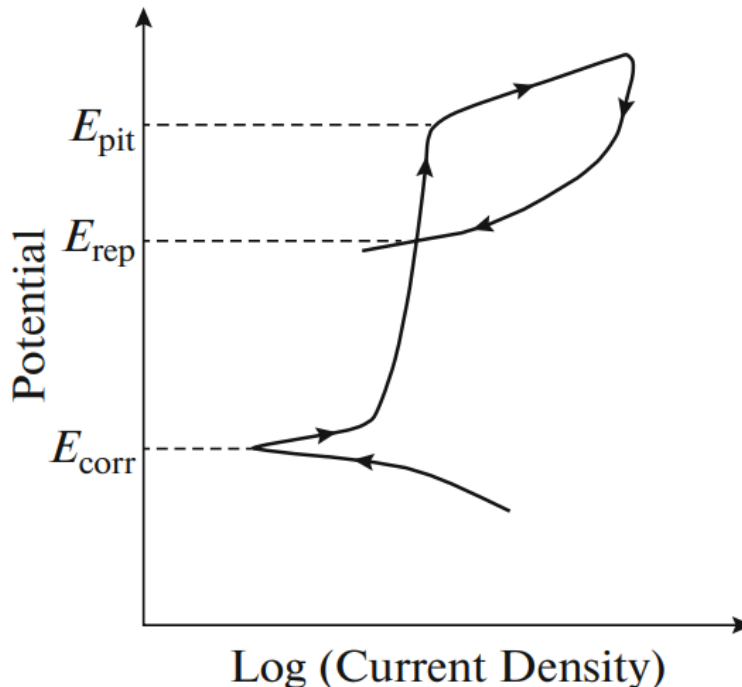


**Figure 2.6:** An example of a typical cyclic potentiodynamic polarization curve for pitting corrosion for a sample exhibiting protection potential [54].

Prior to the anodic polarization scan, the sample is immersed in the electrolyte until



the OCP is stable. After reaching the steady state, the potential scan is started at the measured OCP or 100 mV below, depending on the test method [54].

When the tested sample undergoes localized corrosion, the passive film will be damaged. This corresponds to the breakdown potential, which in the case of pitting corrosion becomes pitting corrosion potential,  $E_{pit}$  or crevice corrosion potential,  $E_{crev}$  in the event of crevice corrosion [53]. This is the potential where the current density increases rapidly. Crevice corrosion can only be initiated when the potential exceeds the crevice corrosion potential [54].

After the scanning direction is reversed, the scan will continue until it crosses the forward scanning polarization curve or until the corrosion potential,  $E_{corr}$  is reached. The intersection between the forward and reversed scanned curve is called the repassivation potential,  $E_{rep}$  [54]. Propagation of crevices can only continue above  $E_{rep}$  [55]. When the potential is between  $E_{crev}$  and  $E_{rep}$ , only the propagation of already initiated crevices can continue. The difference between these two potentials indicates the probability of localized corrosion. Greater difference between  $E_{crev}$  and  $E_{rep}$  indicates lower crevice corrosion resistance [54].

The size of the hysteresis loop is determined by the difference between the current density for the forward and reversed scan at the same potential. A larger loop indicates more passive film disruption and more difficulties restoring the damaged film, resulting in decreased corrosion resistance [54].

To protect the material from crevice corrosion, the potential should be kept under  $E_{rep}$ . The repassivation potential,  $E_{rep}$  can be affected by different environmental parameters, such as chloride content. Accumulation of chloride ions inside the crevice can prevent repassivation of the crevice wall. Deeper crevices will hinder repassivation as well, due to slower transport kinetics between the crevice tip and the bulk solution [55].

Several methods can be used to determine  $E_{crev}$  and  $E_{rep}$  from the anodic cyclic potentiodynamic polarization curves. In this thesis  $E_{crev}$  is determined at the intersection point illustrated in Figure 2.7.  $E_{rep}$  is determined at the point where the hysteresis loop closes, this intersection point is illustrated in Figure 2.8 [56][57].

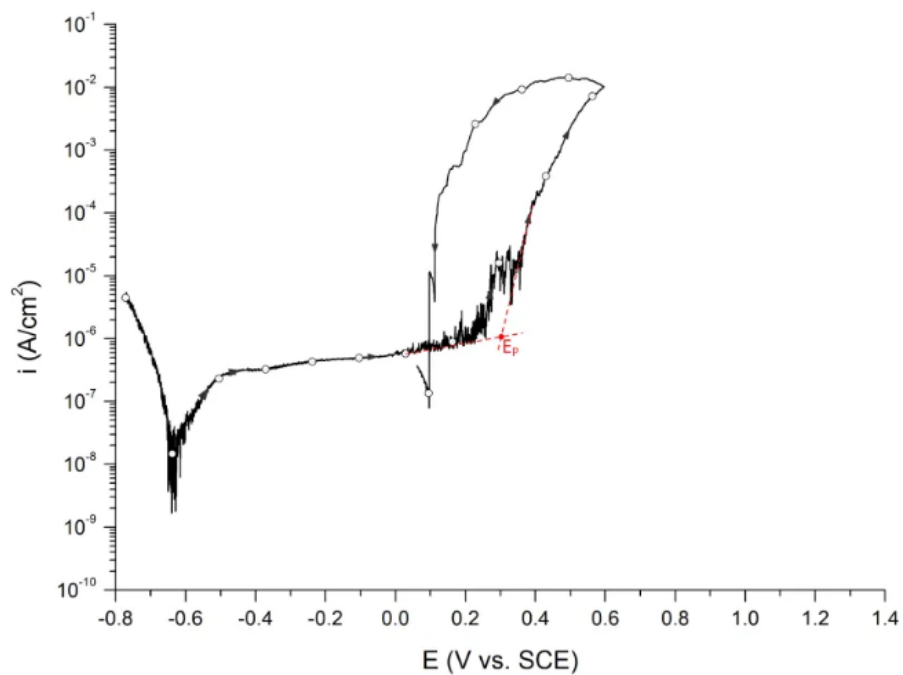


**Figure 2.7:**  $E_{crev}$  is determined as the potential at the inflection point, illustrated as  $E_P$  [56].

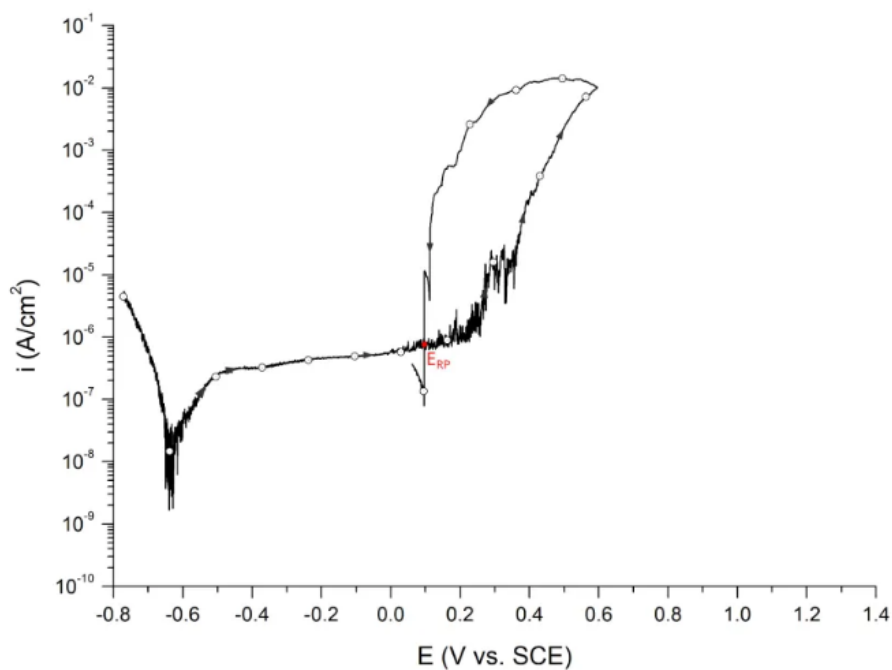


**Figure 2.8:**  $E_{rep}$  is determined as the potential where hysteresis loop closes, illustrated as  $E_{RP}$  [56].

The passive current density curve usually has a steep slope and the current density,  $i_{pass}$  can be determined at the midpoint of this part of the curve. If the slope is not steep, a middle value will be extrapolated in this thesis.

## 2.7 Design of experiments

In a traditional approach to experimental procedure, where all test parameters are included in the test program, a high number of tests must be conducted. The effect of one parameter is studied at a time by keeping the others constant. By using factorial design, multiple factors can be changed at once, and interactions between variables are taken into account. In contrast to the traditional approach, parameters will be varied together instead of one at a time [58]. The factorial design planning process, or Design of experiments (DOE) is defined as "A systematic series of tests, in which purposeful changes are made to input factors, so that you may identify causes for significant changes in the output responses." [58].

For instance, if the effect of three different parameters are investigated and four values for each of the parameters are tested, total number of tests will be:  $4^3 = 64$ . If all the tests are repeated, this will result in 128 tests. DOE can reduce the number of tests by maximizing information with a minimum number of tests [58]. This is done by identifying the best experimental combinations. DOE uses a collection of mathematical and statistical techniques, and can obtain a correlation between the different parameters by creating a regression equation [5].

DOE is in general divided into two main categories; screening and optimization methods. Screening techniques are applied to determine which parameters that have an effect and to what extent [59]. This is done by conducting experiments at two levels for each parameter; a maximum and a minimum. This is maximum and minimum values for the chosen parameter, relevant for the experiment. The method uses a first-order regression model to determine the relationship between the parameters. Optimization methods are more extensive as they in addition to determine the significant parameters, also find the best model. This method is also based on conducting experiments at different levels for each parameter. In addition to the maximum and minimum levels included in screening methods, the average between maximum and minimum is also included. When using these methods, maximum and minimum are referred to as a factorial point. The average between maximum and minimum is referred to as center points. Center points reduces the amount of error in the model. Response Surface Methodology (RSM) is a very important optimization method, and can develop both first- and second-order regression models [60].

Dastgerdi et al.[5] used DOE to study the influence of temperature, pH, and chloride concentration on localized corrosion of stainless steel. By using a RSM method called Central composite design (CCD), number of tests necessary to investigate the effect of different parameters on the passivity breakdown potential were reduced [5]. In addition to factorial and center points, this method consider star points too. Star points were decided by the software used in the study and were extrapolated from the maximum and minimum levels [59]. This method is a five level design, which means that five points/levels are generated for each factor investigated; a minimum, a star point extrapolated from the minimum, a maximum, a star point extrapolated from the maximum and a center point, the average between the maximum and minimum. Figure 2.9 shows a schematic

illustration of the CCD design.

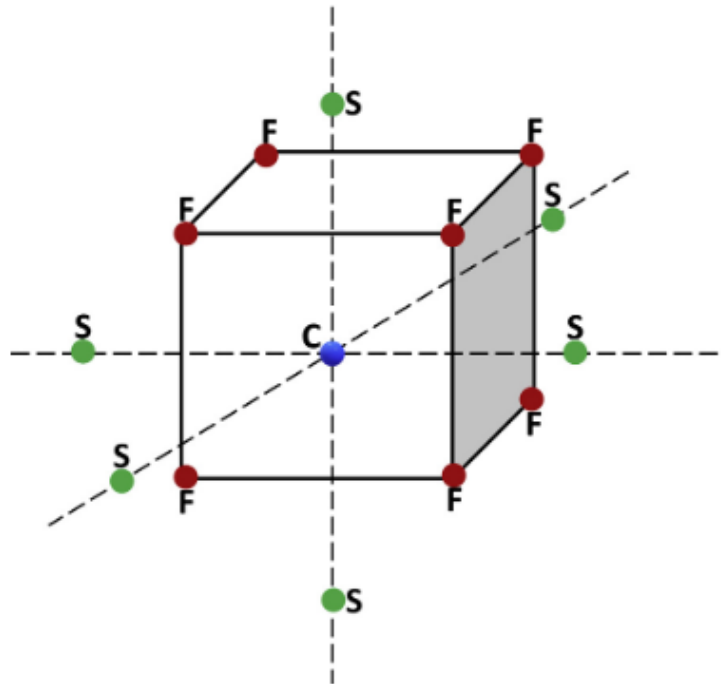


**Figure 2.9:** Schematic illustration of the CCD method, including the different points; factorial (F), center (C) and start (S) points [59].

By using the CCD method, Dastgerdi et al. [5] reduced number of tests from 250, as it would have been by the traditional approach according to the report, to 40 tests. The use of DOE provided a regression equation, which was used to evaluate the effect of different parameters on the pitting and crevice corrosion of UNS S30403 stainless steel. The regression equation was analyzed by comparison with laboratory results and literature. DOE agreed well with literature and experience regarding localized corrosion, in most conditions. However, the DOE result overestimated the pitting corrosion resistance in some conditions. In the report this is explained by the fact that the surface area and finishing may be different or the occurrence of more severe crevices in real application. The results showed that passivity breakdown potential was affected by temperature, chloride concentration and pH, and the temperature had the most severe effect [5].

Dastgerdi et al. [4] also compared screening and optimization methods, by comparing the CCD method to a full factorial design. Full factorial design is a type of screening method, and considers all possible maximum and minimum combinations of all the input parameters. The experiments were conducted at two levels; maximum and minimum level. The CCD method on the other hand, implements a higher number of levels by including center and star points as well. Number of tests conducted were 16 for the full factorial design and 40 for the CCD method and were based on number of levels included by the methods. Higher number of levels resulted in more tests. After conducting the experiments it was concluded that both DOE designs corresponded well with experimental results. Nonetheless, the optimization method, CCD was preferable, because it predicted the midpoints better [4].

DOE will be used in this master thesis to evaluate the effect of environmental parameters on the crevice corrosion of stainless steels, evaluate the experimental procedure and optimize number of tests. After performing the experiments, the crevice corrosion and repassivation potentials obtained from the polarization curves will be introduced to the software. The softwares used in this thesis is Unscrambler and Design-Expert, provided by Camo Analytics [58]. The softwares will be used to analyze the results and evaluate the significance of the different parameters.



### 3 State of the art

It is well known that crevice corrosion is affected by several environmental parameters, and several studies have been conducted to investigate the effect of different parameters. However, there are significantly fewer studies devoted to the effect of dissolved oxygen than effect of other parameters on corrosion of various materials [6]. CRAs are used in the water injection service to a large extent, for instant in process piping, pumps and valves. A current limit of 10 ppbw dissolved oxygen for these materials are used in the industry. During actual operation, this limit can be exceeded due to various unavoidable situations. In addition, sometimes it is difficult to control the dissolved oxygen content and keep it below 10 ppbw during operation [2]. Oxygen content will be stated as ppb instead of ppbw further on in this thesis.

In this section, previous research on the effect of oxygen on crevice corrosion and the maximum acceptable oxygen content to avoid pitting and crevice corrosion on 316L, DSS and similar stainless steels are presented. The state of the art and relevant literature were reviewed through a literature survey in the specialization project preceding this thesis [1]. Parts of this section are similar to the corresponding section in the project report, but has been amended with discussion of a few additional papers that have been studied after the specialization project.

#### 3.1 Effect of oxygen

Dissolved oxygen is one of the main reasons for corrosion, frequently pitting and crevice corrosion, in the oil and gas industry [61]. Corrosion types connected to the oil and gas industry, such as  $H_2S$  corrosion,  $CO_2$  corrosion and microbiologically induced corrosion have been considerably studied. Compared to these, oxygen corrosion can act as an equal or greater threat. An aqueous environment containing oxygen is aggressive towards stainless steels due to the strong oxidizing nature of the oxygen [62]. As a strong oxidizer, oxygen reacts quickly with metals, such as iron [61]. Not only can oxygen cause serious corrosion damage, but a lot of corrosion inhibitors does not work well in the presence of oxygen [62].

Generally, two main effects of dissolved oxygen on the corrosion rate exists. Dissolved oxygen in seawater is in general a very aggressive species towards corrosion of metals, and is dependent on type of metal or alloy. CRAs have negligible general corrosion in aerated water due to the protective passive film created on the surface. This film is formed immediately when exposed to oxygen. A high oxygen content will therefore be favorable for the formation of the passive film [63], which protects the material from corrosion. Nevertheless, CRAs can be susceptible to localized corrosion in aerated seawater. Surface deposits on these alloys can create oxygen concentration cells, which can cause pitting and/or crevice corrosion [64]. In an oxygen concentration cell, the passive film on the area with access to the dissolved oxygen will be in better condition than the area shielded from oxygen. As a result of this, the area with oxygen access will be cathodic to the shielded area [65]. Under cathodic control, the corrosion rate will be limited by the rate of the cathodic reaction, the reduction of dissolved oxygen, which is consumed as an depolarizing agent. In this case, increased oxygen concentration will raise the corrosion current and the corrosion rate [66][67].

Rybalka et al. [6] studied corrosion currents of 17-4 stainless steel in a NaCl solution with different dissolved oxygen concentrations. When the dissolved oxygen concentration in the solution was below 20%, the results showed that a small increase of the oxygen content resulted in a significant change of the corrosion potential, towards more positive values. On a cathodically activated surface, an increase in oxygen concentration resulted in a facilitation of the cathodic reaction and consequently increased the corrosion rate [6].

### 3.1.1 Alteration of the passive film

Dissolved oxygen will dominate the oxidation process when available and increase the potential of the metal. Increased potential might move the metal into the passive region and can affect the passive film and the composition of the film [22].

In sodium chloride solutions, the oxygen content has been found to alter the passive film on stainless steels. Even at concentrations of only 10 ppb, dissolved oxygen were found to alter the oxide film of stainless steels at high temperatures, resulting in increased corrosion potential (otherwise referred to as OCP) [68][69]. For oxygen concentrations within the passive region, presence of chloride ions can cause localized corrosion as a result of the local breakdown of the passive film, as mentioned earlier. The chloride ions will competitively displace the adsorbed oxygen at the local anodes formed in the restricted areas [67].

Feng et al. [70] studied how dissolved oxygen affected the electrochemical behavior of 316L in borat buffer solution. The report suggested that sufficient amount of oxygen bubbles in the solution can change the morphology, structure and growth of the passive film. This would have an effect on the anodic dissolution of the metal. Results showed that both the cathodic and the anodic process of 316L were accelerated when the dissolved oxygen content in the solution were increased [70].

Baek et al. [22] studied the effect of dissolved oxygen on the corrosion film on low carbon steel in a NaCl solution. The report stated that dissolved oxygen had a critical role regarding the formation and growth kinetics of the passive film on the steel. By changing the oxygen concentrations, the iron oxide products developed changed: at high concentrations with formation of  $\gamma - \text{Fe}_2\text{O}_3$  and  $\text{FeOOH}$ , and at low concentrations with formation of  $\alpha - \text{Fe}_2\text{O}_3$ .

### 3.1.2 Oxygen reduction reaction

The cathodic process related to corrosion of alloys in aerated chloride solutions, primarily the oxygen reduction, is an important factor to consider when determining the corrosion rates of CRAs [71]. By increasing the rate of the cathodic reaction, oxygen can increase the corrosion rate, both as uniform and local corrosion. [62].

Chen et al. [62] investigated the corrosion behavior of Q345R steel in 1 wt% NaCl solution, and the effect of oxygen concentration, temperature and pH. The report stated that the oxygen concentration affected the corrosion behaviour of the material. The experimental results showed that the corrosion potential increased with increasing oxygen concentration, indicating that the corrosion of Q345R steel is determined by the cathodic reaction. Increased oxygen concentration also increased the corrosion current density, which was interpreted as an accelerated cathodic reaction as a result of the increased



oxygen content [62].

Wang et al.[72] studied the effect of dissolved oxygen on the corrosion behavior of API-X80 pipe steel in a solution simulating soil medium. This was done in a weakly acidic aqueous solution, with small amounts of different salts, first of all 46.8 ppmw NaCl and pH 4.5. The results showed that the corrosion rate was controlled by the dissolved oxygen content. At a concentration of 0.85 ppmw in the solution, the presence of oxygen had an effect on the cathodic process. The corrosion rate decreased with decreasing oxygen concentration. However, when the oxygen concentration was above 1.90 ppmw, the corrosion rate was controlled by the anodic process. The results showed that the presence of dissolved oxygen also had an effect on the composition of the corrosion products [72].

### 3.2 Oxygen application limit

Due to the effect oxygen has on the corrosion resistance, stainless steels must be operated within a oxygen content limit. The application of the corrosion resistant alloys 316L, DSS and 25% Cr super duplex stainless steel (SDSS) are often limited to 10 ppb dissolved oxygen in well fluid conditions, according to Wahaibi et al. [2]. This is the general practice among the oil companies. The importance of evaluating the oxygen content during materials selection is stated in ISO 21457 [73], which is currently the only international standard covering all issues regarding materials selection, according to [74].

Wahaibi et al. [2] suggested that this application limit could be expanded. They conducted experiments with 316L, DSS and SDSS, to investigate pitting and crevice corrosion. NaCl concentrations used in the tests were 16, 100, 167 and 250 g/L NaCl, temperatures were 50 °C and 60 °C and dissolved oxygen concentrations were 20, 50 and 100 ppb. The results showed that 316L was less resistant towards pitting and crevice corrosion than DSS and SDSS. An increased oxygen concentration in combination with the presence of chloride ions resulted in increased localized corrosion. The results showed that an increased oxygen content resulted in more evident effect of the salt content and temperature as well. The conclusion from the study was that 316L was resistant to localized corrosion up to 20 ppb dissolved oxygen. DSS was resistant up to 20 ppb dissolved oxygen for all tested salt concentrations and temperatures and 50 ppb dissolved oxygen, except in solution with 250 g/L NaCl at 60 °C. SDSS was resistant to localized corrosion at all salt concentrations and temperatures tested. An increase from 20 ppb to 100 ppb dissolved oxygen showed no effect on the corrosion resistance of SDSS [2].

Larché et al. [75] investigated corrosion attacks on DSS (UNS S82551) in treated seawater at 30 °C with different dissolved oxygen concentrations. The results showed that the risk of crevice propagation increased with increasing dissolved oxygen content. In other words, higher oxygen content resulted in higher corrosion rates. No crevice corrosion occurred on UNS S82551 when the dissolved oxygen concentration was below 50 ppb. This fits well with the results obtained by Wahaibi et al. [2], where DSS was resistant to crevice corrosion when the dissolved oxygen content was 50 ppb at 50 °C.

### 3.3 OCP measurements at different oxygen contents

In this thesis, the crevice corrosion potential,  $E_{crev}$  and corresponding repassivation potential,  $E_{rep}$  for 316L and DSS at different environmental conditions will be established, by conducting tests with different chloride content, temperature and pH. By using the established  $E_{crev}$  and  $E_{rep}$ , the maximum acceptable oxygen content at the different conditions can be defined. This is done by measuring the OCP of the materials in solutions with different oxygen contents. The change in OCP with increased dissolved oxygen (DO) content of stainless steel with  $PRE_N$  in the range 23–38 is presented in Figure 3.1 [76]. This is unpublished data established by Equinor, that has been given permission to be used in this master thesis. The dissolved oxygen limit is defined when the OCP equals the established  $E_{crev}$  or  $E_{rep}$ .  $E_{rep}$  would be a more conservative application limit, as this potential normally is below  $E_{crev}$ .

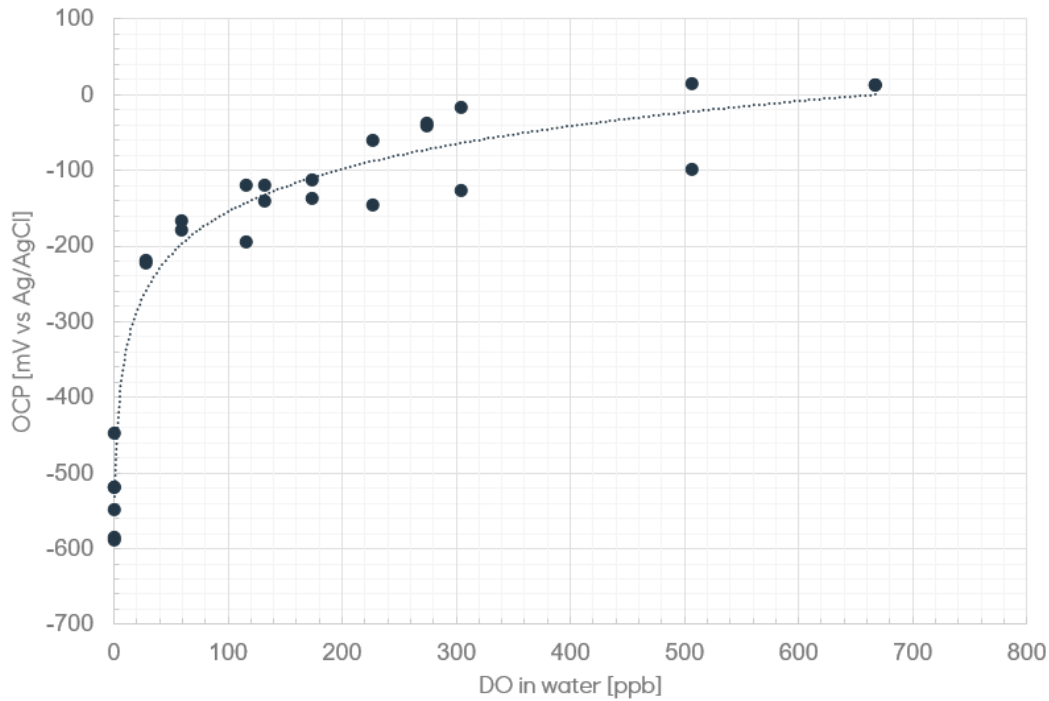


**Figure 3.1:** OCP development as a function of dissolved oxygen (DO) content, for stainless steel in solution with 19 000 ppm chloride and pH 7.5 at 45 °C [76].

## 4 Experimental

The objective during the experimental work in this thesis was to investigate the effect of chloride content, temperature, pH and oxygen content on the crevice corrosion potential and repassivation potential for 316L and DSS, as well as study the development of crevice corrosion. The experimental work included anodic CPP and OCP measurements.

The anodic CPP curves were established according to ASTM G61 [52] at selected test conditions. Test conditions that enabled tests in electrolytes with similar properties as produced water were chosen. The experiments were conducted in an environment without oxygen, as the oxygen in the electrolytes were removed prior to each test. Anodic CPP measurements were also conducted in the specialization project preceding this thesis [1]. Description of the material preparation and ASTM G61 are the same as in the project report and are included below. Two different setups were used to record the anodic CPP curves, as the setup was improved based on experiences from the specialization project. Setup 1 was used during the specialization project [1], while setup 2 was used in this thesis. Description of both setups and differences between the two are included below, as results from the specialization project are evaluated in this thesis as well.

Experiments where the samples were exposed at OCP for 48 hours at different test conditions were also conducted. These results were planned to be compared with the result from the tests according to ASTM G61 [52], to define critical dissolved oxygen content. Tests with different oxygen contents were therefor supposed to be conducted. Due to the COVID-19 pandemic, only tests without oxygen and one test saturated with oxygen were completed.

### 4.1 Test materials and material preparation

The same materials and sample preparation were used for the anodic CPP and OCP tests. The chemical composition of 316L and DSS used are included in Table 4.1 and Table 4.2, respectively. Material certificate for 316L is provided in Appendix A.1 and for DSS in Appendix A.2.  $PRE_N$  for the materials calculated according to Equation 2.1 are presented in Table 4.3.

**Table 4.1:** Chemical composition of AISI 316L stainless steel [wt%] used in the experiments.

| C     | Si   | Mn   | P     | S      | Cr   | Ni   | Mo   | N     |
|-------|------|------|-------|--------|------|------|------|-------|
| 0.018 | 0.46 | 1.29 | 0.034 | <0.001 | 17.0 | 10.6 | 2.52 | 0.052 |

**Table 4.2:** Chemical composition of 22% Cr duplex stainless steel [wt%] used in the experiments.

| C     | Si   | Mn   | P     | S     | Cr    | Ni   | Mo   | Nb    | Cu   | Co    | N     |
|-------|------|------|-------|-------|-------|------|------|-------|------|-------|-------|
| 0.018 | 0.34 | 1.33 | 0.027 | 0.001 | 22.53 | 5.68 | 3.15 | 0.011 | 0.30 | 0.130 | 0.178 |

**Table 4.3:** Calculated  $PRE_N$  values for the test materials.

| Material | $PRE_N$ |
|----------|---------|
| 316L     | 26,15   |
| DSS      | 35,77   |

316L and DSS were delivered as plates from the manufacturer, Outokumpu. Each sample was 41x41 mm. The 316L samples had a thickness of 2 mm and DSS of 3 mm. Each sample had a drilled hole with diameter of 1 mm. This hole was used to attach a platinum wire to mount the sample in the polarization cell. Each sample also had a 7 mm hole in the center for the crevice former, as illustrated in Figure 4.1 and Figure 4.2.

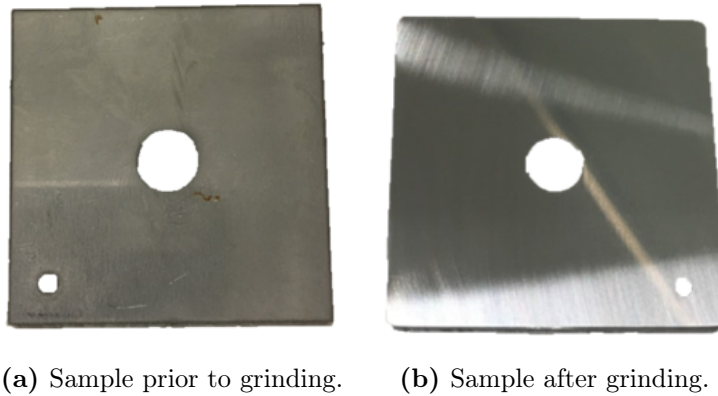


**Figure 4.1:** 316L samples used in the experiments

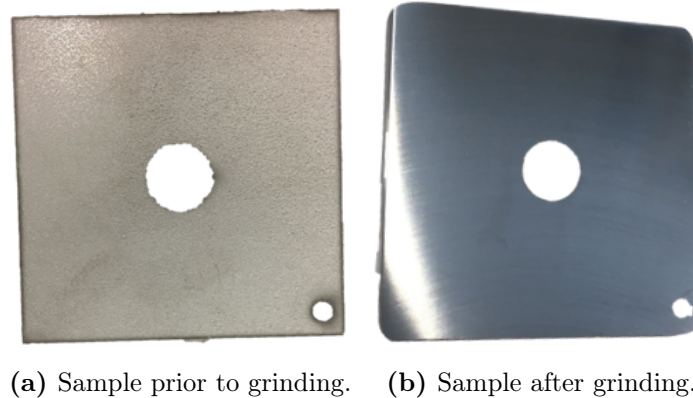


**Figure 4.2:** DSS samples used in the experiments

Prior to the experiments, all samples were wet grinded with 80-500 grit SiC-paper. By starting at the roughest paper, the samples were grinded until previous rough scratches were removed, and the edges were rounded off. Finally, the samples were wet polished with 500 grit SiC-paper. Prior to assembly, the samples were degreased with soap water, water and distilled water, and in an ultrasonic bath using acetone. They were then dried and stored in an exicator overnight. This was to ensure that the passive film was restored before initiating the experiments. Before testing, the samples were also weighed, and the lengths and thickness were measured.

To obtain the current density, the area of the working electrode, the sample, was calculated before the experiments were conducted, according to Equation 4.1:

$$A = 2l_1l_2 + 2l_1t + 2l_2t - 2\pi r_1^2 - 2\pi r_2^2 \quad (4.1)$$

Where  $l_1$  and  $l_2$  are the lengths of the sample,  $t$  is the thickness,  $r_1$  is the radius of the hole in the middle for the crevice former and  $r_2$  is the radius of the little hole for the Pt-string, as pictured in Figure 4.1 and Figure 4.2. This was the procedure in setup 1.

In setup 2, the area of the working electrode used to obtain the current density was changed to the area of the sample that was covered by the crevice former. This change was made because this area is the active surface area, and not the whole sample. The area of the sample covered by the crevice former was calculated according to Equation 4.2:

$$A = 2\pi d_{former}t_{former} \quad (4.2)$$

Where  $d_{former}$  is the diameter of the crevice former and  $t_{former}$  is the thickness of the crevice former. It is multiplied by two since the former covers both sides of the sample.

## 4.2 ASTM G61

An experimental procedure according to ASTM G61 [52] was conducted to record the anodic CPP curves and to obtain the OCP,  $E_{corr}$ ,  $E_{crev}$ ,  $E_{rep}$  and  $i_{pass}$ . OCP and corrosion potential refers to the same potential, but the OCP was measured prior to the polarization scan and the corrosion potential was obtained from the anodic CPP curves as described in Section 2.6.1. The scan started 100 mV below the OCP measured prior to the test. The parameters obtained from the curves were used to compare the corrosion properties at different test conditions, and evaluate the effect of temperature, chloride content and pH.

### 4.2.1 Chemicals and test conditions

The polarization cell should be similar to the one described in G5 [77]; with a cell capacity of about 1 L with suitable necks or seals for the electrodes, gas inlet and outlet, thermometer and pH-meter.

The working electrode (WE) was a 316L or DSS rectangular plate, the reference electrode (RE) was an Ag/AgCl electrode saturated with KCl and the counter electrode (CE) was a platinum wire in setup 1 and a graphite rod in setup 2. A salt bridge was used to separate the bulk solution from the reference electrode (RE) in setup 1. In setup 2, RE was placed in a glass holder placed directly in the electrolyte. Gamry Interface 1000 potentiostat was used to record the curves and maintain the pre-set electrode potential. Electrolytes with chloride concentrations 600 ppmw, 5000 ppmw and 120 000 ppmw, stated as ppm further on in the thesis, at 30 °C and 95 °C were selected as test conditions. Two tests at each condition were carried out. The electrolytes were purged with either N<sub>2</sub> or CO<sub>2</sub> gas to remove the oxygen and to obtain different pH values. The test conditions are presented in Table 4.4.

**Table 4.4:** Test conditions used to record the anodic CPP curves.

| Test condition | Cl <sup>-</sup> conc. [ppm] | Temperature [°C] | Type of gas     |
|----------------|-----------------------------|------------------|-----------------|
| 1              | 600                         | 30               | N <sub>2</sub>  |
| 2              | 600                         | 95               | N <sub>2</sub>  |
| 3              | 600                         | 30               | CO <sub>2</sub> |
| 4              | 600                         | 95               | CO <sub>2</sub> |
| 5              | 5000                        | 30               | N <sub>2</sub>  |
| 6              | 5000                        | 95               | N <sub>2</sub>  |
| 7              | 5000                        | 30               | CO <sub>2</sub> |
| 8              | 5000                        | 95               | CO <sub>2</sub> |
| 9              | 120 000                     | 30               | N <sub>2</sub>  |
| 10             | 120 000                     | 95               | N <sub>2</sub>  |
| 11             | 120 000                     | 30               | CO <sub>2</sub> |
| 12             | 120 000                     | 95               | CO <sub>2</sub> |

Due to the COVID-19 pandemic, test condition 5 was only carried with 316L and test condition 7 was not carried out with either of the materials. The choice to prioritize the other test parameters was made on the basis of DOE; the maximum and minimum level for each parameter were prioritized. A screening method similar to a full factorial design was thereby used in this thesis.

#### 4.2.2 Crevice assembly

During experiments regarding crevice corrosion, crevice formers or in particular the multiple crevice assembly (MCA) are used. A MCA consists of several plateaus and hollows, which creates a serrated pattern. This is to create several crevice initiation sites at one sample, which enables statistical analysis with fewer parallel tests [49].

As a part of the CREVCORR-project, a project to develop a qualification test for crevice corrosion of stainless steels in marine environments [78], a disc spring multiple crevice assembly (DSMCA) was concluded to be the most suitable artificial crevice former [79], presented in Figure 4.3.

A crevice assembly similar to this was used during the experiments. The crevice assembly used in the experiments consisted of titanium washers, bolt and nut, a PVC tube as insulating sleeve, disc spring and centralizing ring, and PEEK crevice formers.

#### 4.2.3 Procedure and apertures

After sample preparation, the sample was mounted to the crevice assembly and the electrode holder. The samples were assembled as illustrated in Figure 4.3 and tightened by applying a torque, using 2 Nm. After preparing the sodium chloride solution by dissolving NaCl in distilled water, the test solution was transferred to the polarization cell. The electrode holder was then placed in the polarization cell. The sample was kept above the solution level, at any time. Finally, the counter electrode, the salt-bridge

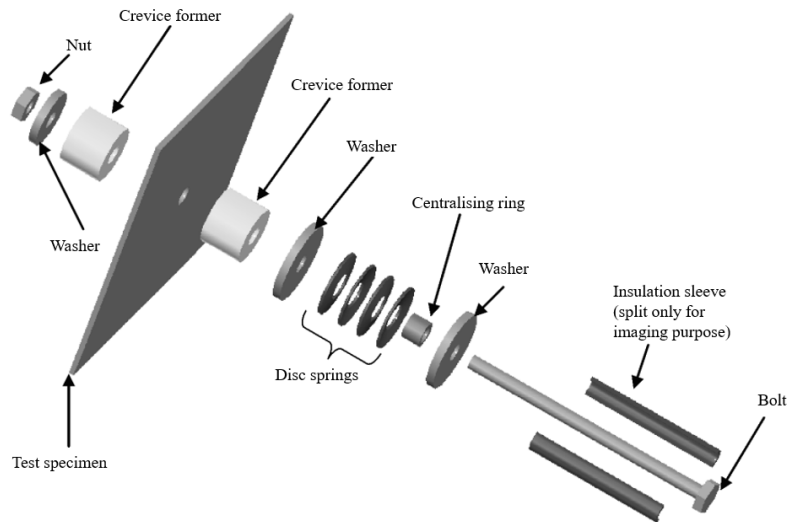


**Figure 4.3:** Illustration of the DSMCA [79].

probe/reference electrode, thermometer, the cooler and the gas inlet/outlet were placed in the test cell.

Oxygen was removed by purging the solution sufficiently (minimum one hour) with  $N_2$ -gas before immersing the specimen. The tests purged with  $CO_2$  were first purged with  $N_2$ -gas for one hour to remove the oxygen and then with  $CO_2$  gas for 30 min to stabilize the pH in the electrolyte. All inlets were sealed to avoid oxygen ingress during the test. The temperature of the solution was brought up to the desired level before the sample was immersed, by using a hotplate. The oxygen content was measured prior to immersion, as well as during the test by using Fibox 3 LCD-trace Oxygen Meter, to make sure it was no oxygen in the electrolyte. Purging the solution with  $N_2$  gas or  $CO_2$  gas was continued during each test to make sure there was no dissolved oxygen in the electrolyte throughout the experiment.

Setup 2 is presented schematically in Figure 4.4, and an image of the experimental setup is presented in Figure 4.5. Only setup 2 is presented, as this was the setup used in this thesis.

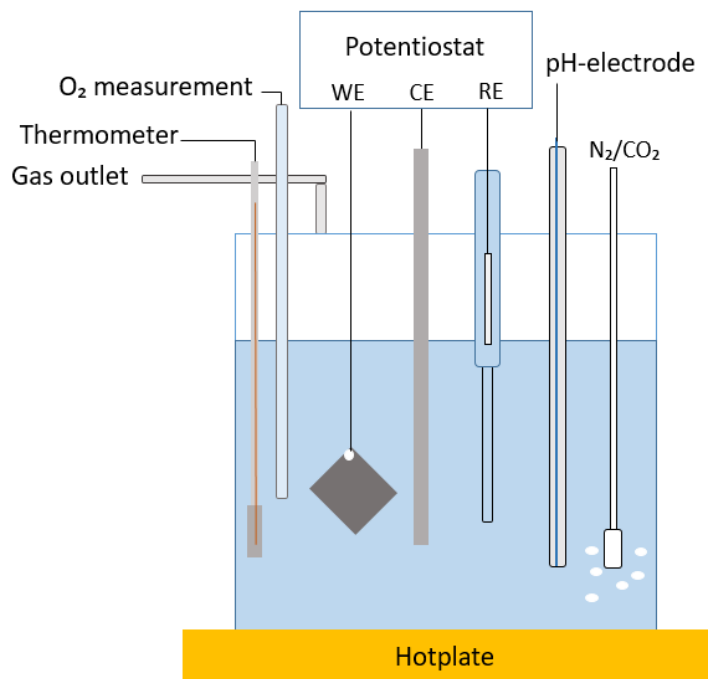


**Figure 4.4:** Schematic illustration of setup 2 used to record anodic CPP curves, made by the author.

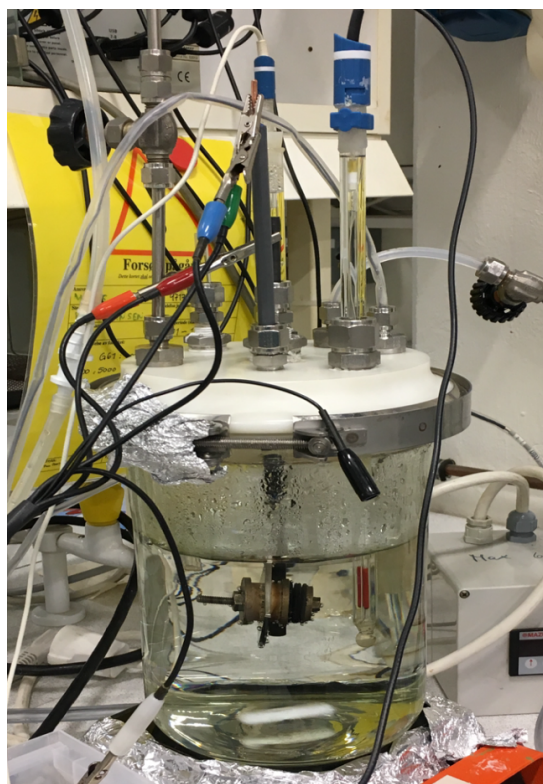


**Figure 4.5:** Image of setup 2 used to record anodic CPP curves.

The sample was immersed for one hour before initiating polarization. OCP was recorded during this hour and the potential scan began at 100mV below the measured OCP. The



potential was scanned in anodic direction, at a scan rate of 0.6 V/h. The current was recorded continuously, and the change in current with potential was plotted. In the project thesis and thereby during the tests conducted with setup 1, the scanning direction was reversed when the current reached 0,1 mA. At some of the test conditions no or shallow attacks were observed on the samples. In this thesis the scanning direction was reversed when the current reached 5 mA and only the area of the sample covered by the crevice former were considered as WE area, as stated earlier. The scan was reversed at a higher current to make sure the corrosion attacks became more evident. The scan was continued until the hysteresis loop was closed or the corrosion potential was reached. The anodic polarization data were then plotted. These curves are referred to as the anodic CPP curves and OCP,  $E_{corr}$ ,  $E_{crev}$ ,  $E_{rep}$  and  $i_{pass}$  were obtained from these curves.

#### 4.2.4 Differences between the two setups

As mentioned, two setups were used during the experiments. In setup 1, the pH was measured before and after the test. While in setup 2, a pH-electrode was placed in the test cell, which enabled recording of the pH during the test from start to finish. It was necessary to be able to control the pH-value during the test when the effect of change in pH was investigated. This change in setup was therefor conducted. Setup 1 was used for the tests with 316L purged with N<sub>2</sub>, while setup 2 was used for the other tests.

The counter electrode was also changed from platinum wire in setup 1, to a graphite rod in setup 2. In setup 1, the reference electrode was connected through a salt-bridge, while in setup 2, it was in a glass holder placed directly in electrolyte. The cell capacity was increased, from 1L to 3L, and it was decided to not use a cooler in setup 2.

### 4.3 Open circuit potential measurements

By conducting OCP measurements at selected test conditions with specific oxygen concentrations, the corrosion susceptibility of the materials under conditions where oxygen is present, can be investigated. This is done by comparing the results from the OCP measurements with  $E_{crev}$  and  $E_{rep}$  obtained from the CPP curves at the same test condition. When OCP is measured against dissolved oxygen concentration, the oxygen application limit is defined when the OCP equals obtained  $E_{crev}$  or  $E_{rep}$ .

#### 4.3.1 Chemicals and test conditions

The polarization cell is similar to setup 2 used to record the anodic CPP curves, described in Section 4.2. However, the counter electrode (CE) has been removed and replaced with another working electrode (WE). Two samples could thereby be exposed simultaneously. The samples were not mounted to the crevice assembly.

The working electrodes (WE) were 316L and DSS rectangular plates. One sample of each material was tested at the same time. Electrolytes with 120 000 ppm and 600 ppm chloride at 30 °C and 95 °C were chosen as test conditions. One test with 19 000 ppm chloride at 45 °C was conducted as well. The tests were conducted with electrolytes where the oxygen had been removed by purging the solution with N<sub>2</sub>. In addition, one test with

120 000 ppm chloride purged with O<sub>2</sub> was also conducted, the temperature was changed from 95 °C to 60 °C and finally to 30 °C during the test. The test conditions are presented in Table 4.5.

**Table 4.5:** Test conditions used to measure OCP.

| Test number | Cl <sup>-</sup> conc. [ppm] | Temperature [°C] | O <sub>2</sub> content |
|-------------|-----------------------------|------------------|------------------------|
| 1           | 600                         | 30               | 0 ppb                  |
| 2           | 600                         | 95               | 0 ppb                  |
| 3           | 19 000                      | 45               | 0 ppb                  |
| 4           | 120 000                     | 30               | 0 ppb                  |
| 5           | 120 000                     | 95               | 0 ppb                  |
| 6           | 120 000                     | 30, 60, 95       | saturated              |

### 4.3.2 Procedure and apertures

As for ASTM G61, the samples were mounted to the electrode holder and the NaCl solution was prepared and transferred to the polarization cell. The solution were heated to desired temperature by using a hotplate. Before immersion of the samples, the solution was purged with N<sub>2</sub> for approximately 1 hour, to remove the oxygen or purged with O<sub>2</sub> by using an aquarium pump, to saturate the solution with oxygen. The specimens were kept above the solution level until the solution had reached desired temperature and had been purged with gas for minimum 1 hour. A schematic illustration of the test cell is presented in Figure 4.6, and an image of the experimental setup is presented in Figure 4.7.

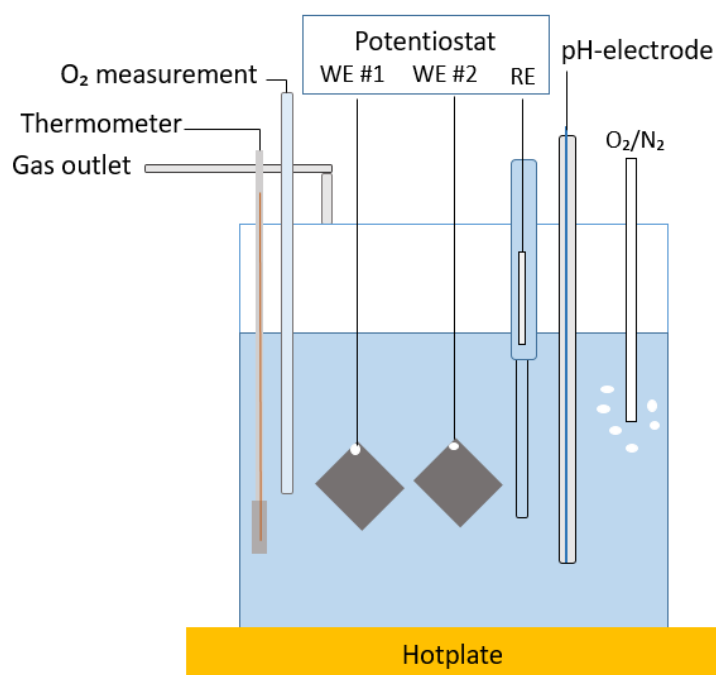


**Figure 4.6:** Schematic illustration of the setup used to record OCP, made by the author.

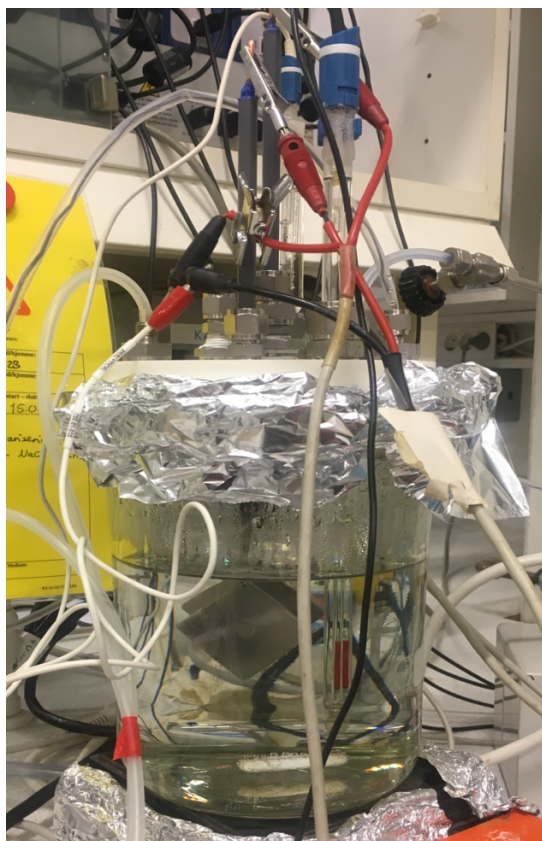


**Figure 4.7:** Image of the experimental setup used to record OCP.

The OCP measurement was started immediately after immersion of the samples, and continued for 48 hours by using logging channels. The oxygen content was measured prior to immersion, as well as during the test by using Fibox 3 LCD-trace Oxygen Meter. Purging of the solution was continued during the test to make sure the oxygen content in the electrolyte was kept as constant as possible.

#### **4.4 Infinite Focus Microscope**

After the anodic CPP measurements were conducted, the samples were examined with an Infinite Focus Microscope (IFM), Alicona's Infinite Focus [80]. To locate and compare the corrosion attacks, IFM was used to examine the samples with a magnification down to 20X. IFM was also used to measure the crevice depth and an example on how this was accomplished is demonstrated in Figure 4.8.

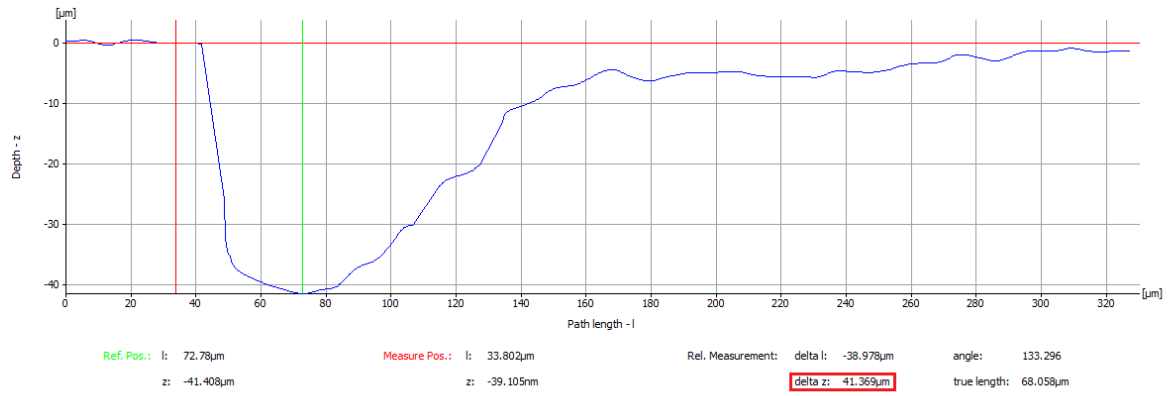


**Figure 4.8:** Example on how to measure crevice depth (stated as delta z) in IFM.

The percentage of the surface consisting of crevices were estimated by analyzing overview images of the samples, taken with IFM. The images were obtained with 5X magnification and analyzed in ImageJ [81].

## 5 Results

The results from the experimental work are presented in the following five sections. The first three sections are dedicated to the investigation of the effect of temperature, chloride concentration and pH. First, the anodic CPP curves according to the test program in Table 4.4 are presented, followed by the parameters obtained from the curves and IFM images of selected samples to illustrate the effect of the different parameters. The results regarding 316L and DSS are presented separately. The following section is dedicated to the surface characterization of the samples exposed to anodic CPP. Finally, the results from the OCP measurements at selected test conditions, with low oxygen content ( $< 10$  ppb) and saturated with oxygen are presented.

The anodic CPP curves were recorded to investigate the effect of different environmental parameters, including temperature, chloride content and pH on crevice corrosion of 316L and DSS. The anodic CPP curves were obtained according to ASTM G61 [52]. The experiments with 316L in electrolytes purged with  $N_2$  were carried out with setup 1 during the specialization project [1] preceding this thesis, and the values obtained from the anodic CPP curves will be reported. All tests with 316L where the electrolyte was purged with  $CO_2$  and all tests with DSS were carried out with setup 2 during this thesis. A few of the test conditions conducted with setup 1 were repeated with setup 2. To illustrate the effect of the different parameters, the same curves will be presented multiple times, but together with different curves each time. For instance, curves obtained with test condition 3 will be presented together with test condition 4 to illustrate the effect of temperature, and together with test condition 11 to illustrate the effect of chloride concentration.

### 5.1 Effect of temperature

To evaluate the effect of temperature, tests at 30 °C and 95 °C were conducted. The temperature was changed, while the electrolyte was purged with the same gas and the chloride concentration was kept constant. Anodic CPP curves were recorded during each test. In this section, these curves in addition to OCP,  $E_{corr}$ ,  $E_{crev}$ ,  $E_{rep}$  and  $i_{pass}$  obtained from the curves will be presented. Both 316L and DSS were tested, and the results for each material are presented separately.

#### 5.1.1 AISI 316L stainless steel

Values for OCP,  $E_{corr}$ ,  $E_{crev}$ ,  $E_{rep}$  and  $i_{pass}$  obtained from the anodic CPP curves from tests conducted during the specialization project [1] preceding this thesis are presented in Table 5.1 - Table 5.3. These results were obtained from the tests where the electrolytes were purged with  $N_2$ .

**Table 5.1:** Parameters obtained from the CPP curves for 316L recorded in electrolytes with 600 ppm chloride and purged with N<sub>2</sub> at different temperatures, all potentials are vs. Ag/AgCl [1].

| Test cond. | Temp.[°C] | OCP[V] | E <sub>corr</sub> [V] | E <sub>crev</sub> [V] | E <sub>rep</sub> [V] | i <sub>pass</sub> [μA/cm <sup>2</sup> ] |
|------------|-----------|--------|-----------------------|-----------------------|----------------------|---|
| 1          | 30        | -0.30  | -0.32                 | 0.39                  | 0.007                | 0.30                                    |
| 1          | 30        | -0.31  | -0.36                 | 0.47                  | -0.044               | 0.24                                    |
| 2          | 95        | -0.58  | -0.60                 | 0.22                  | 0.022                | 0.69                                    |
| 2          | 95        | -0.59  | -0.61                 | 0.25                  | -0.033               | 0.63                                    |

**Table 5.2:** Parameters obtained from the CPP curves for 316L recorded in electrolytes with 5000 ppm chloride and purged with N<sub>2</sub> at different temperatures, all potentials are vs. Ag/AgCl [1].

| Test cond. | Temp.[°C] | OCP[V] | E <sub>corr</sub> [V] | E <sub>crev</sub> [V] | E <sub>rep</sub> [V] | i <sub>pass</sub> [μA/cm <sup>2</sup> ] |
|------------|-----------|--------|-----------------------|-----------------------|----------------------|---|
| 5          | 30        | -0.40  | -0.42                 | 0.240                 | 0.023                | 0.79                                    |
| 5          | 30        | -0.33  | -0.38                 | 0.190                 | -0.073               | 0.26                                    |
| 6          | 95        | -0.59  | -0.60                 | 0.048                 | -0.130               | 0.62                                    |
| 6          | 95        | -0.63  | -0.66                 | 0.039                 | -0.240               | 9.26                                    |

**Table 5.3:** Parameters obtained from the CPP curves for 316L recorded in electrolytes with 120 000 ppm chloride and purged with N<sub>2</sub> at different temperatures, all potentials are vs. Ag/AgCl [1].

| Test cond. | Temp.[°C] | OCP[V] | E <sub>corr</sub> [V] | E <sub>crev</sub> [V] | E <sub>rep</sub> [V] | i <sub>pass</sub> [μA/cm <sup>2</sup> ] |
|------------|-----------|--------|-----------------------|-----------------------|----------------------|---|
| 9          | 30        | -0.35  | -0.41                 | 0.069                 | -0.20                | 0.14                                    |
| 9          | 30        | -0.28  | -0.32                 | 0.067                 | -0.20                | 0.19                                    |
| 10         | 95        | -0.56  | -0.57                 | -0.140                | -0.29                | 0.88                                    |
| 10         | 95        | -0.51  | -0.55                 | -0.140                | -0.19                | 0.57                                    |

All the tests with 316L where the electrolytes were purged with CO<sub>2</sub>, were conducted during this thesis. Anodic CPP curves are presented in Figure 5.1 and Figure 5.2. These tests were conducted with 600 ppm and 120 000 ppm chloride at 30 °C and 95 °C. Corresponding OCP, E<sub>corr</sub>, E<sub>crev</sub>, E<sub>rep</sub> and i<sub>pass</sub> values obtained from the these curves are presented in Table 5.4 and Table 5.5.

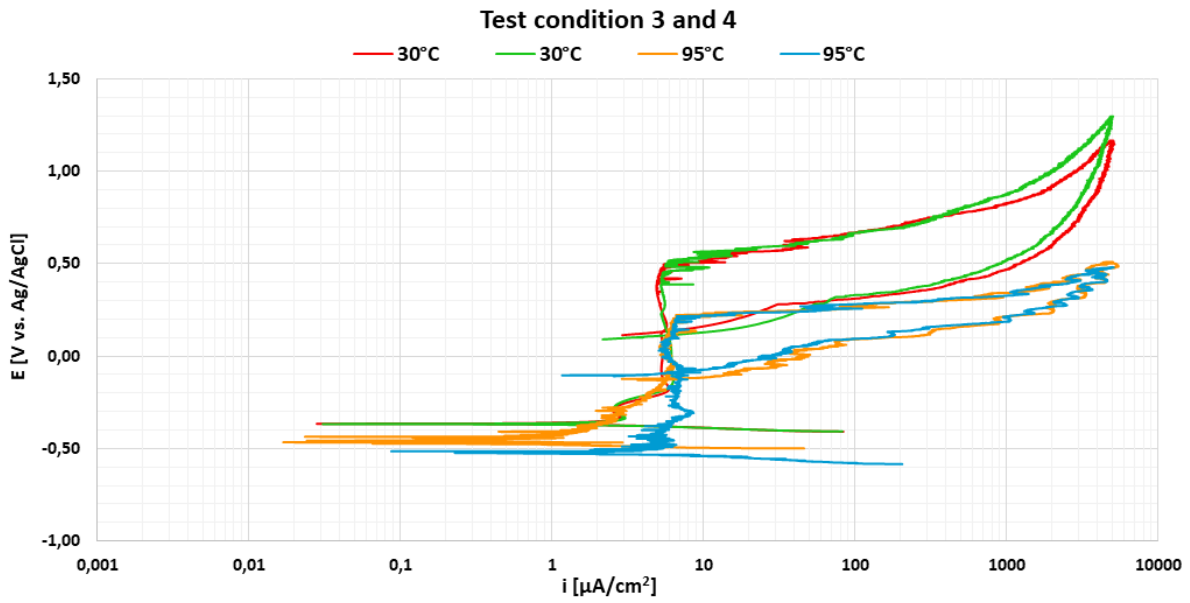


**Figure 5.1:** Anodic CPP curves for 316L obtained in electrolytes with 600 ppm chloride and purged with CO<sub>2</sub> at different temperatures.

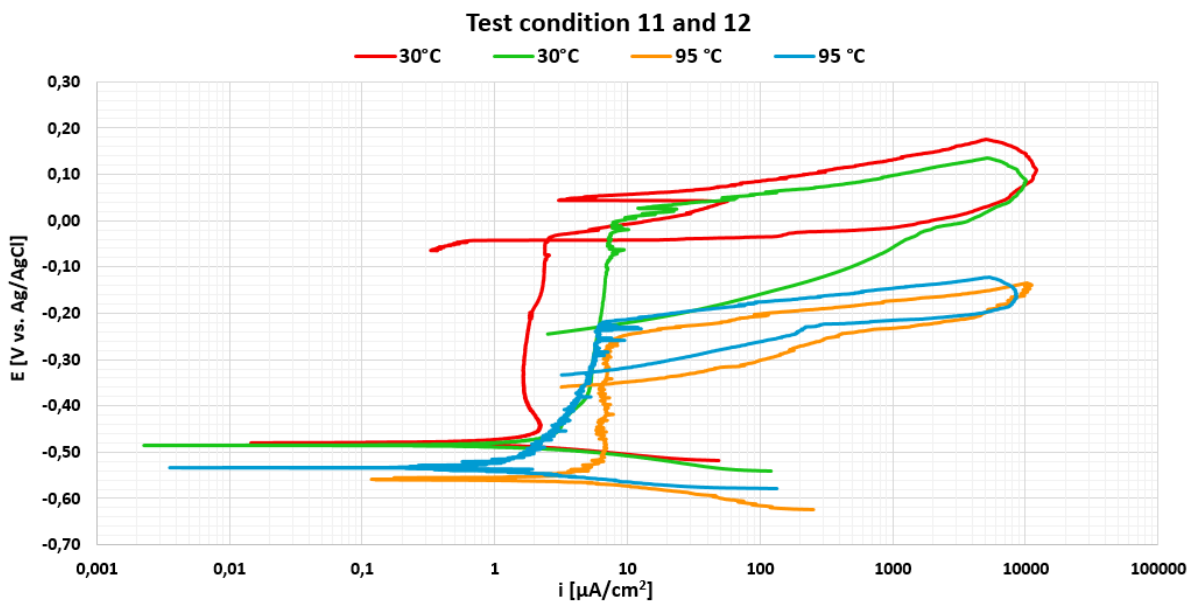


**Figure 5.2:** Anodic CPP curves for 316L obtained in electrolytes with 120 000 ppm chloride and purged with CO<sub>2</sub> at different temperatures.

**Table 5.4:** Parameters obtained from the CPP curves for 316L recorded in electrolytes with 600 ppm chloride and purged with CO<sub>2</sub> at different temperatures, all potentials are vs. Ag/AgCl.

| Test cond. | Temp.[°C] | OCP[V] | E <sub>corr</sub> [V] | E <sub>crev</sub> [V] | E <sub>rep</sub> [V] | i <sub>pass</sub> [μA/cm <sup>2</sup> ] |
|------------|-----------|--------|-----------------------|-----------------------|----------------------|---|
| 3          | 30        | -0.31  | -0.37                 | 0.50                  | 0.13                 | 5.20                                    |
| 3          | 30        | -0.31  | -0.37                 | 0.52                  | 0.11                 | 6.12                                    |
| 4          | 95        | -0.40  | -0.47                 | 0.21                  | -0.13                | 4.21                                    |
| 4          | 95        | -0.48  | -0.52                 | 0.21                  | -0.08                | 6.25                                    |

**Table 5.5:** Parameters obtained from the CPP curves for 316L recorded in electrolytes with 120 000 ppm chloride and purged with CO<sub>2</sub> at different temperatures, all potentials are vs. Ag/AgCl.

| Test cond. | Temp.[°C] | OCP[V] | E <sub>corr</sub> [V] | E <sub>crev</sub> [V] | E <sub>rep</sub> [V] | i <sub>pass</sub> [μA/cm <sup>2</sup> ] |
|------------|-----------|--------|-----------------------|-----------------------|----------------------|---|
| 11         | 30        | -0.42  | -0.48                 | -0.035                | -0.04                | 1.71                                    |
| 11         | 30        | -0.44  | -0.49                 | -0.001                | -0.23                | 5.70                                    |
| 12         | 95        | -0.52  | -0.56                 | -0.260                | -0.35                | 7.09                                    |
| 12         | 95        | -0.48  | -0.53                 | -0.220                | -0.33                | 4.61                                    |

Images of 316L sample surfaces subjected to anodic CPP at 30 °C and 95 °C are presented in Figure 5.3. The images were obtained with IFM with 5X magnification. Only image of the side of the sample with the most severe corrosion attacks is presented. As observed in Figure 5.3, the sample tested at 30 °C has experienced much more severe corrosion attacks than the sample tested at 95 °C. This will be further discussed in Section 6.1.

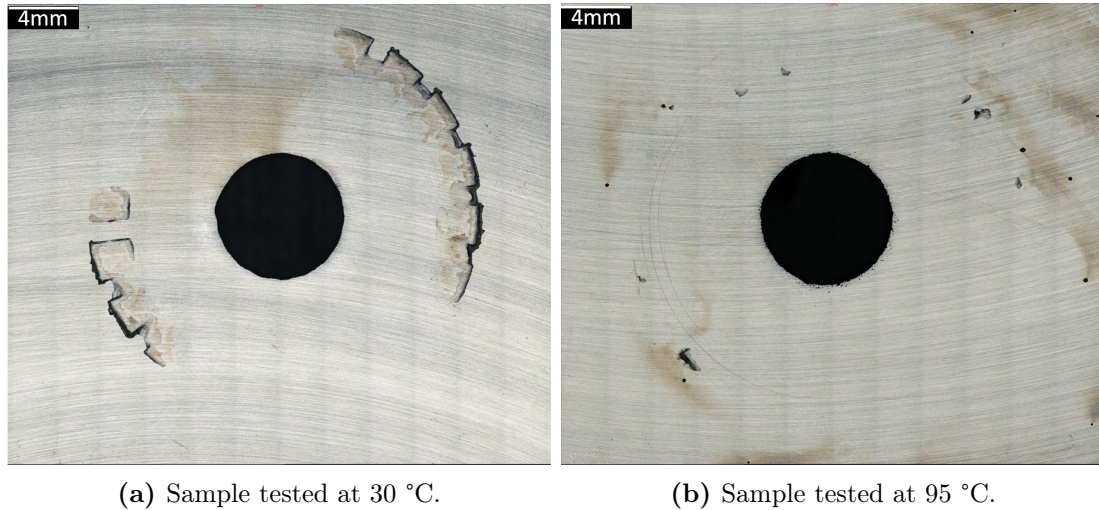


**Figure 5.3:** Images of 316L samples after anodic CPP conducted at different temperatures in electrolytes with 120 000 ppm chloride and purged with CO<sub>2</sub>, obtained with IFM with 5X magnification.



### 5.1.2 22% Cr duplex stainless steel

Anodic CPP curves recorded during tests with DSS at different temperatures are presented in Figure 5.4 - Figure 5.7. The electrolytes were purged with N<sub>2</sub> or CO<sub>2</sub> and the chloride concentration was 600 ppm or 120 000 ppm chloride. The parameters obtained from the curves are presented in Table 5.6 - Table 5.9.

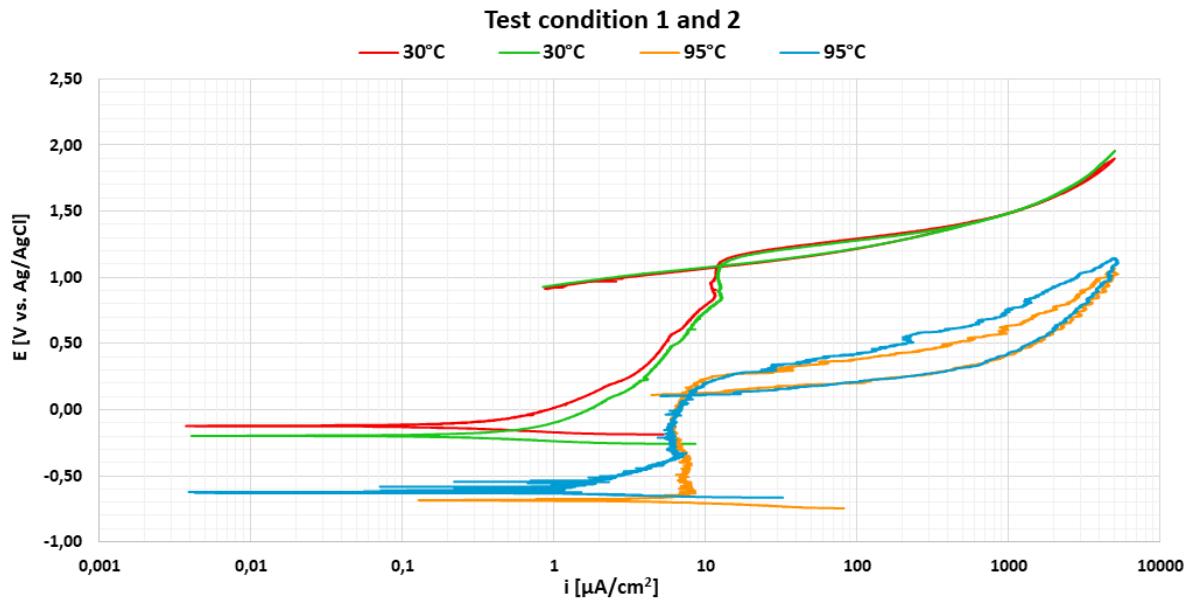


**Figure 5.4:** Anodic CPP curves for DSS obtained in electrolytes with 600 ppm chloride and purged with N<sub>2</sub> at different temperatures.

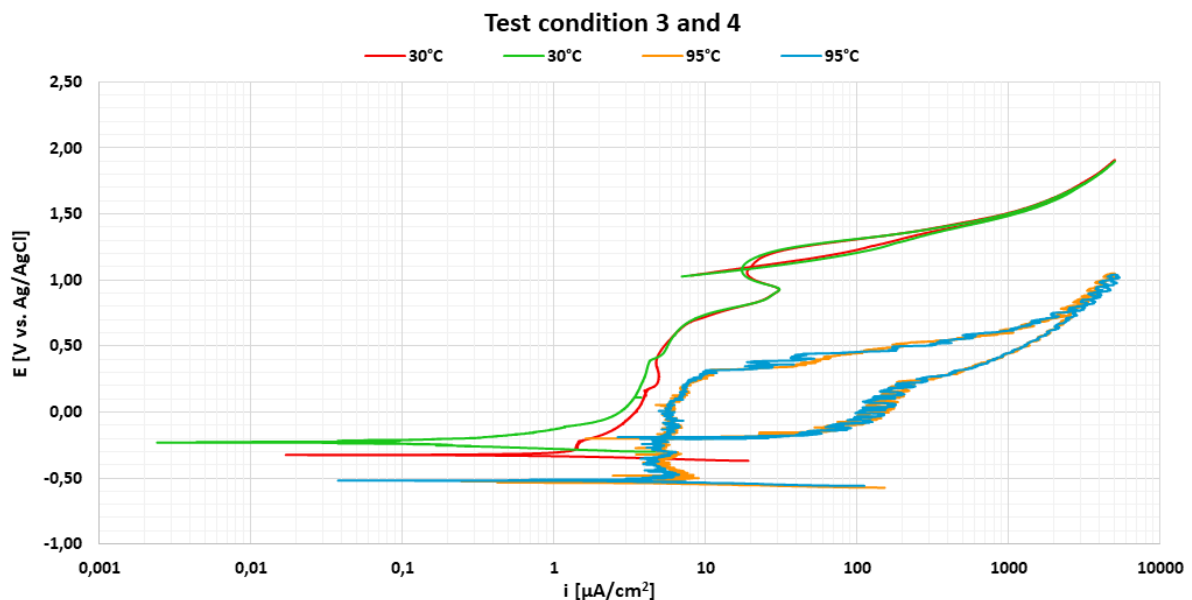


**Figure 5.5:** Anodic CPP curves for DSS obtained in electrolytes with 600 ppm chloride and purged with CO<sub>2</sub> at different temperatures.

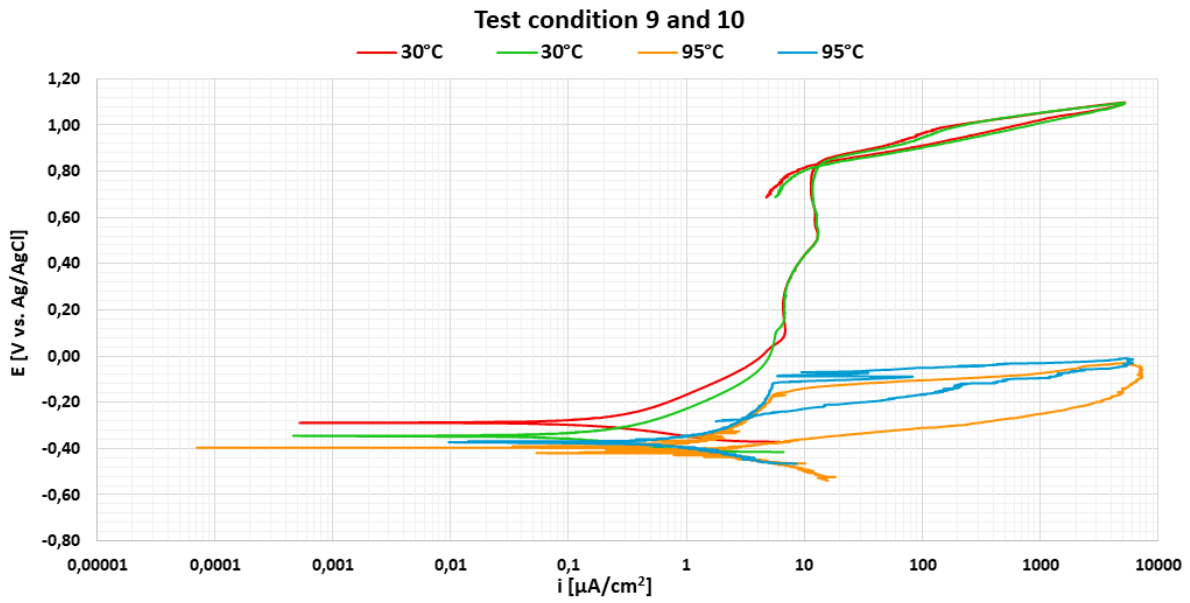


**Figure 5.6:** Anodic CPP curves for DSS obtained in electrolytes with 120 000 ppm chloride and purged with  $\text{N}_2$  at different temperatures.

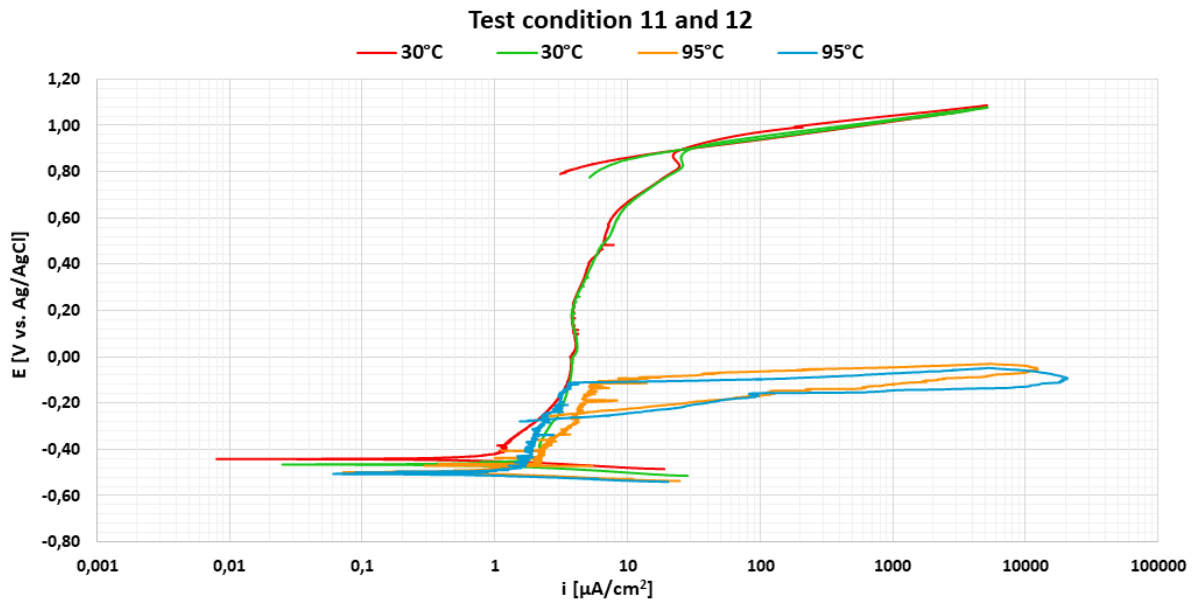


**Figure 5.7:** Anodic CPP curves for DSS obtained in electrolytes with 120 000 ppm chloride and purged with  $\text{CO}_2$  at different temperatures.

**Table 5.6:** Parameters obtained from the CPP curves for DSS recorded in electrolytes with 600 ppm chloride and purged with N<sub>2</sub> at different temperatures, all potentials are vs. Ag/AgCl.

| Test cond. | Temp. [°C] | OCP[V] | E <sub>corr</sub> [V] | E <sub>crev</sub> [V] | E <sub>rep</sub> [V] | i <sub>pass</sub> [μA/cm <sup>2</sup> ] |
|------------|------------|--------|-----------------------|-----------------------|----------------------|---|
| 1          | 30         | -0.087 | -0.12                 | 1.17                  | 1.08                 | 5.20                                    |
| 1          | 30         | -0.16  | -0.20                 | 1.17                  | 1.09                 | 5.31                                    |
| 2          | 95         | -0.65  | -0.69                 | 0.25                  | 0.12                 | 7.04                                    |
| 2          | 95         | -0.57  | -0.63                 | 0.26                  | 0.11                 | 6.67                                    |

**Table 5.7:** Parameters obtained from the CPP curves for DSS recorded in electrolytes with 600 ppm chloride and purged with CO<sub>2</sub> at different temperatures, all potentials are vs. Ag/AgCl.

| Test cond. | Temp. [°C] | OCP[V] | E <sub>corr</sub> [V] | E <sub>crev</sub> [V] | E <sub>rep</sub> [V] | i <sub>pass</sub> [μA/cm <sup>2</sup> ] |
|------------|------------|--------|-----------------------|-----------------------|----------------------|---|
| 3          | 30         | -0.27  | -0.33                 | 1.20                  | 1.10                 | 5.65                                    |
| 3          | 30         | -0.20  | -0.23                 | 1.20                  | 1.08                 | 5.61                                    |
| 4          | 95         | -0.47  | -0.52                 | 0.31                  | 0.11                 | 5.90                                    |
| 4          | 95         | -0.46  | -0.52                 | 0.31                  | 0.11                 | 6.04                                    |

**Table 5.8:** Parameters obtained from the CPP curves for DSS recorded in electrolytes with 120 000 ppm chloride and purged with N<sub>2</sub> at different temperatures, all potentials are vs. Ag/AgCl.

| Test cond. | Temp. [°C] | OCP[V] | E <sub>corr</sub> [V] | E <sub>crev</sub> [V] | E <sub>rep</sub> [V] | i <sub>pass</sub> [μA/cm <sup>2</sup> ] |
|------------|------------|--------|-----------------------|-----------------------|----------------------|---|
| 9          | 30         | -0.27  | -0.29                 | 0.84                  | 0.83                 | 8.42                                    |
| 9          | 30         | -0.31  | -0.34                 | 0.84                  | 0.82                 | 8.39                                    |
| 10         | 95         | -0.36  | -0.40                 | -0.16                 | -0.36                | 3.42                                    |
| 10         | 95         | -0.37  | -0.37                 | -0.12                 | -0.27                | 3.66                                    |

**Table 5.9:** Parameters obtained from the CPP curves for DSS recorded in electrolytes with 120 000 ppm chloride and purged with CO<sub>2</sub> at different temperatures, all potentials are vs. Ag/AgCl.

| Test cond. | Temp. [°C] | OCP[V] | E <sub>corr</sub> [V] | E <sub>crev</sub> [V] | E <sub>rep</sub> [V] | i <sub>pass</sub> [μA/cm <sup>2</sup> ] |
|------------|------------|--------|-----------------------|-----------------------|----------------------|---|
| 11         | 30         | -0.39  | -0.44                 | 0.90                  | 0.89                 | 5.19                                    |
| 11         | 30         | -0.41  | -0.47                 | 0.91                  | 0.90                 | 5.30                                    |
| 12         | 95         | -0.44  | -0.50                 | -0.11                 | -0.24                | 4.04                                    |
| 12         | 95         | -0.44  | -0.51                 | -0.11                 | -0.27                | 2.64                                    |

Images of the DSS sample surfaces subjected to anodic CPP at 30 °C and 95 °C are presented in Figure 5.8. The images were obtained with IFM with 5X magnification. Only image of the side of the sample with the most severe surface change is presented.

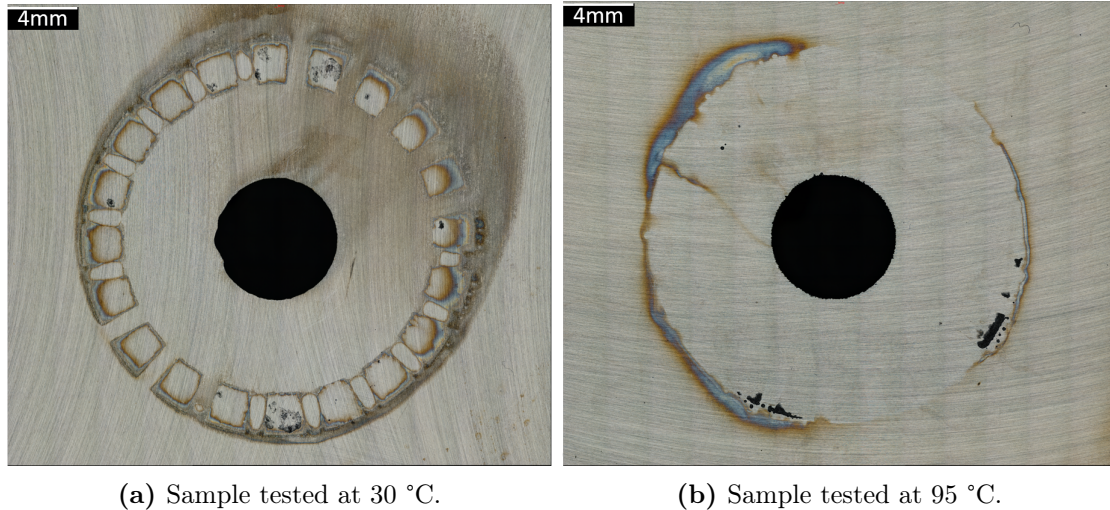


**Figure 5.8:** Images of DSS samples after anodic CPP conducted at different temperatures in electrolytes with 120 000 ppm chloride and purged with  $N_2$ , obtained with IFM with 5X magnification.

## 5.2 Effect of chloride concentration

To evaluate the effect of chloride concentration, tests with electrolytes purged with the same gas type and at constant temperature, but different chloride concentrations were conducted. The chloride concentrations were 600 ppm, 5000 ppm and 120 000 ppm chloride. Anodic CPP curves measured during each test, as well as OCP,  $E_{corr}$ ,  $E_{crev}$ ,  $E_{rep}$  and  $i_{pass}$  obtained from each curve will be presented in this section. Both 316L and DSS were tested, and the results for each material will be presented individually.

### 5.2.1 AISI 316L stainless steel

All tests conducted with 316L with electrolytes purged with  $N_2$ , were conducted in the specialization project [1] preceding this thesis. Values for OCP,  $E_{corr}$ ,  $E_{crev}$ ,  $E_{rep}$  and  $i_{pass}$  obtained from the anodic CPP curves from tests conducted during the specialization project are presented in Table 5.10 and Table 5.11. These results are obtained from the tests conducted with setup 1, with exception of one test conducted at 95 °C and 5000 ppm chloride (test condition 6), presented in Table 5.11. At this test condition it was decided to use the results from one test with setup 1 and one with setup 2, as the results from these tests correlated better than the results from both tests conducted with setup 1 did. As mentioned in Section 4.2, the scanning direction was reversed at a higher current and only the area of the sample covered by the crevice former were considered when calculating the current density for the tests conducted with setup 2. Obtained  $i_{pass}$  for the test conducted with setup 2, presented in Table 5.11 will be higher than the other  $i_{pass}$  values because a smaller WE area was considered.

**Table 5.10:** Parameters obtained from the CPP curves for 316L recorded in electrolytes purged with N<sub>2</sub> at 30 °C with different chloride concentrations, all potentials are vs. Ag/AgCl [1].

| Test cond. | Cl <sup>-</sup> [ppm] | OCP[V] | E <sub>corr</sub> [V] | E <sub>crev</sub> [V] | E <sub>rep</sub> [V] | i <sub>pass</sub> [μA/cm <sup>2</sup> ] |
|------------|-----------------------|--------|-----------------------|-----------------------|----------------------|---|
| 1          | 600                   | -0.30  | -0.32                 | 0.390                 | 0.007                | 0.30                                    |
| 1          | 600                   | -0.31  | -0.36                 | 0.470                 | -0.044               | 0.24                                    |
| 5          | 5000                  | -0.40  | -0.42                 | 0.240                 | 0.023                | 0.79                                    |
| 5          | 5000                  | -0.33  | -0.38                 | 0.190                 | -0.073               | 0.26                                    |
| 9          | 120 000               | -0.35  | -0.41                 | 0.069                 | -0.200               | 0.14                                    |
| 9          | 120 000               | -0.28  | -0.32                 | 0.067                 | -0.200               | 0.19                                    |

**Table 5.11:** Parameters obtained from the CPP curves for 316L recorded in electrolytes purged with N<sub>2</sub> at 95 °C with different chloride concentrations, all potentials are vs. Ag/AgCl [1].

| Test cond. | Cl <sup>-</sup> [ppm] | OCP[V] | E <sub>corr</sub> [V] | E <sub>crev</sub> [V] | E <sub>rep</sub> [V] | i <sub>pass</sub> [μA/cm <sup>2</sup> ] |
|------------|-----------------------|--------|-----------------------|-----------------------|----------------------|---|
| 2          | 600                   | -0.58  | -0.60                 | 0.220                 | 0.022                | 0.69                                    |
| 2          | 600                   | -0.59  | -0.61                 | 0.250                 | -0.033               | 0.63                                    |
| 6          | 5000                  | -0.59  | -0.60                 | 0.048                 | -0.130               | 0.62                                    |
| 6          | 5000                  | -0.63  | -0.66                 | 0.039                 | -0.240               | 9.26                                    |
| 10         | 120 000               | -0.56  | -0.57                 | -0.140                | -0.290               | 0.88                                    |
| 10         | 120 000               | -0.51  | -0.55                 | -0.140                | -0.190               | 0.57                                    |

The curves obtained for 316L when the electrolytes were purged with CO<sub>2</sub> were conducted during the work with this thesis, and are presented in Figure 5.9 and Figure 5.10. The corresponding values for OCP, E<sub>corr</sub>, E<sub>crev</sub>, E<sub>rep</sub> and i<sub>pass</sub> obtained from the curves are presented in Table 5.12 and Table 5.13.

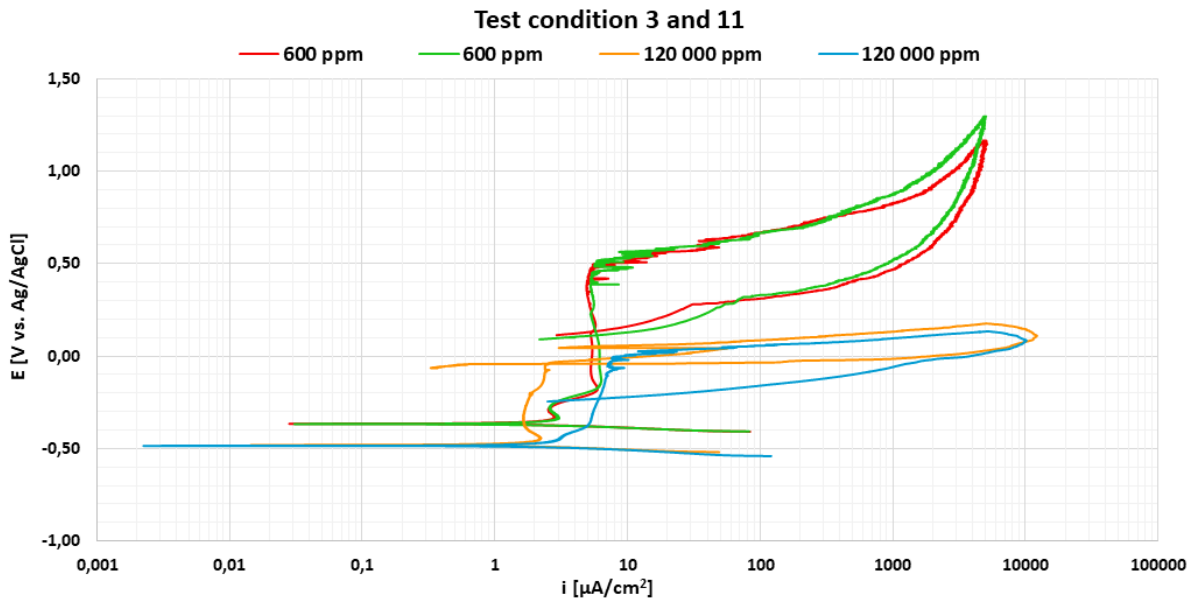


**Figure 5.9:** Anodic CPP curves for 316L obtained in electrolytes purged with  $\text{CO}_2$  at  $30\text{ }^\circ\text{C}$  with different chloride concentrations.

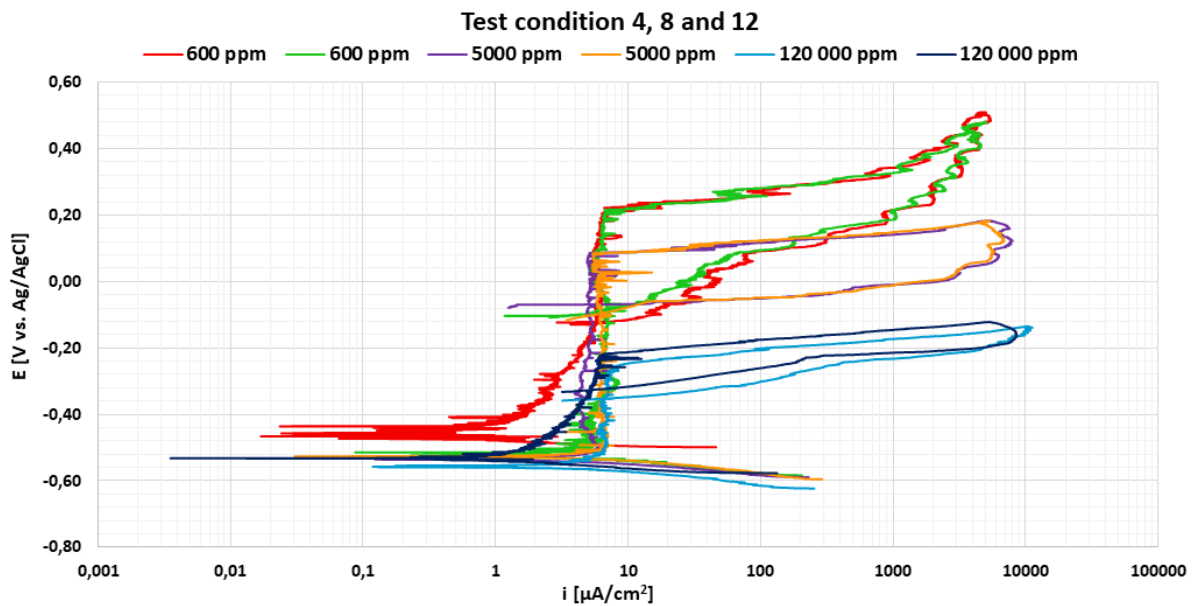


**Figure 5.10:** Anodic CPP curves for 316L obtained in electrolytes purged with  $\text{CO}_2$  at  $95\text{ }^\circ\text{C}$  with different chloride concentrations.

**Table 5.12:** Parameters obtained from the CPP curves for 316L recorded in electrolytes purged with CO<sub>2</sub> at 30 °C with different chloride concentrations, all potentials are vs. Ag/AgCl.

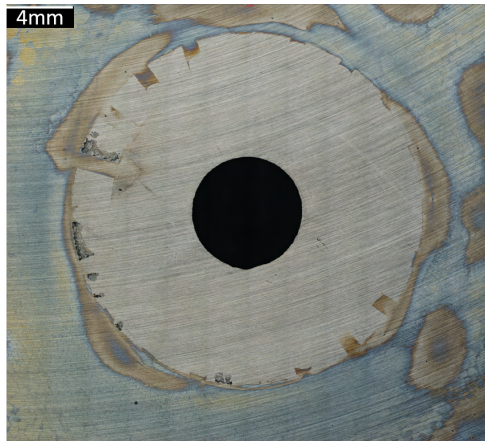
| Test cond. | Cl <sup>-</sup> [ppm] | OCP[V] | E <sub>corr</sub> [V] | E <sub>crev</sub> [V] | E <sub>rep</sub> [V] | i <sub>pass</sub> [μA/cm <sup>2</sup> ] |
|------------|-----------------------|--------|-----------------------|-----------------------|----------------------|---|
| 3          | 600                   | -0.31  | -0.37                 | 0.500                 | 0.13                 | 5.20                                    |
| 3          | 600                   | -0.31  | -0.37                 | 0.520                 | 0.11                 | 6.12                                    |
| 11         | 120 000               | -0.42  | -0.48                 | -0.035                | -0.04                | 1.77                                    |
| 11         | 120 000               | -0.44  | -0.49                 | -0.001                | -0.23                | 5.70                                    |

**Table 5.13:** Parameters obtained from the CPP curves for 316L recorded in solution purged with CO<sub>2</sub> at 95 °C with different chloride concentrations, all potentials are vs. Ag/AgCl.

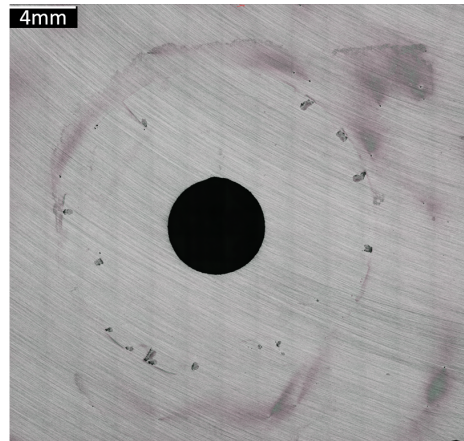
| Test cond. | Cl <sup>-</sup> [ppm] | OCP[V] | E <sub>corr</sub> [V] | E <sub>crev</sub> [V] | E <sub>rep</sub> [V] | i <sub>pass</sub> [μA/cm <sup>2</sup> ] |
|------------|-----------------------|--------|-----------------------|-----------------------|----------------------|---|
| 4          | 600                   | -0.40  | -0.47                 | 0.210                 | -0.130               | 4.21                                    |
| 4          | 600                   | -0.48  | -0.52                 | 0.210                 | -0.083               | 6.25                                    |
| 8          | 5000                  | -0.49  | -0.54                 | 0.082                 | -0.079               | 5.17                                    |
| 8          | 5000                  | -0.50  | -0.53                 | 0.085                 | -0.096               | 6.35                                    |
| 12         | 120 000               | -0.52  | -0.56                 | -0.260                | -0.350               | 7.09                                    |
| 12         | 120 000               | -0.48  | -0.53                 | -0.220                | -0.330               | 4.61                                    |

The curves recorded in electrolytes with 120 000 ppm chloride, presented in Figure 5.9, experienced different course of passivation and E<sub>rep</sub>, obtained from the curves deviates within the parallel. The difference in the results is difficult to explain, but may be due to different chemistry inside the crevices on the two samples.

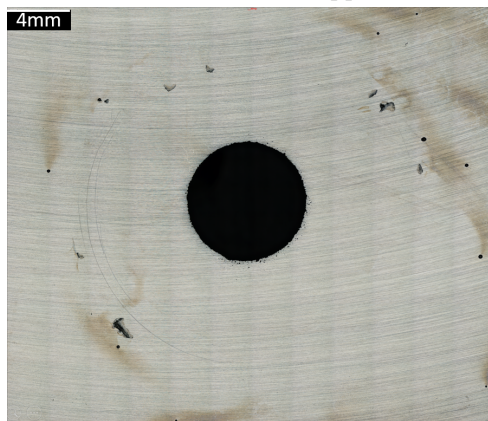
Images of 316L samples tested in electrolytes with different chloride concentrations are presented in Figure 5.11. The images were obtained with IFM with 5X magnification. The side of the sample with the most severe corrosion attacks is presented.



(a) Sample tested in electrolyte with 600 ppm chloride.



(b) Sample tested in electrolyte with 5000 ppm chloride.



(c) Sample tested in electrolyte with 120 000 ppm chloride.

**Figure 5.11:** Images of 316L samples after anodic CPP conducted with different chloride concentrations in electrolytes purged with  $\text{CO}_2$  at  $95\text{ }^\circ\text{C}$ , obtained with IFM with 5X magnification.

### 5.2.2 22% Cr duplex stainless steel

The curves obtained for DSS at constant temperature and purged with the same gas, but with different chloride concentrations are presented in Figure 5.12 - Figure 5.15. At  $30\text{ }^\circ\text{C}$ , only 600 ppm and 120 000 ppm chloride were tested, while at  $95\text{ }^\circ\text{C}$ , 5000 ppm chloride was tested in addition to 600 ppm and 120 000 ppm chloride. The values obtained from the curves are presented in Table 5.14 - Table 5.17. All the tests were conducted with setup 2.



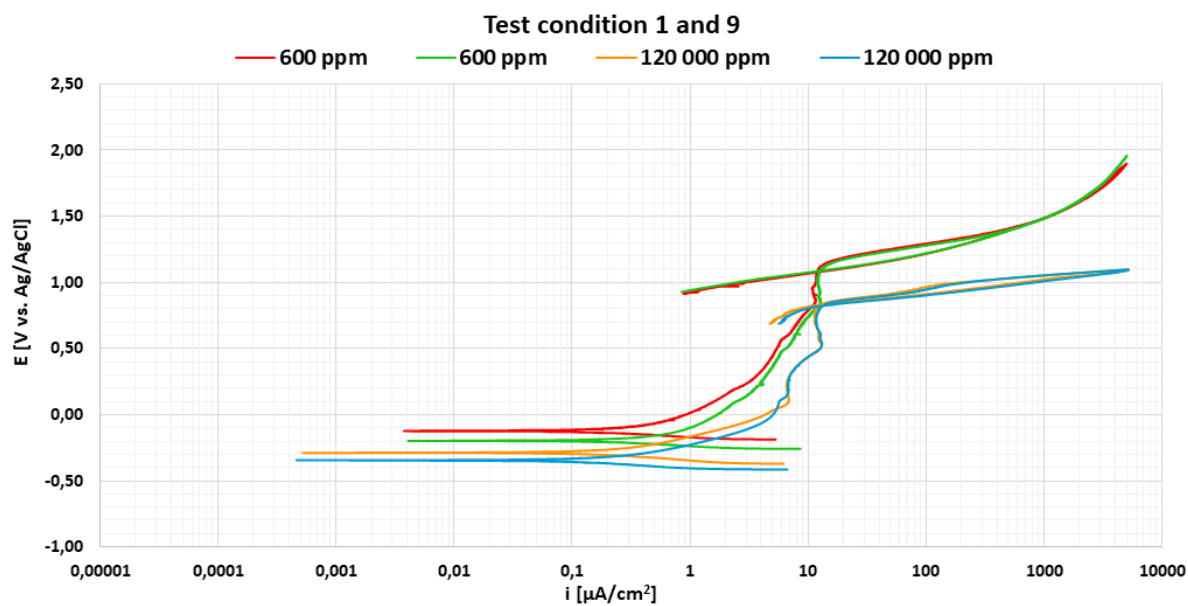


**Figure 5.12:** Anodic CPP curves for DSS obtained in electrolytes purged with  $N_2$  at  $30\text{ }^\circ\text{C}$  with different chloride concentrations.

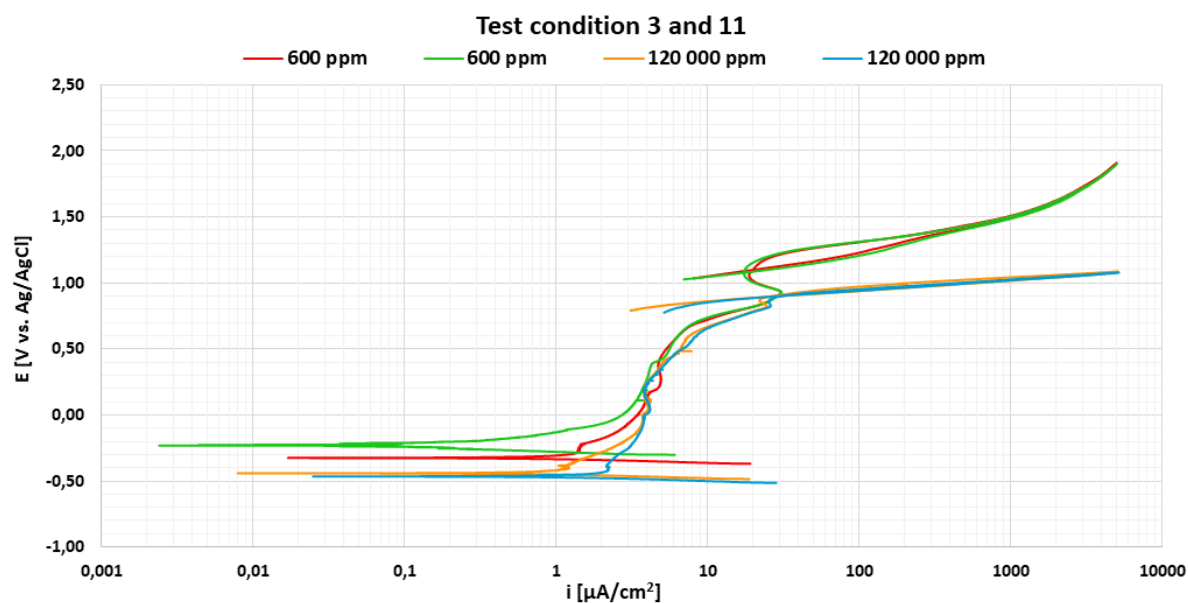


**Figure 5.13:** Anodic CPP curves for DSS obtained in electrolytes purged with  $CO_2$  at  $30\text{ }^\circ\text{C}$  with different chloride concentrations.

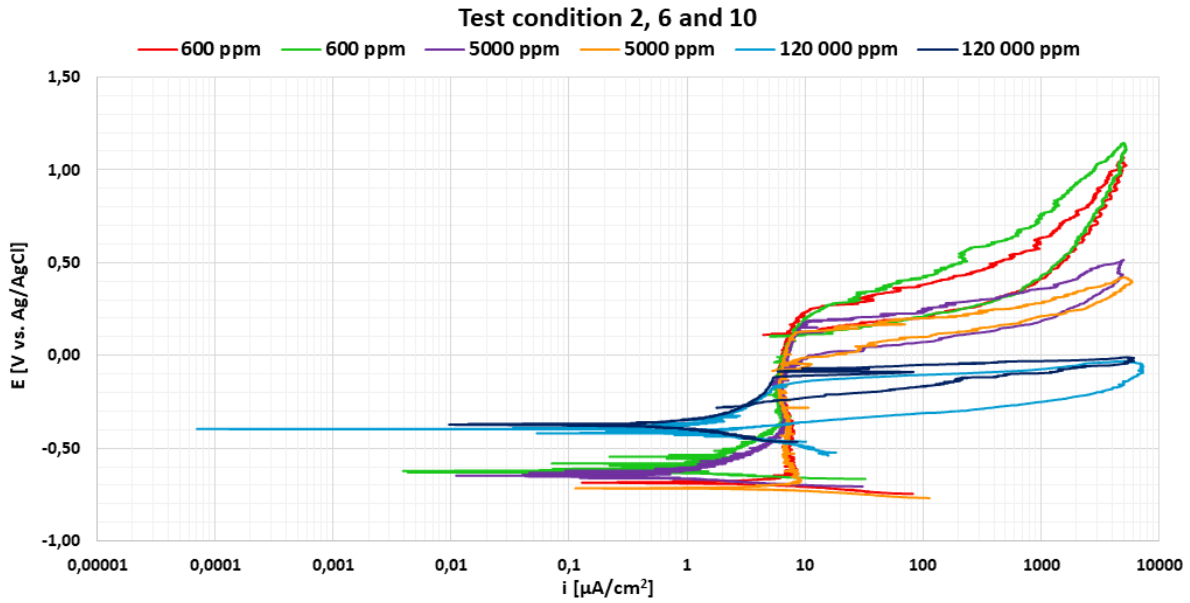


**Figure 5.14:** Anodic CPP curves for DSS obtained in electrolytes purged with  $N_2$  at  $95\text{ }^\circ\text{C}$  with different chloride concentrations.

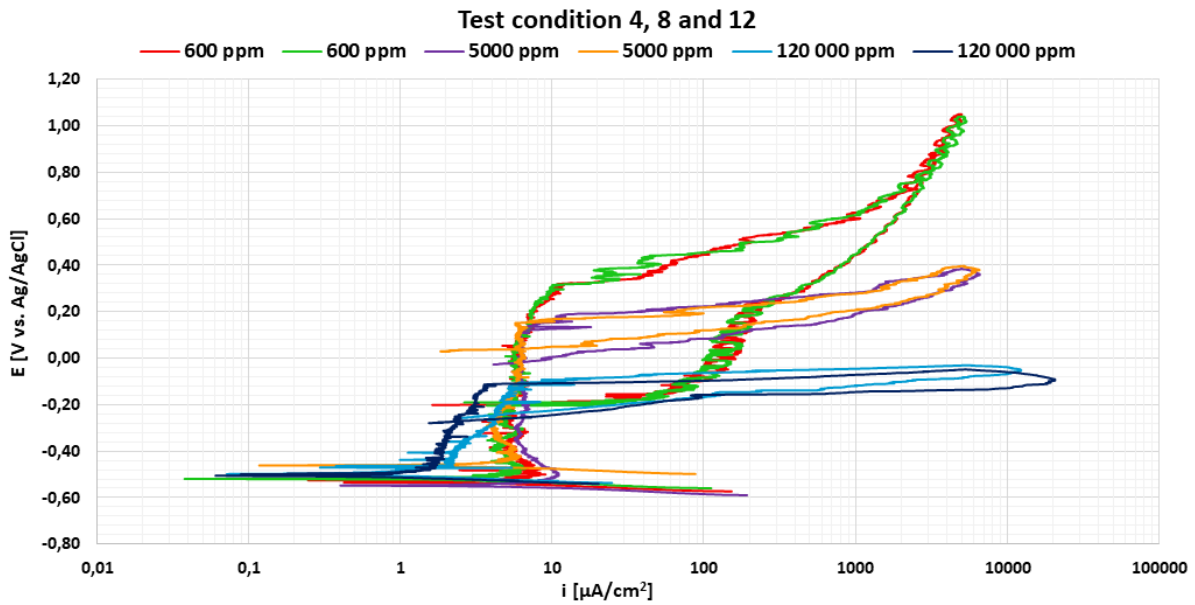


**Figure 5.15:** Anodic CPP curves for DSS obtained in electrolytes purged with  $CO_2$  at  $95\text{ }^\circ\text{C}$  with different chloride concentrations.

**Table 5.14:** Parameters obtained from the CPP curves for DSS recorded in electrolytes purged with  $N_2$  at  $30\text{ }^\circ\text{C}$  with different chloride concentrations, all potentials are vs. Ag/AgCl.

| Test cond. | $Cl^-$ [ppm] | OCP [V] | $E_{corr}$ [V] | $E_{crev}$ [V] | $E_{rep}$ [V] | $i_{pass}$ [ $\mu A/cm^2$ ] |
|------------|--------------|---------|----------------|----------------|---------------|-----------------------------|
| 1          | 600          | -0.087  | -0.12          | 1.17           | 1.08          | 5.20                        |
| 1          | 600          | -0.16   | -0.20          | 1.17           | 1.09          | 5.31                        |
| 9          | 120 000      | -0.27   | -0.29          | 0.84           | 0.83          | 8.42                        |
| 9          | 120 000      | -0.31   | -0.34          | 0.84           | 0.82          | 8.39                        |

**Table 5.15:** Parameters obtained from the CPP curves for DSS recorded in electrolytes purged with CO<sub>2</sub> at 30 °C with different chloride concentrations, all potentials are vs. Ag/AgCl.

| Test cond. | Cl <sup>-</sup> [ppm] | OCP[V] | E <sub>corr</sub> [V] | E <sub>crev</sub> [V] | E <sub>rep</sub> [V] | i <sub>pass</sub> [μA/cm <sup>2</sup> ] |
|------------|-----------------------|--------|-----------------------|-----------------------|----------------------|---|
| 3          | 600                   | -0.27  | -0.33                 | 1.20                  | 1.10                 | 5.65                                    |
| 3          | 600                   | -0.20  | -0.23                 | 1.20                  | 1.08                 | 5.61                                    |
| 11         | 120 000               | -0.39  | -0.44                 | 0.90                  | 0.89                 | 5.19                                    |
| 11         | 120 000               | -0.41  | -0.47                 | 0.91                  | 0.90                 | 5.30                                    |

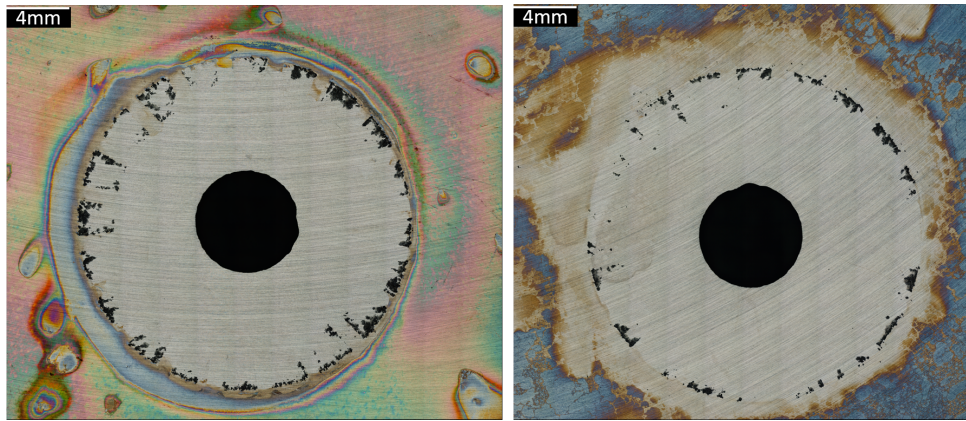
**Table 5.16:** Parameters obtained from the CPP curves for DSS recorded in electrolytes purged with N<sub>2</sub> at 95 °C with different chloride concentrations, all potentials are vs. Ag/AgCl.

| Test cond. | Cl <sup>-</sup> [ppm] | OCP[V] | E <sub>corr</sub> [V] | E <sub>crev</sub> [V] | E <sub>rep</sub> [V] | i <sub>pass</sub> [μA/cm <sup>2</sup> ] |
|------------|-----------------------|--------|-----------------------|-----------------------|----------------------|---|
| 2          | 600                   | -0.65  | -0.69                 | 0.25                  | 0.12                 | 7.04                                    |
| 2          | 600                   | -0.57  | -0.63                 | 0.26                  | 0.11                 | 6.67                                    |
| 6          | 5000                  | -0.61  | -0.65                 | 0.18                  | -0.10                | 6.79                                    |
| 6          | 5000                  | -0.67  | -0.72                 | 0.13                  | -0.08                | 6.33                                    |
| 10         | 120 000               | -0.36  | -0.40                 | -0.16                 | -0.36                | 3.42                                    |
| 10         | 120 000               | -0.37  | -0.37                 | -0.12                 | -0.27                | 3.66                                    |

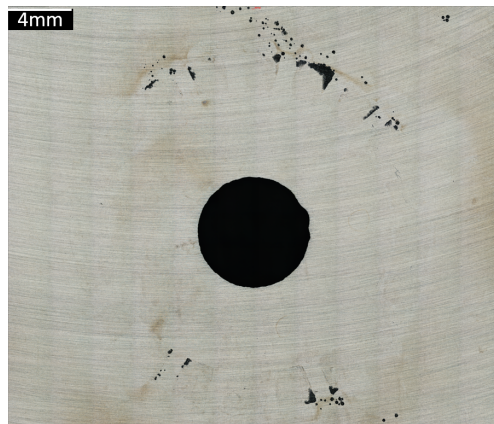
**Table 5.17:** Parameters obtained from the CPP curves for DSS recorded in electrolytes purged with CO<sub>2</sub> at 95 °C with different chloride concentrations, all potentials are vs. Ag/AgCl.

| Test cond. | Cl <sup>-</sup> [ppm] | OCP[V] | E <sub>corr</sub> [V] | E <sub>crev</sub> [V] | E <sub>rep</sub> [V] | i <sub>pass</sub> [μA/cm <sup>2</sup> ] |
|------------|-----------------------|--------|-----------------------|-----------------------|----------------------|---|
| 4          | 600                   | -0.47  | -0.52                 | 0.31                  | 0.11                 | 5.90                                    |
| 4          | 600                   | -0.46  | -0.52                 | 0.31                  | 0.11                 | 6.04                                    |
| 8          | 5000                  | -0.49  | -0.55                 | 0.12                  | -0.02                | 6.50                                    |
| 8          | 5000                  | -0.47  | -0.53                 | 0.13                  | -0.01                | 6.60                                    |
| 12         | 120 000               | -0.44  | -0.50                 | -0.11                 | -0.24                | 4.04                                    |
| 12         | 120 000               | -0.44  | -0.51                 | -0.11                 | -0.27                | 2.64                                    |

Images of DSS samples tested in electrolytes with different chloride concentrations are presented in Figure 5.16. The images were obtained with IFM with 5X magnification. The side of the sample with the most severe corrosion attacks is presented.



(a) Sample tested in electrolyte with 600 ppm chloride. (b) Sample tested in electrolyte with 5000 ppm chloride.



(c) Sample tested in electrolyte with 120 000 ppm chloride.

**Figure 5.16:** Images of DSS samples after anodic CPP conducted with different chloride concentrations in electrolytes purged with  $\text{CO}_2$  at 95 °C, obtained with IFM with 5X magnification.

### 5.3 Effect of pH

To evaluate the effect of pH, tests with electrolytes with different pH values were conducted. The pH was changed by purging the electrolyte with either  $\text{CO}_2$  or  $\text{N}_2$ , as  $\text{CO}_2$  creates a more acidic environment. Measured pH values for the tests purged with  $\text{CO}_2$  were between 4.3 and 5.3. While the tests purged with  $\text{N}_2$  had pH values between 6.6 and 8.5. pH was measured continuously during the tests and had the tendency to increase during the experiment. The pH values are therefore stated as an interval. The chloride concentrations tested were 600 ppm and 120 000 ppm chloride for the tests conducted at 30 °C, and 600 ppm, 5000 ppm and 120 000 ppm chloride for the tests at 95 °C.

The anodic CPP curves measured during the tests and corresponding  $E_{corr}$ ,  $E_{crev}$ ,  $E_{rep}$  and  $i_{pass}$  values obtained from the curves are presented in the following two subsections. The red and green CPP curves represent the tests purged with  $\text{N}_2$ , while the yellow and blue CPP curves represent the tests purged with  $\text{CO}_2$ .

### 5.3.1 AISI 316L stainless steel

Curves recorded during anodic CPP of 316L samples in electrolytes with different pH are presented in Figure 5.17 - Figure 5.21. As mentioned earlier, all the tests with 316L purged with  $N_2$  were conducted during the specialization project [1]. This with the exception of one of the tests with 120 000 ppm at 95 ° (test condition 6), which was conducted during this thesis. To illustrate the effect of pH, the anodic CPP curves obtained during the specialization project and during this thesis will be presented together in this section. All the tests purged with  $CO_2$  were conducted during this thesis. OCP,  $E_{corr}$ ,  $E_{crev}$ ,  $E_{rep}$  and  $i_{pass}$  values obtained from the curves are presented in Table 5.18 - Table 5.22.

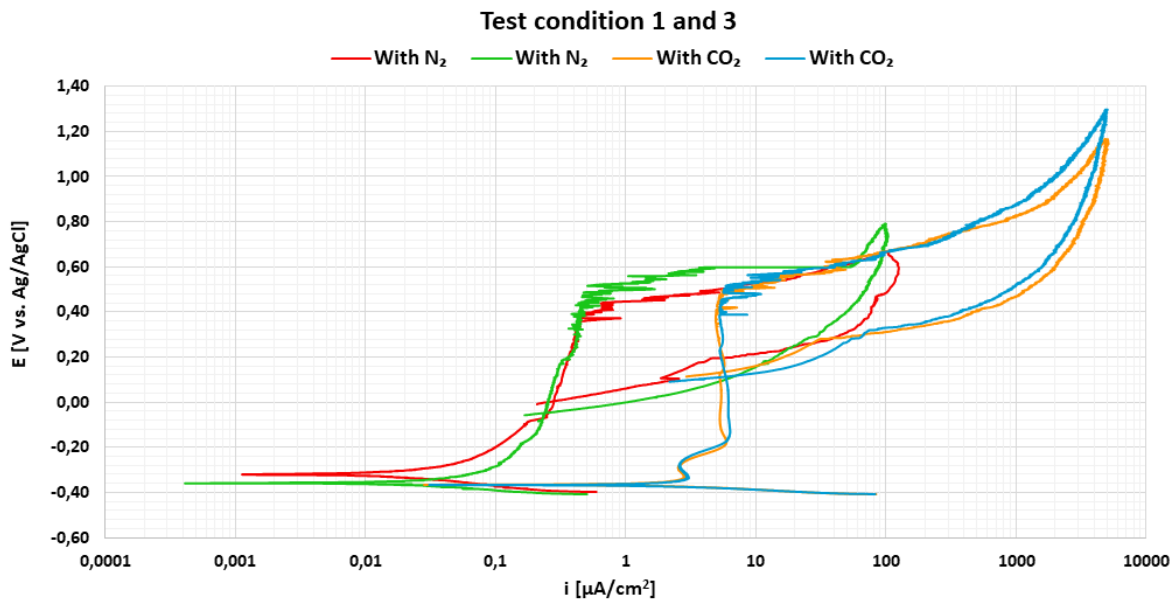


**Figure 5.17:** Anodic CPP curves for 316L obtained in electrolytes with 600 ppm chloride at 30 °C purged with  $N_2$  and  $CO_2$ .

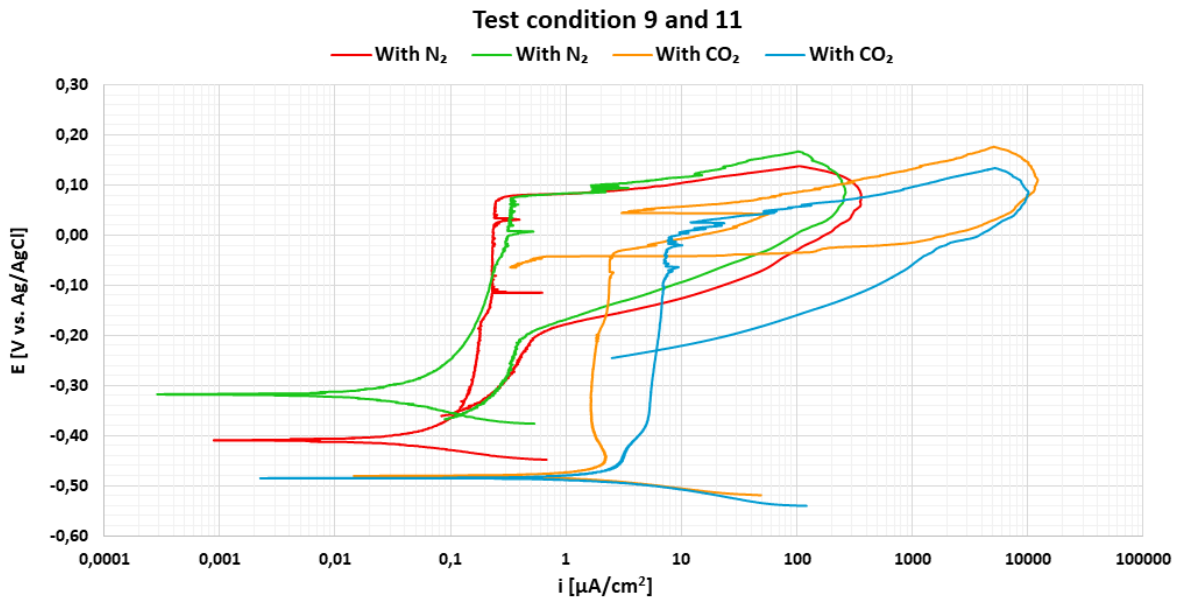


**Figure 5.18:** Anodic CPP curves for 316L obtained in electrolytes with 120 000 ppm chloride at 30 °C purged with N<sub>2</sub> and CO<sub>2</sub>.

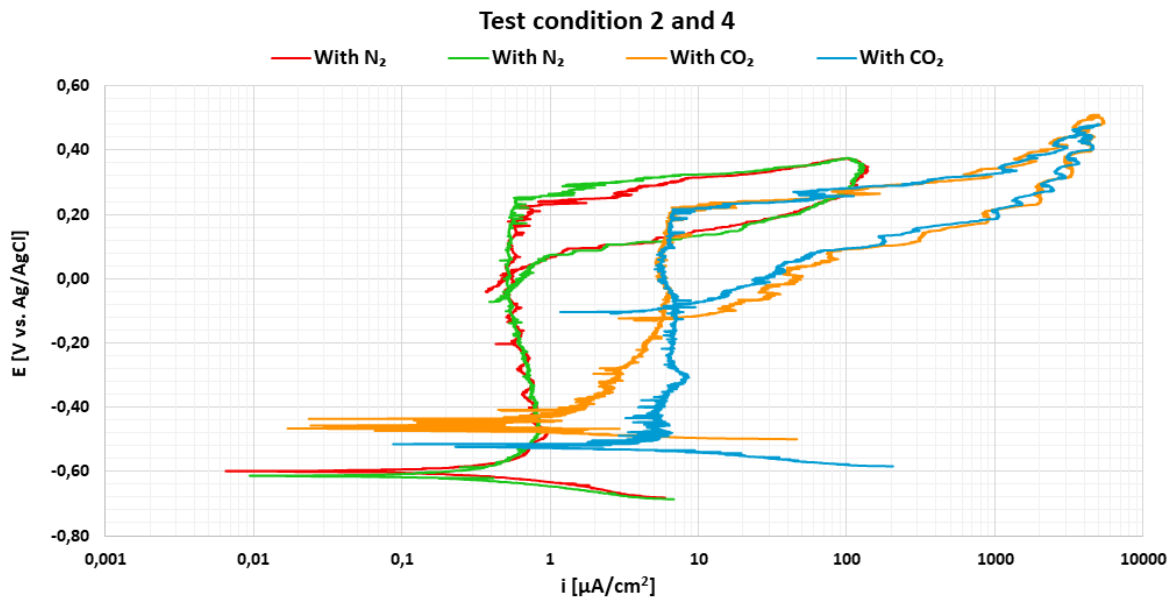


**Figure 5.19:** Anodic CPP curves for 316L obtained in solution at 95 °C with 600 ppm chloride purged with N<sub>2</sub> and CO<sub>2</sub>.

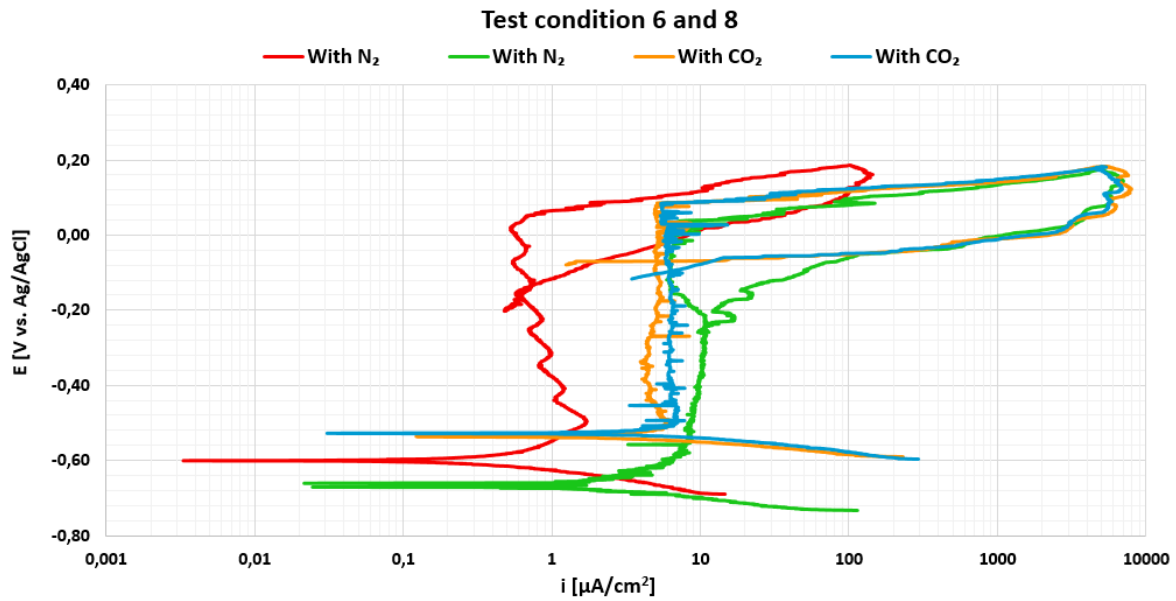


**Figure 5.20:** Anodic CPP curves for 316L obtained in solution at 95 °C with 5000 ppm chloride purged with N<sub>2</sub> and CO<sub>2</sub>.

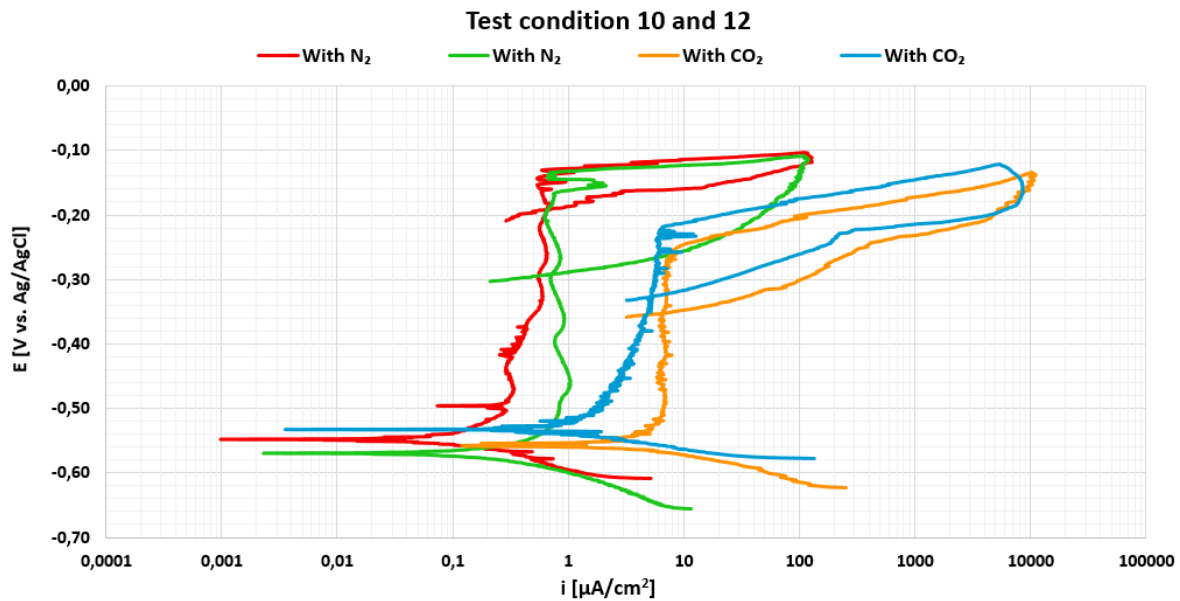


**Figure 5.21:** Anodic CPP curves for 316L obtained in electrolytes with 120 000 ppm chloride at 95 °C purged with N<sub>2</sub> and CO<sub>2</sub>.

**Table 5.18:** Parameters obtained from the CPP curves for 316L recorded in electrolytes with 600 ppm chloride at 30 °C with different pH, all potentials are vs. Ag/AgCl.

| pH      | Gas type        | OCP[V] | $E_{corr}$ [V] | $E_{crev}$ [V] | $E_{rep}$ [V] | $i_{pass}$ [ $\mu A/cm^2$ ] |
|---------|-----------------|--------|----------------|----------------|---------------|-----------------------------|
| 5.8-7.7 | N <sub>2</sub>  | -0.30  | -0.32          | 0.39           | 0.007         | 0.30                        |
| 6.7-7.0 | N <sub>2</sub>  | -0.31  | -0.36          | 0.47           | -0.044        | 0.24                        |
| 4.3-4.8 | CO <sub>2</sub> | -0.31  | -0.37          | 0.50           | 0.130         | 5.20                        |
| 4.2-5.0 | CO <sub>2</sub> | -0.31  | -0.37          | 0.52           | 0.110         | 6.12                        |

**Table 5.19:** Parameters obtained from the CPP curves for 316L recorded in electrolytes with 120 000 ppm chloride at 30 °C with different pH, all potentials are vs. Ag/AgCl.

| pH      | Gas type        | OCP[V] | $E_{corr}$ [V] | $E_{crev}$ [V] | $E_{rep}$ [V] | $i_{pass}$ [ $\mu A/cm^2$ ] |
|---------|-----------------|--------|----------------|----------------|---------------|-----------------------------|
| 5.3-5.9 | N <sub>2</sub>  | -0.35  | -0.41          | 0.069          | -0.20         | 0.14                        |
| 5.5-6.3 | N <sub>2</sub>  | -0.28  | -0.32          | 0.067          | -0.20         | 0.19                        |
| 4.8-4.9 | CO <sub>2</sub> | -0.42  | -0.48          | -0.035         | -0.04         | 1.71                        |
| 4.8-4.9 | CO <sub>2</sub> | -0.44  | -0.49          | -0.001         | -0.23         | 5.70                        |

**Table 5.20:** Parameters obtained from the CPP curves for 316L recorded in electrolytes with 600 ppm chloride at 95 °C with different pH, all potentials are vs. Ag/AgCl.

| pH      | Gas type        | OCP[V] | $E_{corr}$ [V] | $E_{crev}$ [V] | $E_{rep}$ [V] | $i_{pass}$ [ $\mu A/cm^2$ ] |
|---------|-----------------|--------|----------------|----------------|---------------|-----------------------------|
| 5.6-6.7 | N <sub>2</sub>  | -0.58  | -0.60          | 0.22           | 0.022         | 0.69                        |
| 5.9-6.7 | N <sub>2</sub>  | -0.59  | -0.61          | 0.25           | -0.033        | 0.63                        |
| 4.3-5.1 | CO <sub>2</sub> | -0.40  | -0.47          | 0.21           | -0.130        | 4.21                        |
| 4.3-5.0 | CO <sub>2</sub> | -0.48  | -0.52          | 0.21           | -0.083        | 6.25                        |

**Table 5.21:** Parameters obtained from the CPP curves for 316L recorded in electrolytes with 5000 ppm chloride at 95 °C with different pH, all potentials are vs. Ag/AgCl.

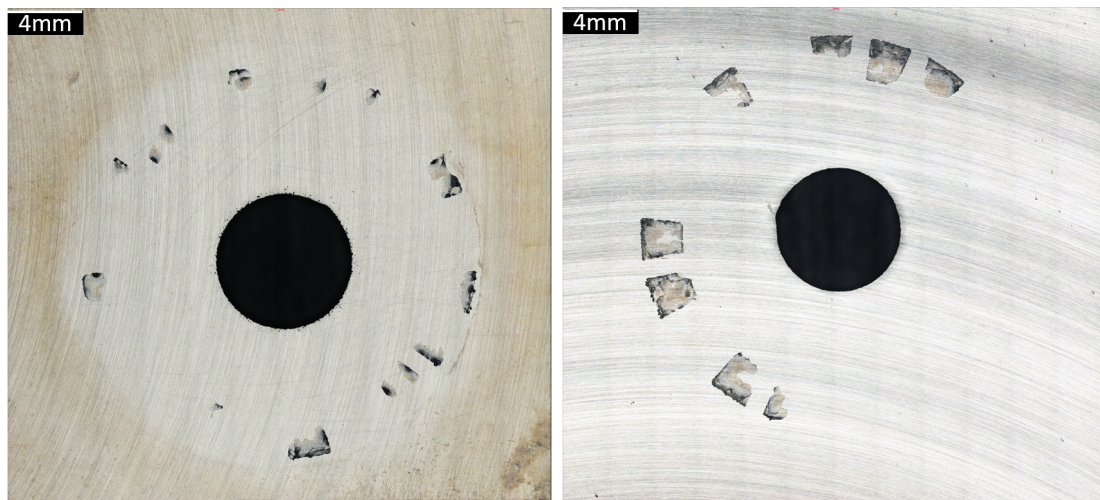
| pH      | Gas type        | OCP[V] | $E_{corr}$ [V] | $E_{crev}$ [V] | $E_{rep}$ [V] | $i_{pass}$ [ $\mu A/cm^2$ ] |
|---------|-----------------|--------|----------------|----------------|---------------|-----------------------------|
| 5.7-7.0 | N <sub>2</sub>  | -0.59  | -0.60          | 0.048          | -0.130        | 0.62                        |
| 7.2-8.0 | N <sub>2</sub>  | -0.63  | -0.66          | 0.039          | -0.240        | 9.26                        |
| 4.3-4.8 | CO <sub>2</sub> | -0.49  | -0.54          | 0.082          | -0.079        | 5.17                        |
| 4,3-4,7 | CO <sub>2</sub> | -0.50  | -0.53          | 0.085          | -0.096        | 6.35                        |



**Table 5.22:** Parameters obtained from the CPP curves for 316L recorded in electrolytes with 120 000 ppm chloride at 95 °C with different pH, all potentials are vs. Ag/AgCl.

| pH      | Gas type        | OCP[V] | $E_{corr}$ [V] | $E_{crev}$ [V] | $E_{rep}$ [V] | $i_{pass}$ [ $\mu A/cm^2$ ] |
|---------|-----------------|--------|----------------|----------------|---------------|-----------------------------|
| 5.2-6.1 | N <sub>2</sub>  | -0.56  | -0.57          | -0.14          | -0.29         | 0.88                        |
| 5.2-6.0 | N <sub>2</sub>  | -0.51  | -0.55          | -0.14          | -0.19         | 0.57                        |
| 4.9-5.0 | CO <sub>2</sub> | -0.52  | -0.56          | -0.26          | -0.35         | 7.09                        |
| 4.8-5.0 | CO <sub>2</sub> | -0.48  | -0.53          | -0.22          | -0.33         | 4.61                        |

Images of 316L samples tested in electrolytes with different pH are presented in Figure 5.22. The images were obtained with IFM with 5X magnification, and the image of the side of the sample with most severe corrosion attacks is presented.



(a) Sample tested in electrolyte purged with N<sub>2</sub>, with pH 6.7-7.0. (b) Sample tested in electrolyte purged with CO<sub>2</sub>, with pH 4.2-5.0.

**Figure 5.22:** Images of 316L samples after anodic CPP conducted in electrolytes with 600 ppm chloride at 30 °C and with different pH values, obtained with IFM with 5X magnification.

### 5.3.2 22% Cr duplex stainless steel

The curves obtained for DSS at different pH values are presented in Figure 5.23 - Figure 5.27. OCP,  $E_{corr}$ ,  $E_{crev}$ ,  $E_{rep}$  and  $i_{pass}$  values obtained from the curves are presented in Table 5.23 - Table 5.27.

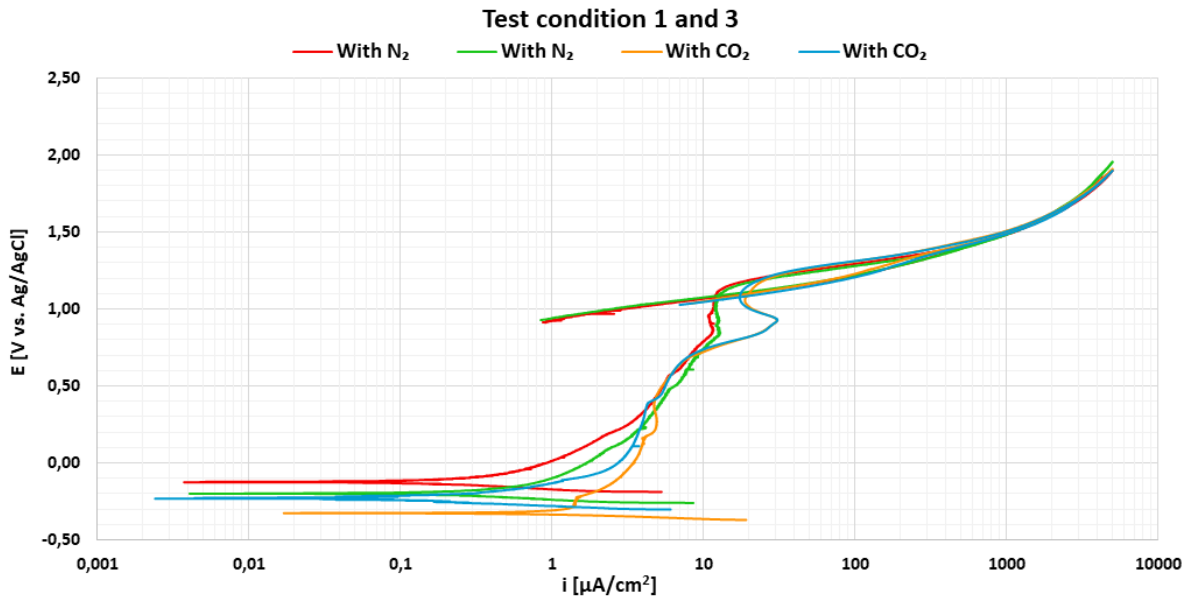


**Figure 5.23:** Anodic CPP curves for DSS obtained in electrolytes with 600 ppm chloride at 30 °C purged with N<sub>2</sub> and CO<sub>2</sub>.

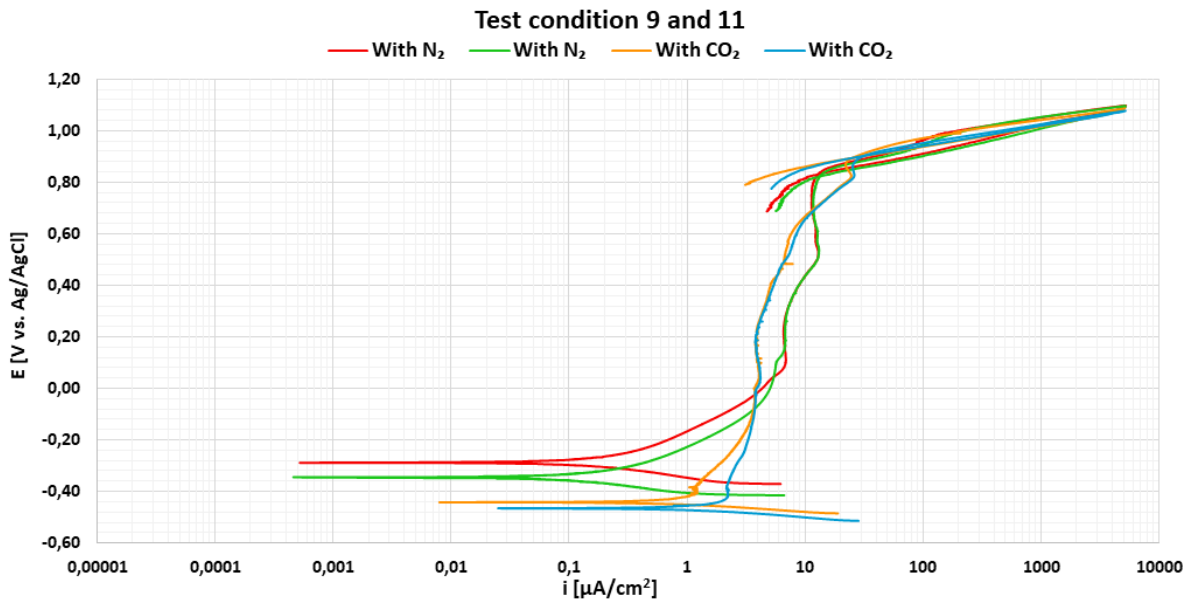


**Figure 5.24:** Anodic CPP curves for DSS obtained in electrolytes with 120 000 ppm chloride at 30 °C purged with N<sub>2</sub> and CO<sub>2</sub>.

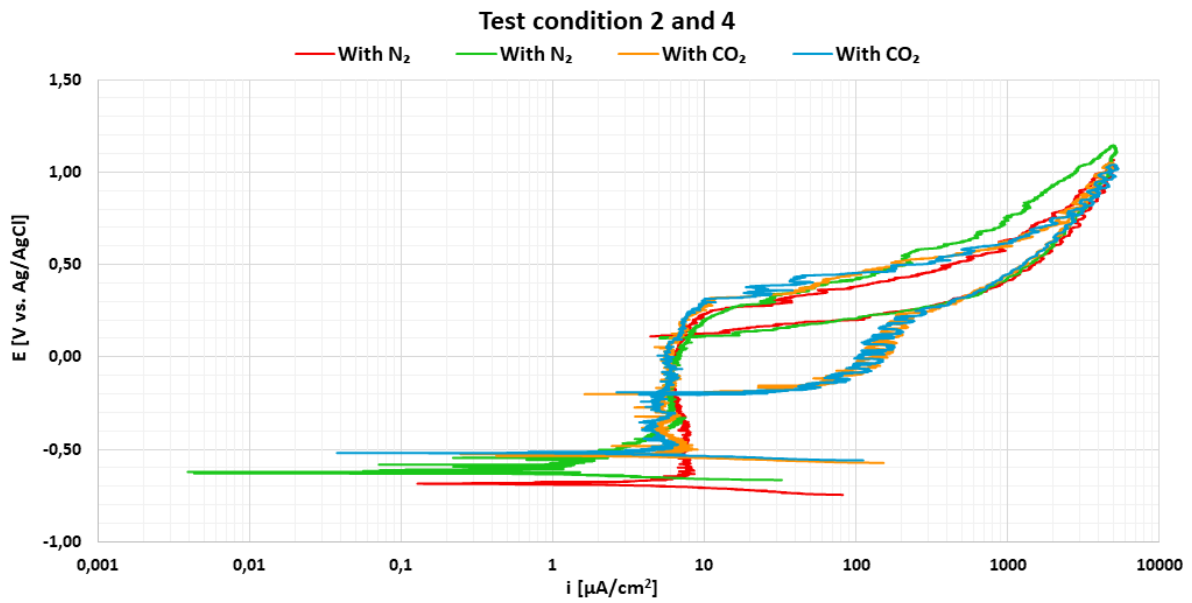


**Figure 5.25:** Anodic CPP curves for DSS obtained in electrolytes with 600 ppm chloride at 95 °C purged with N<sub>2</sub> and CO<sub>2</sub>.

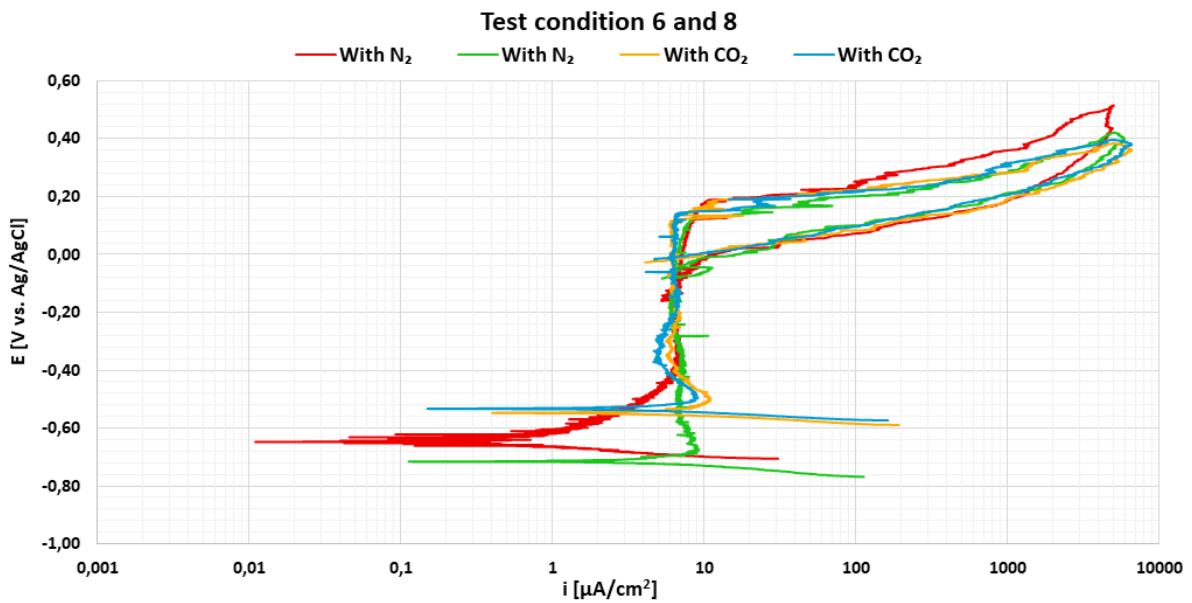


**Figure 5.26:** Anodic CPP curves for DSS obtained in electrolytes with 5000 ppm chloride at 95 °C with purged with N<sub>2</sub> and CO<sub>2</sub>.

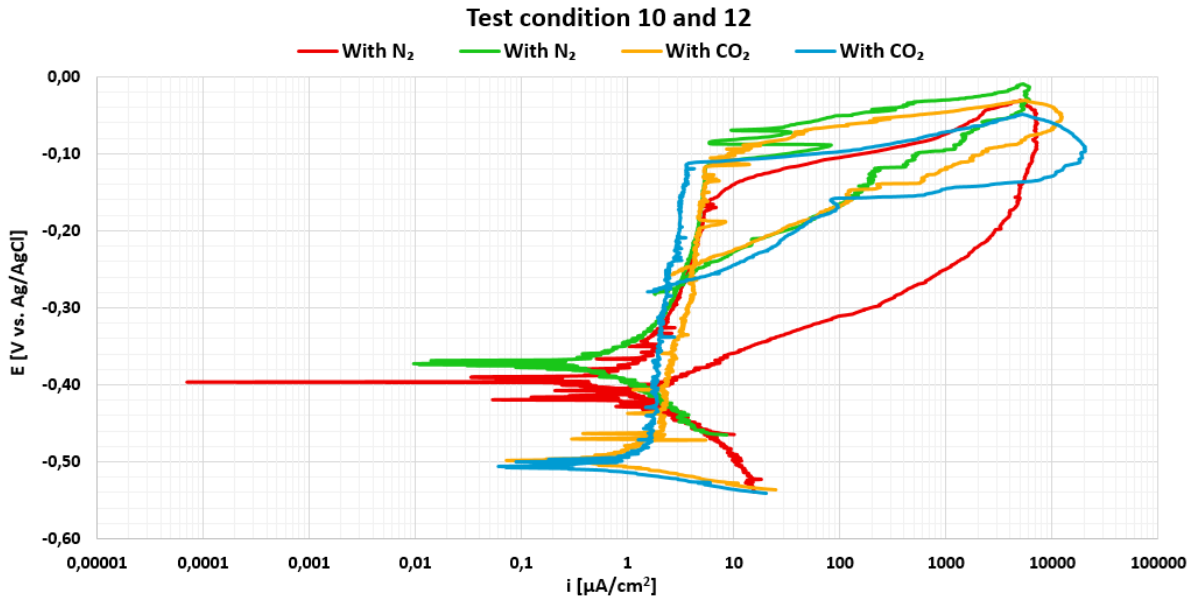


**Figure 5.27:** Anodic CPP curves for DSS obtained in electrolytes with 120 000 ppm chloride at 95 °C purged with N<sub>2</sub> and CO<sub>2</sub>.

**Table 5.23:** Parameters obtained from the CPP curves for DSS recorded in electrolytes with 600 ppm chloride at 30 °C with different pH, all potentials are vs. Ag/AgCl.

| pH      | Gas type        | OCP[V] | $E_{corr}$ [V] | $E_{crev}$ [V] | $E_{rep}$ [V] | $i_{pass}$ [ $\mu A/cm^2$ ] |
|---------|-----------------|--------|----------------|----------------|---------------|-----------------------------|
| 6.8-7.5 | N <sub>2</sub>  | -0.087 | -0.12          | 1.17           | 1.08          | 5.20                        |
| 6.5-7.4 | N <sub>2</sub>  | -0.16  | -0.20          | 1.17           | 1.09          | 5.31                        |
| 4.1-4.2 | CO <sub>2</sub> | -0.27  | -0.33          | 1.20           | 1.10          | 5.65                        |
| 4.2-4.5 | CO <sub>2</sub> | -0.20  | -0.23          | 1.20           | 1.08          | 5.61                        |

**Table 5.24:** Parameters obtained from the CPP curves for DSS recorded in electrolytes with 120 000 ppm chloride at 30 °C with different pH, all potentials are vs. Ag/AgCl.

| pH      | Gas type        | OCP[V] | $E_{corr}$ [V] | $E_{crev}$ [V] | $E_{rep}$ [V] | $i_{pass}$ [ $\mu A/cm^2$ ] |
|---------|-----------------|--------|----------------|----------------|---------------|-----------------------------|
| 7.2-8.5 | N <sub>2</sub>  | -0.27  | -0.29          | 0.84           | 0.83          | 8.42                        |
| 7.2-8.5 | N <sub>2</sub>  | -0.31  | -0.34          | 0.84           | 0.82          | 8.39                        |
| 4.8     | CO <sub>2</sub> | -0.39  | -0.44          | 0.90           | 0.89          | 5.19                        |
| 4.8     | CO <sub>2</sub> | -0.41  | -0.47          | 0.91           | 0.90          | 5.30                        |

**Table 5.25:** Parameters obtained from the CPP curves for DSS recorded in electrolytes with 600 ppm chloride at 95 °C and different pH-values, all potentials are vs. Ag/AgCl.

| pH      | Gas type        | OCP[V] | $E_{corr}$ [V] | $E_{crev}$ [V] | $E_{rep}$ [V] | $i_{pass}$ [ $\mu A/cm^2$ ] |
|---------|-----------------|--------|----------------|----------------|---------------|-----------------------------|
| 7.1-8.5 | N <sub>2</sub>  | -0.65  | -0.69          | 0.25           | 0.12          | 7.04                        |
| 7.1-8.3 | N <sub>2</sub>  | -0.57  | -0.63          | 0.26           | 0.11          | 6.67                        |
| 4.3-5.5 | CO <sub>2</sub> | -0.47  | -0.52          | 0.31           | 0.11          | 5.90                        |
| 4.3-5.3 | CO <sub>2</sub> | -0.46  | -0.52          | 0.31           | 0.11          | 6.04                        |

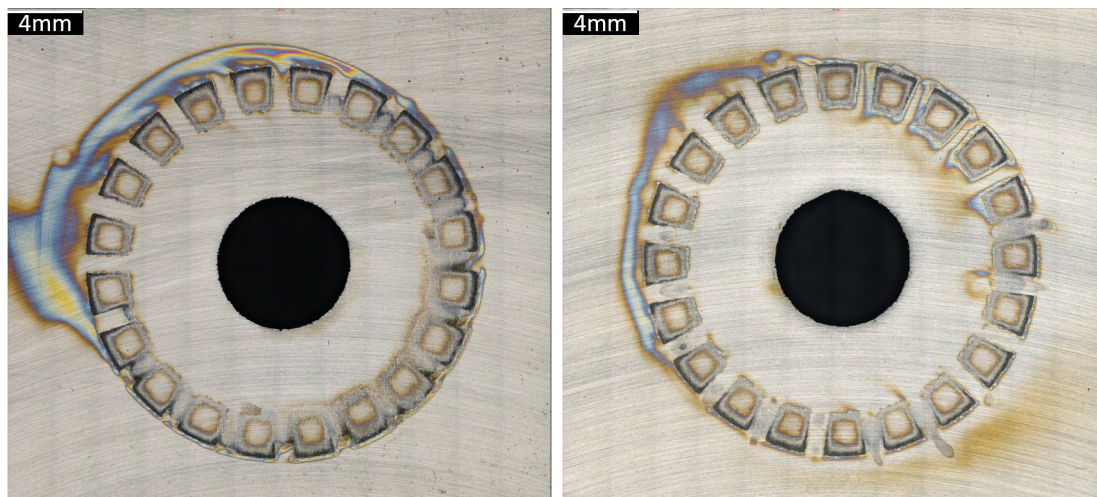
**Table 5.26:** Parameters obtained from the CPP curves for DSS recorded in electrolytes with 5000 ppm chloride at 95 °C and different pH-values, all potentials are vs. Ag/AgCl.

| pH      | Gas type        | OCP[V] | $E_{corr}$ [V] | $E_{crev}$ [V] | $E_{rep}$ [V] | $i_{pass}$ [ $\mu A/cm^2$ ] |
|---------|-----------------|--------|----------------|----------------|---------------|-----------------------------|
| 7.2-8.2 | N <sub>2</sub>  | -0.61  | -0.65          | 0.18           | -0.100        | 6.79                        |
| 7.4-8.0 | N <sub>2</sub>  | -0.67  | -0.72          | 0.13           | -0.077        | 6.33                        |
| 4.3-4.8 | CO <sub>2</sub> | -0.49  | -0.55          | 0.12           | -0.018        | 6.50                        |
| 4.3-4.8 | CO <sub>2</sub> | -0.47  | -0.53          | 0.13           | -0.010        | 6.60                        |

**Table 5.27:** Parameters obtained from the CPP curves for DSS recorded in electrolytes with 120 000 ppm chloride at 95 °C and different pH-values, all potentials are vs. Ag/AgCl.

| pH      | Gas type        | OCP[V] | $E_{corr}$ [V] | $E_{crev}$ [V] | $E_{rep}$ [V] | $i_{pass}$ [ $\mu A/cm^2$ ] |
|---------|-----------------|--------|----------------|----------------|---------------|-----------------------------|
| 7.6-7.7 | N <sub>2</sub>  | -0.36  | -0.40          | -0.16          | -0.36         | 3.42                        |
| 7.5-7.6 | N <sub>2</sub>  | -0.37  | -0.37          | -0.12          | -0.27         | 3.66                        |
| 4.9-5.0 | CO <sub>2</sub> | -0.44  | -0.50          | -0.11          | -0.24         | 4.04                        |
| 4.9-5.0 | CO <sub>2</sub> | -0.44  | -0.51          | -0.11          | -0.27         | 2.64                        |

Images of DSS samples tested in electrolytes with different pH are presented in Figure 5.28. The images were obtained with IFM with 5X magnification, and the image of the side of the sample with most severe corrosion attacks are presented.



(a) Sample tested in electrolyte purged with  $N_2$ , with pH 6.8-7.5. (b) Sample tested in electrolyte purged with  $CO_2$ , with pH 4.1-4.2.

**Figure 5.28:** Images of DSS samples after anodic CPP conducted in electrolytes with 600 ppm chloride at 30 °C and with different pH values, obtained with IFM with 5X magnification.

## 5.4 Surface characterization

After anodic CPP, the sample surfaces were investigated and weight loss of each sample was calculated. The results will be presented in this section, and the results for 316L and DSS will be presented separately. Surface characterization of the samples includes overview images, used to investigate the extent and to compare the crevice corrosion attacks at each test condition according to the test program in Table 4.4. IFM was used to obtain overview images of the samples, and a selection of these was presented in Section 5.1 - Section 5.3. One 316L and one DSS sample from each parallel were chosen, since the samples within each parallel showed similar surface changes, with exception of the 316L samples tested at test condition 11. As mentioned in Section 5.2.1, these samples experienced different courses of repassivation. This resulted in different surface changes, that will be discussed further in Section 6.1.1. The average crevice percentage for the two samples was therefore used for this test condition. The crevice percentage was obtained by analyzing the IFM overview images in ImageJ [81]. It must be emphasized that it is not the percentage of crevices on the entire surface that has been obtained, but the percentage within a selected area. The selected area included all observed crevices and was the same size for each sample analyzed, to enable comparison of the obtained results. No tests were conducted at test condition 5 for DSS or at test condition 7 for either of the materials. For selected samples, more detailed images of crevices were taken to investigate the severity and depth of the attacks. For this purpose, a selection of samples tested at different conditions were chosen.

### 5.4.1 AISI 316L stainless steel

Overview images of both sides of one 316L sample from each parallel were obtained with IFM, with 5X magnification. The images were analyzed in ImageJ, and the percentage



of crevices on the surface within a selected area was obtained. The results for all the test conditions are presented in Table 5.28.

**Table 5.28:** Percentage crevices on the 316L sample surfaces, at each test condition.

| Test condition | Crevice [%] |
|----------------|-------------|
| 1              | 0.75        |
| 2              | 0.06        |
| 3              | 1.00        |
| 4              | 0.07        |
| 5              | 0.08        |
| 6              | 0.42        |
| 8              | 0.06        |
| 9              | 1.36        |
| 10             | 0.05        |
| 11             | 0.49        |
| 12             | 0.18        |

When analyzing the samples in ImageJ, the darker areas on the sample surface were changed to blue and the brighter areas to green. This is illustrated in Figure 5.29, which shows both sides of a 316L sample tested at test condition 3 after being analyzed in ImageJ. The crevice percentage in the selected area was obtained by subtracting the percentage corresponding to the area of the crevice assembly hole from the percentage of the surface that was blue.

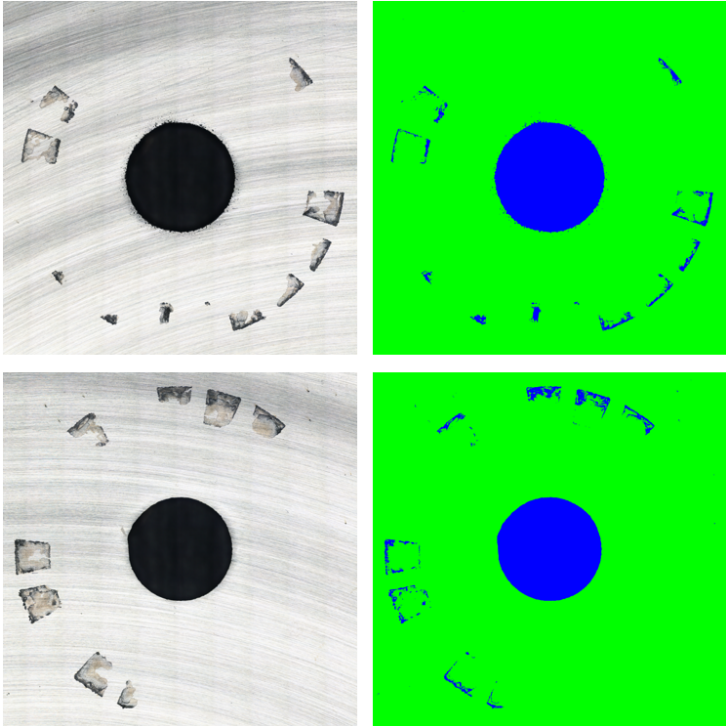
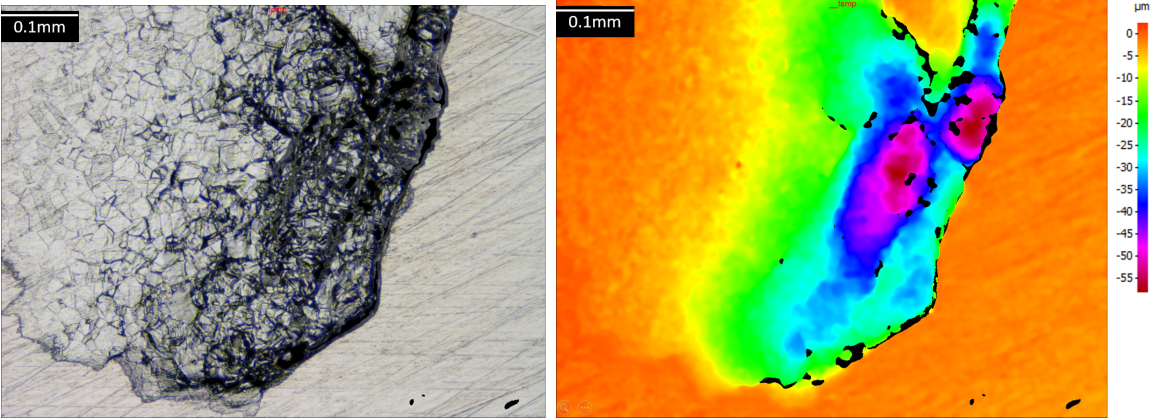


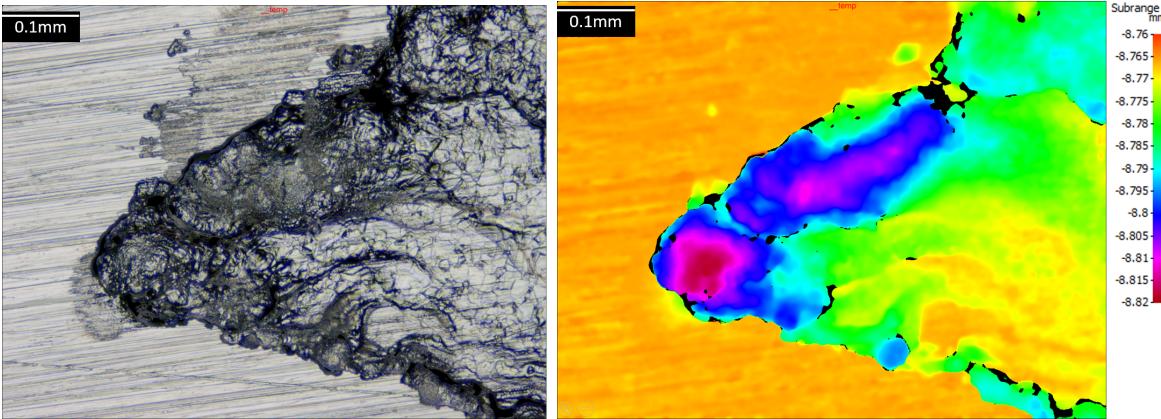
**Figure 5.29:** Images of the surface of a 316L sample (both sides) tested in electrolyte with 600 ppm chloride and pH 4.2-5.0 at 30 °C, obtained with IFM and analyzed in ImageJ.

More detailed images of selected 316L samples were obtained with 20X magnification and 500 nm resolution with IFM, and are presented in Figure 5.30 - Figure 5.32. The black spots are areas the light source from the optical microscope were not able to reach.



(a) IFM image showing one of the observed crevices. (b) IFM image of the crevice with a scale bar presenting the depth distribution [ $\mu\text{m}$ ].

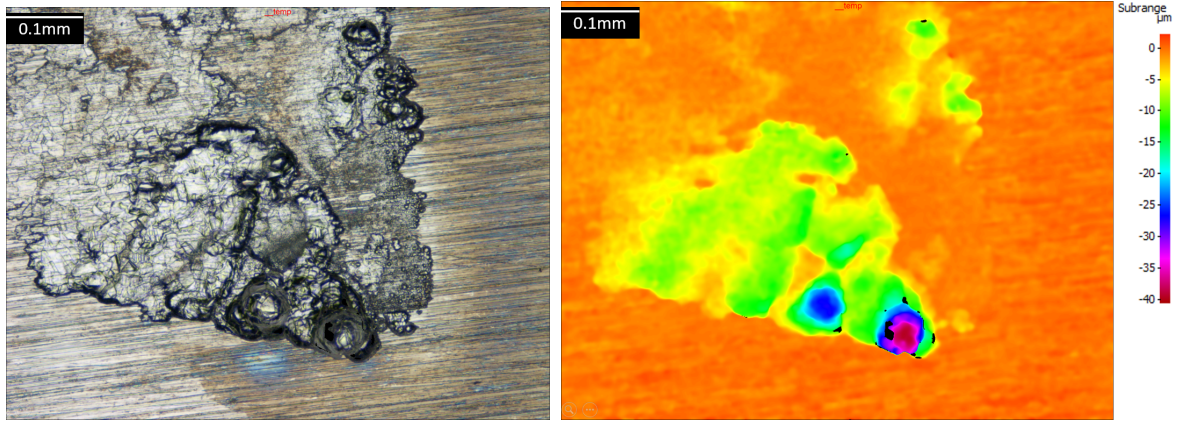
**Figure 5.30:** Crevice observed on a 316L sample after anodic CPP in 600 ppm chloride and pH 5.8-7.7 at 30 °C, imaged by IFM.



(a) IFM image showing one of the observed crevices. (b) IFM image of the crevice with a scale bar presenting the depth distribution [mm].

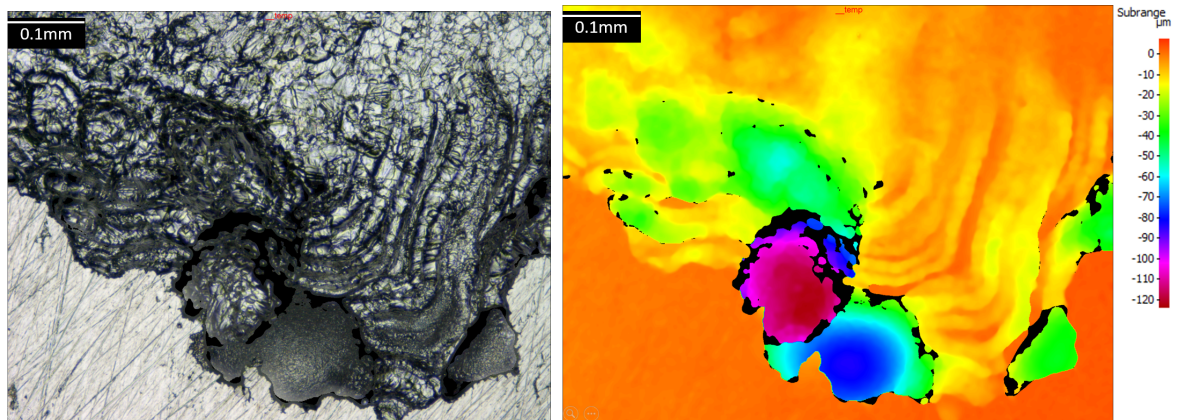
**Figure 5.31:** Crevice observed on a 316L sample after anodic CPP in 600 ppm chloride and pH 4.2-5.0 at 30 °C, imaged by IFM.





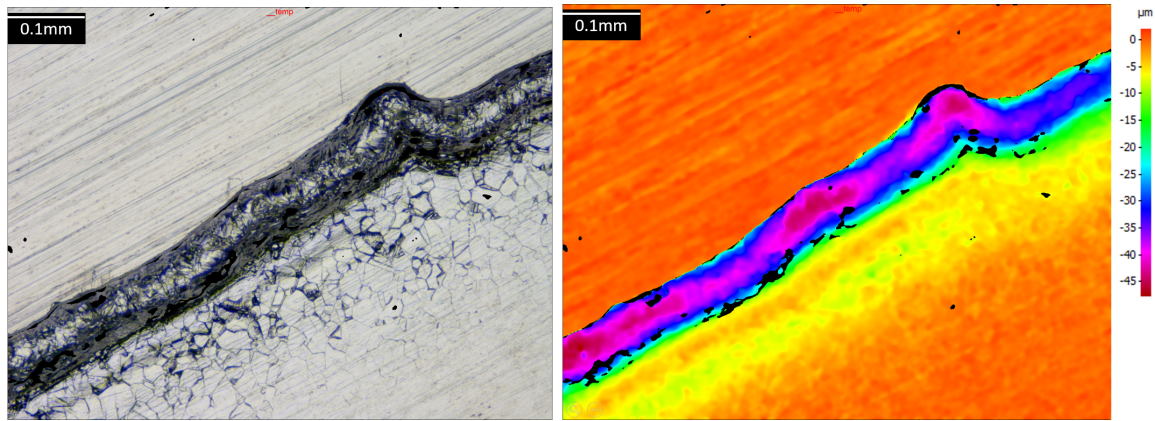
(a) IFM image showing one of the observed crevices. (b) IFM image of the crevice with a scale bar presenting the depth distribution [ $\mu\text{m}$ ].

**Figure 5.32:** Crevice observed on a 316L sample after anodic CPP in 600 ppm chloride and pH 4.3-5.0 at 95 °C, imaged by IFM.



(a) IFM image showing one of the observed crevices. (b) IFM image of the crevice with a scale bar presenting the depth distribution [ $\mu\text{m}$ ].

**Figure 5.33:** Crevice observed on a 316L sample after anodic CPP in 5000 ppm chloride and pH 5.6 at 30 °C, imaged by IFM.



(a) IFM image showing one of the observed crevices. (b) IFM image of the crevice with a scale bar presenting the depth distribution [ $\mu\text{m}$ ].

**Figure 5.34:** Crevice observed on a 316L sample after anodic CPP in 120 000 ppm chloride and pH 5.3-5.9 at 30 °C, imaged by IFM.

The crevice imaged in Figure 5.30 had a depth of 57.92  $\mu\text{m}$ , the crevice in Figure 5.31 was 52.08  $\mu\text{m}$  deep, the crevice in Figure 5.32 was 39.77  $\mu\text{m}$  deep, the crevice in Figure 5.33 was 123.96  $\mu\text{m}$  deep and the crevice in Figure 5.34 was 41.37  $\mu\text{m}$  deep,

All samples were weighed before and after the anodic CPP. Average weight loss for the two 316L samples tested at each conditions, is presented in Table 5.29.

**Table 5.29:** Average weight loss for 316L samples after the anodic CPP measurements at the different tests conditions.

| Test condition | Weight loss [g] |
|----------------|-----------------|
| 1              | 0.0026          |
| 2              | 0.0009          |
| 3              | 0.0202          |
| 4              | 0.0068          |
| 5              | 0.0021          |
| 6              | 0.0027          |
| 8              | 0.0061          |
| 9              | 0.0159          |
| 10             | 0.0003          |
| 11             | 0.0081          |
| 12             | 0.0040          |

#### 5.4.2 22% Cr duplex stainless steel

Obtained crevice percentage on the DSS samples, after analyzing the overview images in ImageJ is presented in Table 5.30. Figure 5.35 presents both sides of a DSS sample tested at test condition 3 before and after ImageJ analysis.

**Table 5.30:** Percentage crevices on the DSS sample surfaces, at each test condition.

| Test condition | Crevice [%] |
|----------------|-------------|
| 1              | 2.12        |
| 2              | 0.57        |
| 3              | 1.55        |
| 4              | 1.47        |
| 6              | 0.96        |
| 8              | 0.64        |
| 9              | 0.04        |
| 10             | 0.10        |
| 11             | 0.17        |
| 12             | 0.40        |

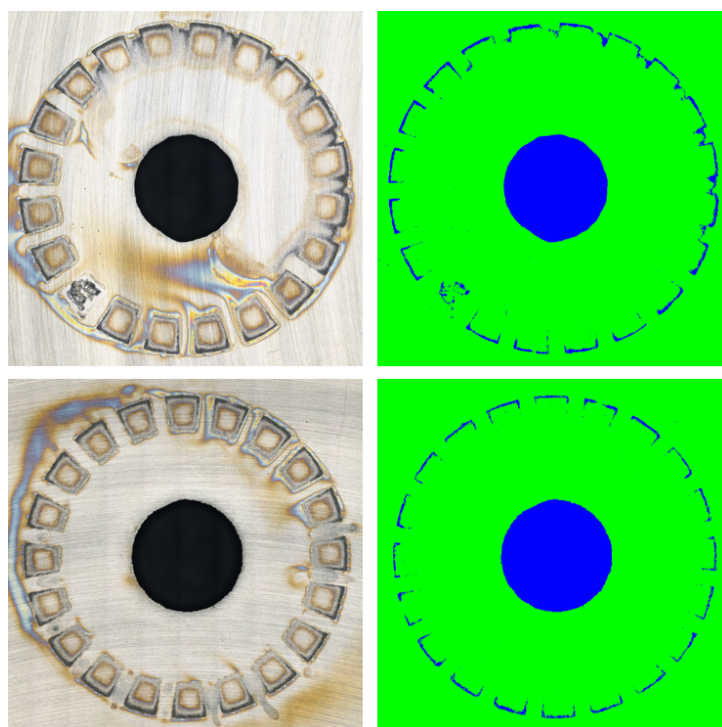
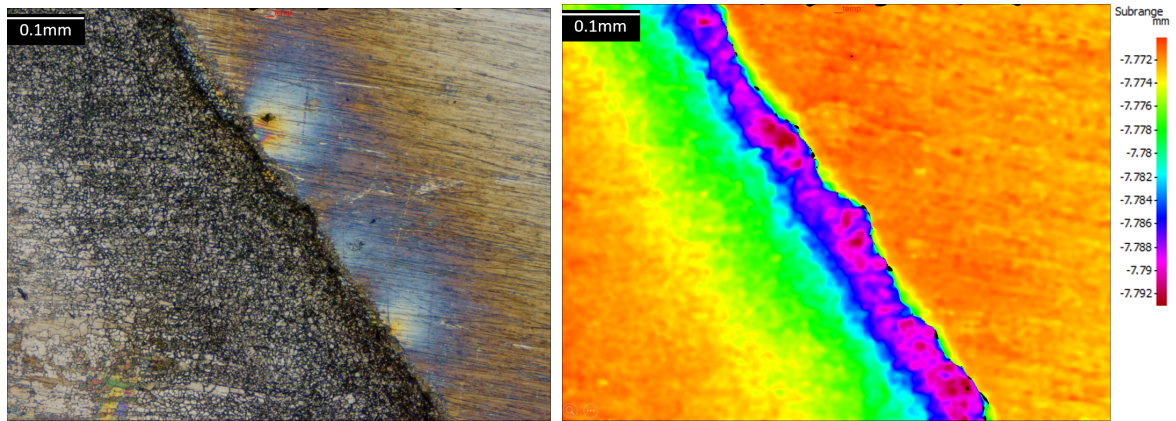


**Figure 5.35:** Images of the surface of a DSS sample (both sides) tested in electrolyte with 600 ppm chloride and pH 4.1-4.2 at 30 °C, obtained with IFM and analyzed in ImageJ.

To illustrate the procedure used to obtain the crevice percentage, additional images of samples of both materials tested at test condition 6 and 12 are included in Appendix A.3. The results in Table 5.28 and Table 5.30 were considered to provide sufficient information regarding the severity of the crevice attacks, and the other overview images analyzed in ImageJ were not included in the thesis.

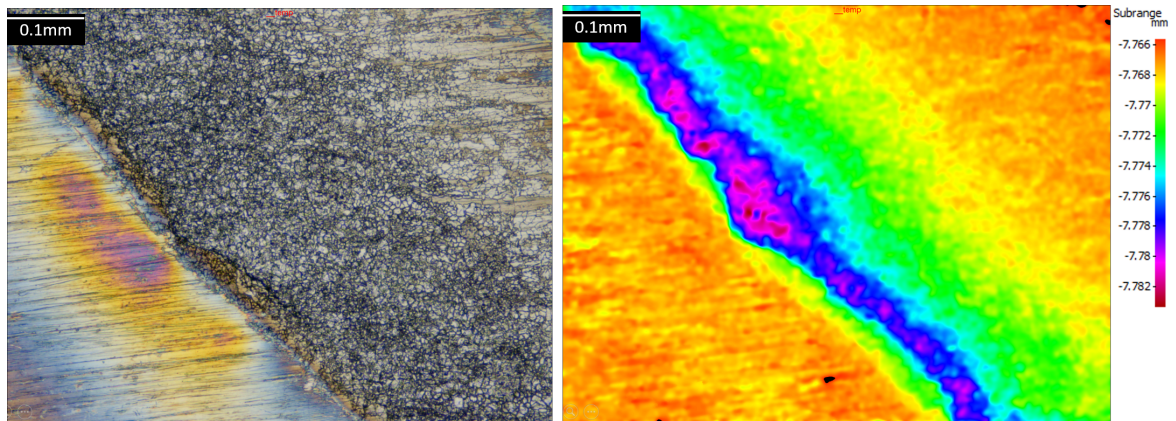
As for the 316L samples, more detailed images of selected DSS samples were obtained with IFM, with 20X magnification and 500 nm resolution. The images are presented in Figure 5.36 - Figure 5.39.





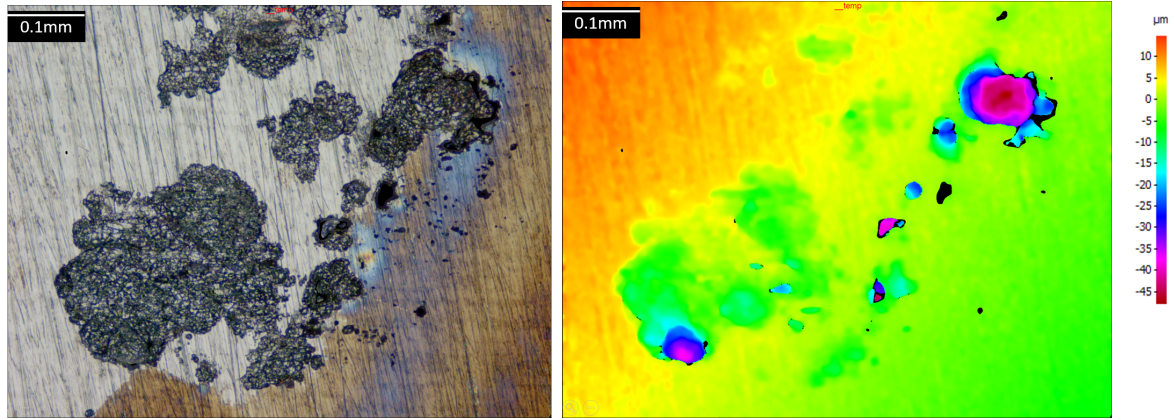
(a) IFM image showing one of the observed crevices. (b) IFM image of the crevice with a scale bar presenting the depth distribution [mm].

**Figure 5.36:** Crevice observed on a DSS sample after anodic CPP in 600 ppm chloride and pH 6.8-7.5 at 30 °C, imaged by IFM.



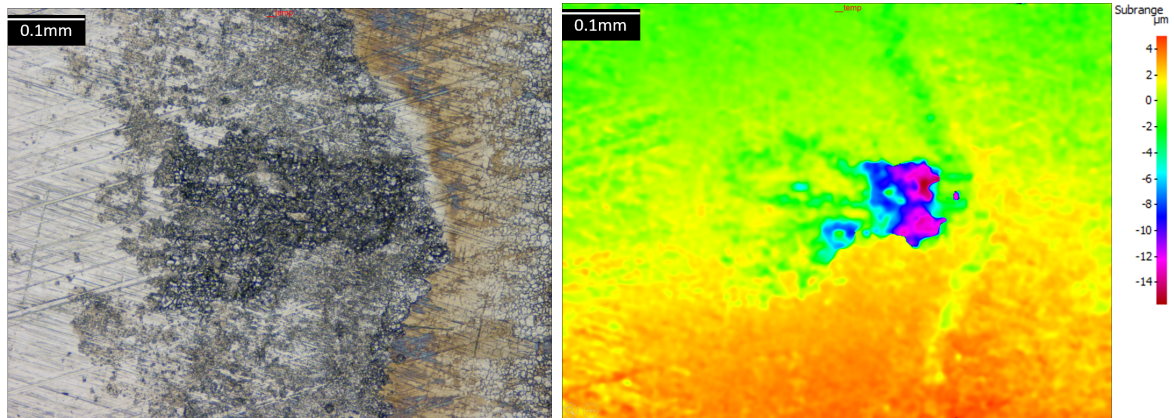
(a) IFM image showing one of the observed crevices. (b) IFM image of the crevice with a scale bar presenting the depth distribution [mm].

**Figure 5.37:** Crevice observed on a DSS sample after anodic CPP in 600 ppm chloride and pH 4.1-4.2 at 30 °C, imaged by IFM.



(a) IFM image showing one of the observed crevices. (b) IFM image of the crevice with a scale bar presenting the depth distribution [ $\mu\text{m}$ ].

**Figure 5.38:** Crevice observed on a DSS sample after anodic CPP in 600 ppm chloride and pH 7.1-8.5 at 95 °C, imaged by IFM.



(a) IFM image showing one of the observed crevices. (b) IFM image of the crevice with a scale bar presenting the depth distribution [ $\mu\text{m}$ ].

**Figure 5.39:** Crevice observed on a DSS sample after anodic CPP in 120 000 ppm chloride and pH 7.2-8.5 at 30 °C, imaged by IFM.

The crevice imaged in Figure 5.36 had a depth of 21.66  $\mu\text{m}$ , the crevice in Figure 5.37 was 14.77  $\mu\text{m}$  deep, the crevice in Figure 5.38 was 50.02  $\mu\text{m}$  deep and the crevice in Figure 5.39 was 18.76  $\mu\text{m}$  deep.

Average weight loss for the two DSS samples tested at each conditions, is presented in Table 5.31.

**Table 5.31:** Average weight loss for DSS samples after the anodic CPP measurements at the different tests conditions.

| Test condition | Weight loss [g] |
|----------------|-----------------|
| 1              | 0.0021          |
| 2              | 0.0173          |
| 3              | 0.0018          |
| 4              | 0.0124          |
| 6              | 0.0074          |
| 8              | 0.0061          |
| 9              | 0.0011          |
| 10             | 0.0013          |
| 11             | 0.0013          |
| 12             | 0.0053          |

## 5.5 OCP measurements

OCP measurements were conducted to investigate the corrosion susceptibility of the materials in the presence of oxygen, and to compare the OCP with obtained  $E_{crev}$  and  $E_{rep}$  from the anodic CPP curves at equivalent temperature, chloride concentration and similar pH for both test materials. The OCP measurements were conducted with both test materials simultaneously, exposed to the conditions presented in Table 4.5 for 48 hours, with the exception of the test saturated with oxygen. During this test the samples were exposed for 144 hours, as the temperature was changed without starting a new test with new samples. The pH during this test changed from 7.3-7.6 at 95 °C, to 7.8-7.9 at 60 °C and finally to 8.0-8.1 at 30 °C. The OCP measurements are presented in Figure 5.40 - Figure 5.45.

The increase in potential, started approximately after 34 hours of exposure, observed in Figure 5.43, is believed to be caused by oxygen ingress. As a result of NaCl crystallizing inside the gas inlet tube, N<sub>2</sub> gas were unable to get through the tube and into the electrolyte.

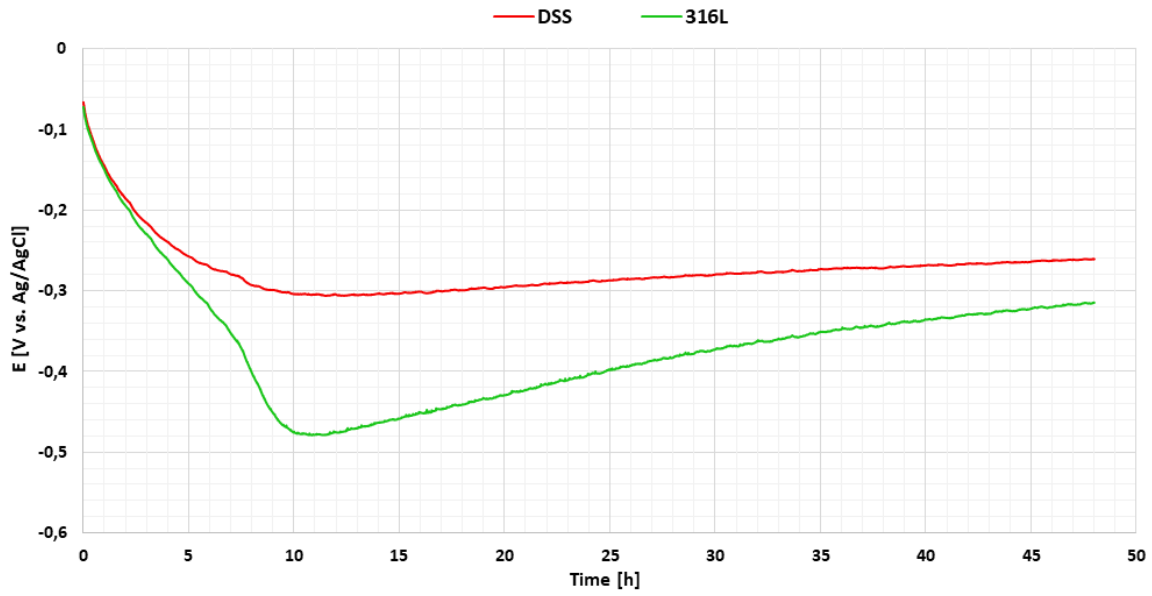


**Figure 5.40:** OCP development as a function of time for samples in an electrolyte without oxygen, with 600 ppm chloride and pH 7.0-7.4 at 30 °C.

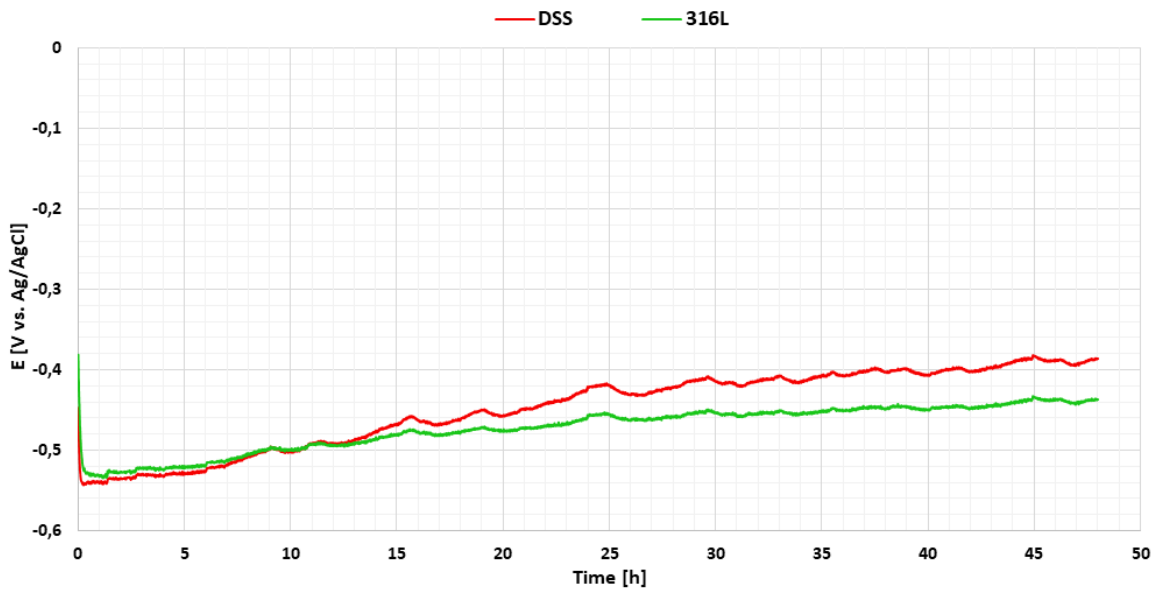


**Figure 5.41:** OCP development as a function of time for samples in an electrolyte without oxygen, with 600 ppm chloride and pH 7.2-8.0 at 95 °C.

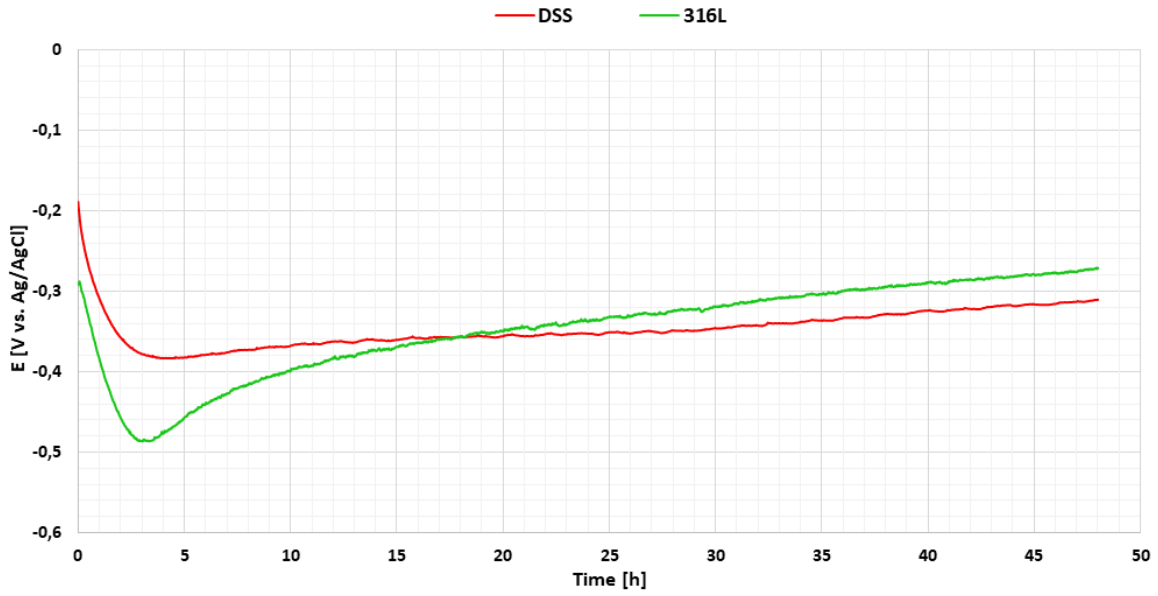


**Figure 5.42:** OCP development as a function of time for samples in an electrolyte without oxygen, with 19 000 ppm chloride and pH 7.1-7.8 at 45 °C.

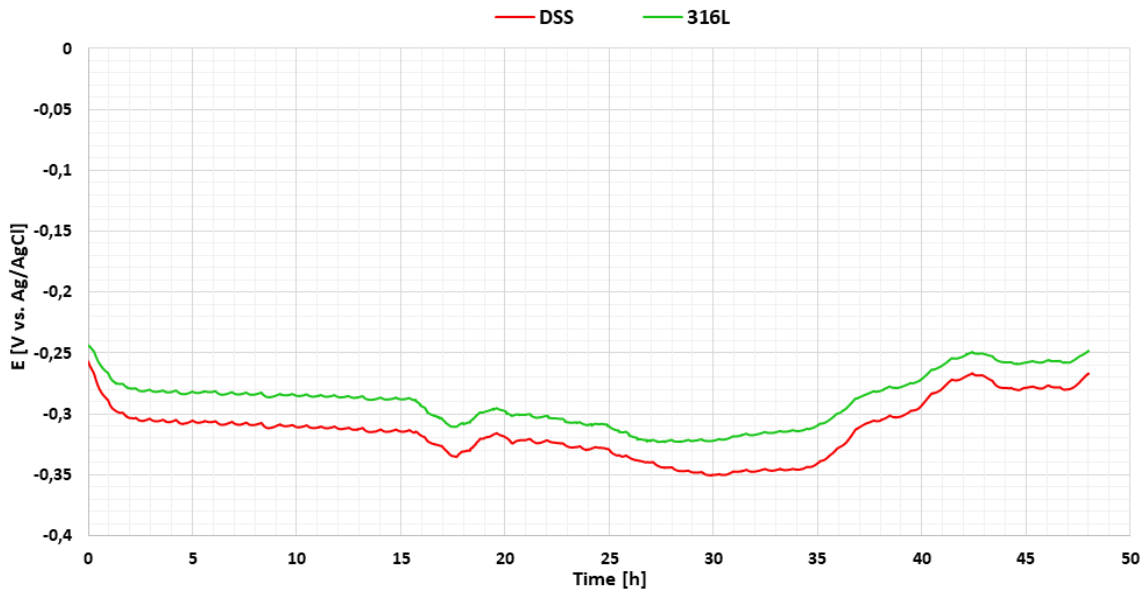


**Figure 5.43:** OCP development as a function of time for samples in an electrolyte without oxygen, with 120 000 ppm chloride and pH 8.6-8.7 at 30 °C.



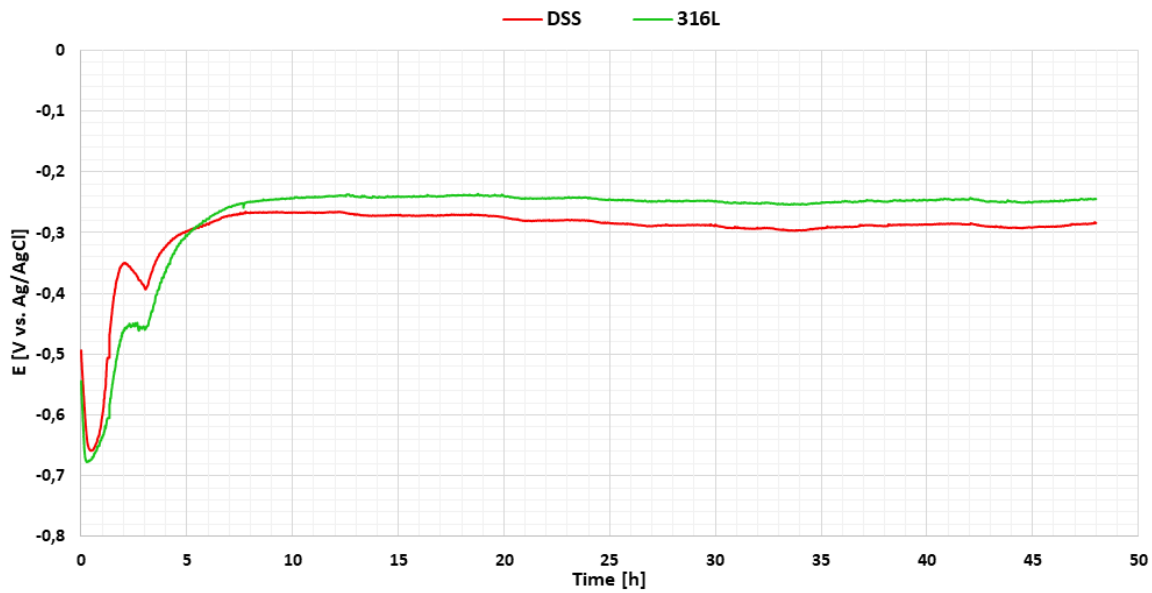


**Figure 5.44:** OCP development as a function of time for samples in an electrolyte without oxygen, with 120 000 ppm chloride and pH 6.5-7.0 at 95 °C.

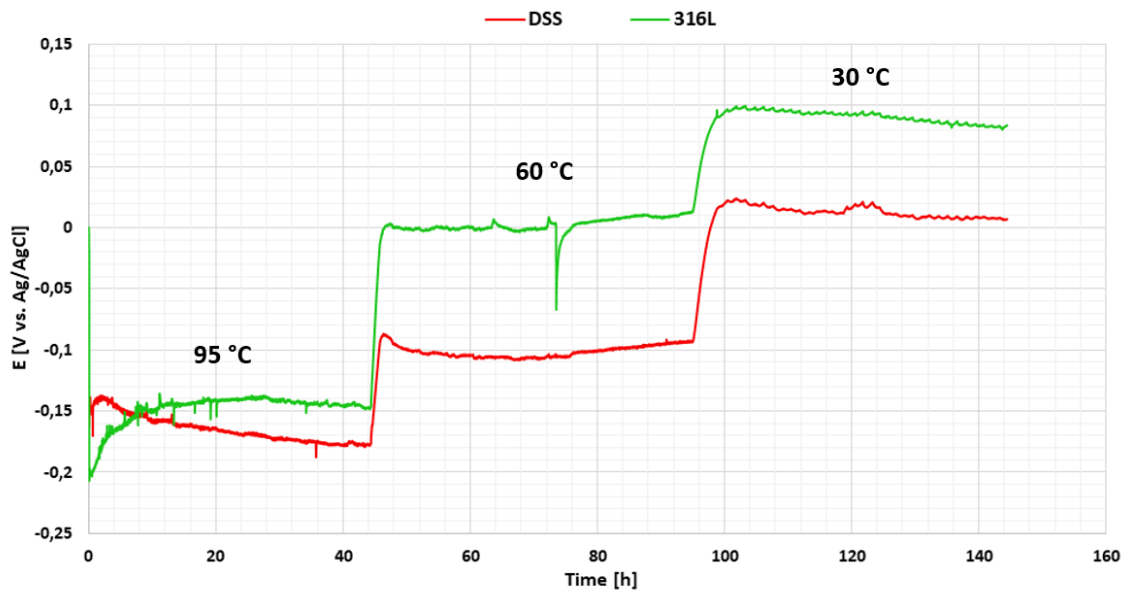


**Figure 5.45:** OCP development as a function of time for samples in an electrolyte saturated with oxygen, with 120 000 ppm chloride and pH 7.3-8.1 at 30 °C, 60 °C and 95 °C.

No corrosion attacks were observed on either of the samples and no weight loss was measured after the OCP measurements.



## 6 Discussion

The results obtained from the experimental work will be further discussed in the following sections. The effect of temperature, chloride concentrations and pH on the corrosion properties of the two materials will be discussed separately. DOE will be used to analyse the effect of the different parameters. Additionally, the extent of the crevice corrosion attack based on the surface characterisation for each sample will be discussed and a comparison of the materials will be conducted. Finally, the results from the OCP measurement will be discussed. As only tests without oxygen and saturated with oxygen were conducted, unpublished results established by Equinor, presented in Section 3.3, will be discussed to assess the effect of oxygen.

### 6.1 Effect of temperature

#### 6.1.1 AISI 316L stainless steel

Potentials obtained from the anodic CPP curves are presented in Table 5.1 - Table 5.5, and showed that OCP and  $E_{corr}$  decreased with increasing temperature. This result applies regardless of pH or chloride concentration of the electrolyte.

As observed from the values in Table 5.1 - Table 5.5,  $E_{crev}$  decreased when the temperature was increased. This applied to all chloride concentration and pH-regions tested. Since crevice corrosion can be initiated at a lower potential when the temperature is high, this results indicate that 316L is less resistant towards crevice corrosion at higher temperatures. As stated in Section 2.4.1, increased temperature accelerates the transition from metastable to stable corrosion. According to Matsch and Böhni [31], this is the main reason for the decreasing potential experienced when the temperature is increased. Nevertheless, overview images of the samples presented in Figure 5.3 indicate that the sample exposed to a lower temperature experienced more severe crevice corrosion attacks. The anodic CPP curves that represent these samples are presented in Figure 5.2, where the green curve represents the sample tested at 30 °C and the blue curve the sample tested at 95 °C. As can be observed from the curves, the difference between  $E_{crev}$  and  $E_{rep}$  was bigger for the green curve than for the blue curve. This indicates that the crevices on the sample tested at 30 °C had more time to grow before the surface repassivated. However, the results regarding the extent of the corrosion attacks on samples tested at 30 °C are not consequent. The red curve in Figure 5.2, also obtained at 30 °C had a higher  $E_{rep}$  and a smaller difference between  $E_{crev}$  and  $E_{rep}$ . Corrosion attacks on this sample were barely visible due to the limited exposure period between  $E_{crev}$  and  $E_{rep}$ .

The repassivation potentials presented in Table 5.1 - Table 5.3 were discussed in the project thesis [1], and the report concluded that  $E_{rep}$  was not affected by change in temperature when the chloride concentration was 600 ppm. Low chloride ion availability could inhibit the crevice initiation, as the chloride ion availability is the rate determining process when the chloride concentration is sufficient low [82]. At higher chloride concentrations, 5000 ppm and 120 000 ppm, the results within each parallel deviated. Since most of the tests experienced a decrease in  $E_{rep}$  with increasing temperature, it seemed to be harder for the surface to repassivate at higher temperatures.

The repassivation potentials presented in Table 5.4 - Table 5.5, obtained from curves

recorded during this thesis, decreased with increasing temperature. This was the case for both low and high chloride concentrations, 600 ppm and 120 000 ppm, respectively. This indicates that repassivation of the surface becomes more difficult at higher temperatures. Increased temperature promotes corrosion tendency [31] and reduces the protective properties of the passive film [33], as stated in Section 2.4.1. A damaged passive film makes it harder for the surface to repassivate.

### 6.1.2 22% Cr duplex stainless steel

As presented in Table 5.6 - Table 5.9, OCP and  $E_{corr}$  decreased with increasing temperature. This is the case for all chloride concentrations and pH-regions tested, and the same results were obtained for 316L. These results are in line with the change in the equilibrium potential with temperature, expressed by the Nernst equation. For DSS, the decrease in potential was more prominent for the tests conducted with 600 ppm chloride. Similar results have been obtained by Muñoz et al. [83]. The corrosion study observed decreasing OCP with increasing temperature for both austenitic stainless steels and DSS.

Both  $E_{crev}$  and  $E_{rep}$ , presented in Table 5.6 - Table 5.9 decreased with increasing temperature. This indicates that crevice corrosion is easier initiated and repassivation becomes more difficult at higher temperatures. This corresponds well with the fact that the corrosion tendency increases with increasing temperature [31] and higher temperatures result in a more porous and less protective passive film [33], as stated in Section 2.4.1.

As illustrated in Figure 5.4 - Figure 5.7,  $E_{rep}$  values were very high and the hysteresis loops were almost non-existent for the tests conducted at 30 °C. These samples did experience corrosion attacks, as can be observed from the overview images presented in Figure 5.28 and the more detailed images presented in Figure 5.37 and Figure 5.36. These corrosion attacks are called transpassive attacks and occurs when the sample reach the transpassive potential during the forward scan of the polarization curve. At the transpassive potential, Cr starts dissolving into the electrolyte from the passive layer, resulting in a weaker passive film that enables the corrosion attack [84]. As can be observed from the images in Figure 5.37 and Figure 5.36, the phase/grain boundaries are attacked. This is typical for a transpassive attack [85]. Even if the attack has been initiated, it is not stable, and thus does not affect  $E_{rep}$ . Transpassive corrosion occurs at temperatures below CPT or CCT [84][85], in this case CCT. This is probably why DSS experienced transpassive attacks only at 30 °C, since 95 °C is above CCT for DSS [85]. These kind of attacks were not observed on 316L samples, because CCT for 316L is below 30 °C [84].

$E_{rep}$  values for the tests conducted at 95 °C presented in Table 5.7 have been stated as 0.11 V vs. Ag/AgCl. However, the anodic CPP curves, presented in Figure 5.5 show that the reversed scanning curves crosses the forward scanning curve at -0.21 V vs. Ag/AgCl. These samples seem to have experienced a stronger passive current, resulting in the sudden drop in potential at the reversed scan curve.  $E_{rep}$  values for these curves were therefore stated as 0.11 V vs. Ag/AgCl, as it is believed that  $E_{rep}$  would have been approximately 0.11 V vs. Ag/AgCl without the potential drop. This potential has been obtained based on the curves presented in Figure 5.25, where all the reversed scanning curves were almost identical until the drop.  $E_{rep}$  similar to the two curves that did not experienced the potential drop was therefore chosen. Similar behaviour was observed for

316L as well at this test condition, presented in Figure 5.19. The potential drop was however not as evident and  $E_{rep}$  was therefore stated as the cross section between the reversed scanning and the forward scanning curves for these tests.

## 6.2 Effect of chloride concentration

### 6.2.1 AISI 316L stainless steel

The parameters presented in Table 5.10 and Table 5.11 were established during the specialization project [1]. It was concluded that it was no clear trend regarding the effect of chloride concentration on OCP and  $E_{corr}$ , and it seemed like chloride concentration did not affect these parameters. At all temperatures,  $E_{crev}$  decreased with increasing chloride concentration, indicating that crevice corrosion was easier initiated at higher chloride concentrations. A relationship between the effect of chloride concentration and temperature on repassivation of the surface was observed. Similar results have been observed by Mameng et al. [82]. The report stated that at low temperatures, the crevice growth will be slow enough to make it the rate determining process, as crevices will passivate at sufficient low temperatures. If the solution is sufficient saturated with chloride ions, the crevice chemistry can be maintained even at low temperatures [82].

All the tests purged with  $CO_2$  were conducted during this thesis, and the parameters obtained during these tests are presented in Table 5.12 and Table 5.13. At 30 °C, OCP and  $E_{corr}$  decreased with increasing chloride concentration. At 95 °C no or little change in the potentials were observed when the chloride concentration was changed. The only exception was one of the tests with 600 ppm chloride, which had higher OCP and  $E_{corr}$  than the other test in the parallel. Based on the potentials obtained for this test, OCP and  $E_{corr}$  decreased with increasing chloride concentrations, as for the tests at 30°C. Overall, it seemed like OCP and  $E_{corr}$  was affected by change in chloride concentration at lower temperatures, while at higher temperatures, the temperature was the dominating parameter.

As presented in Figure 5.9 and Figure 5.10,  $E_{crev}$  decreased with increasing chloride concentration. This indicates that crevice corrosion is easier initiated when the chloride concentration is higher. The same results were obtained for the tests purged with  $N_2$  conducted during the specialization project, as stated above. The results agree with the fact that higher chloride concentration increases the probability of chloride ions to breakdown the passive film, as more chloride ions are available. A breakdown of the passive film will increase the risk of corrosion initiation [35], as stated in Section 2.4.2. Figure 6.2 presents a model graph created in Design-Expert and illustrates the change in  $E_{crev}$  with temperature and chloride content at an average pH value. The  $E_{crev}$  values are illustrated as the lines in the image, and the numbers on the lines are the potential values in V vs. Ag/AgCl. The graph shows that  $E_{crev}$  increase at lower chloride concentration and temperature.

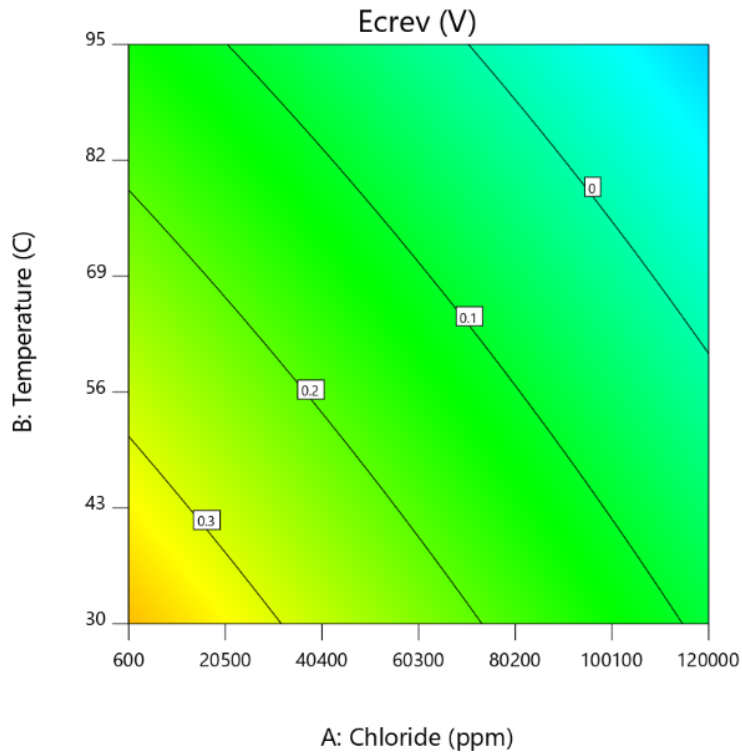


**Figure 6.1:** Change in  $E_{crev}$  with chloride concentration and temperature for 316L at pH 6.05, created in Design-Expert.

The curves presented in Figure 5.9 and Figure 5.10 showed that  $E_{rep}$  was more negative when the chloride concentration was high, which indicates that repassivation is more difficult at higher chloride concentrations. This result corresponds well with the fact that higher chloride concentration increases the probability of chloride ions to be adsorbed, causing local dissolution of the film or to penetrate through the passive film, which makes repassivation more difficult [35], as stated in Section 2.4.2. This was the case for all tests except the ones at 95 °C with 600 ppm and 5000 ppm chloride.  $E_{rep}$  for these tests was in the same area, as illustrated in Figure 5.10. At these test conditions it seemed like the increase in chloride concentration needed to be more severe to affect repassivation of the surface. The potential decreased significant when the chloride concentration was further increased to 120 000 ppm. Overall, for both the tests purged with  $N_2$  and  $CO_2$ ,  $E_{rep}$  decreased with increasing chloride concentration. The change in  $E_{rep}$  with temperature and chloride content at an average pH value is illustrated in Figure 6.2, created in Design-Expert.

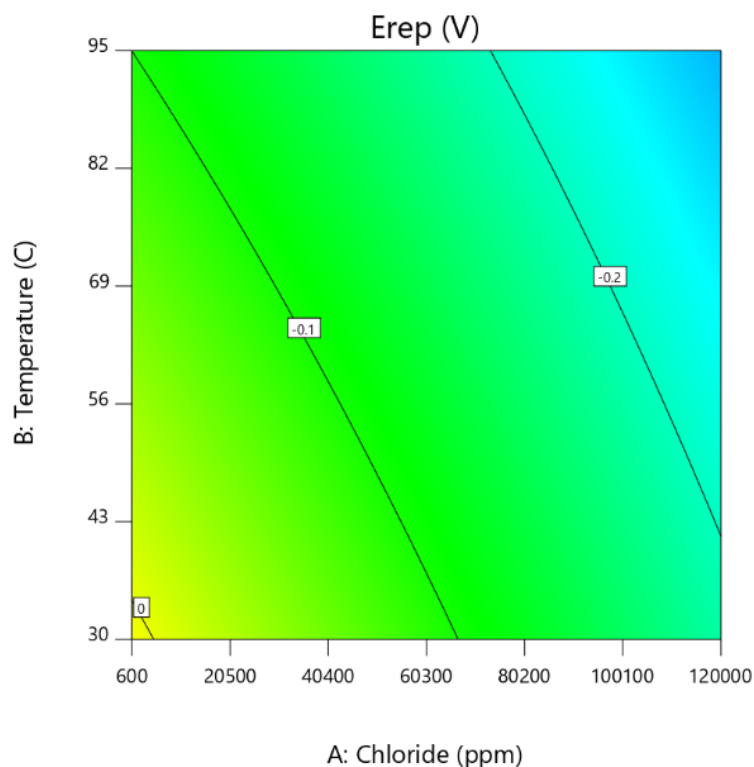


**Figure 6.2:** Change in  $E_{rep}$  with chloride concentration and temperature for 316L at pH 6.05, created in Design-Expert.

### 6.2.2 22% Cr duplex stainless steel

OCP and  $E_{corr}$  presented in Table 5.14 - Table 5.17, decreased with increasing chloride concentrations for the tests completed at 30 °C. This was the case regardless of the pH. At 95 °C, the potentials showed no or minor changes with increasing chloride concentration for the tests purged with CO<sub>2</sub>. For the tests purged with N<sub>2</sub>, the potentials showed minor changes when the chloride concentration was increased from 600 ppm to 5000 ppm. When the chloride concentration was further increased to 120 000 ppm the potentials increased significantly. Consequently, there is no clear trend regarding change in OCP and  $E_{corr}$  with chloride concentration.

$E_{crev}$  obtained from the anodic CPP curves, illustrated in Figure 5.12 - Figure 5.15, showed that the crevice corrosion potential decreased with increasing chloride concentration. This was the case regardless of temperature and pH, and indicates that crevice corrosion is easier initiated when the chloride concentration is higher. The same results were obtained for 316L. Figure 6.2 is created in Design-Expert and presents the change in  $E_{crev}$  with temperature and chloride content at an average pH value. This illustrates the increase in  $E_{crev}$  with decreasing chloride concentration and temperature.

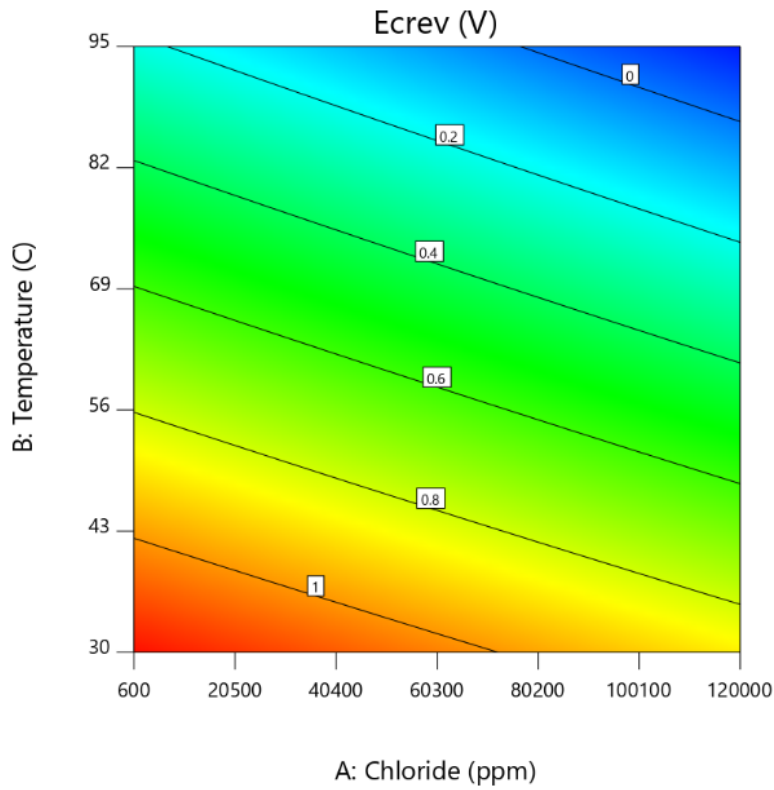


**Figure 6.3:** Change in  $E_{crev}$  with chloride concentration and temperature for DSS at pH 6.0, created in Design-Expert.

As for the crevice corrosion potential, the obtained  $E_{rep}$  values decreased with increasing chloride concentration for all the tests, regardless of temperature and pH. This indicates that it is more difficult for the surface to repassivate at higher chloride concentrations. The results corresponds well with the results for 316L, discussed above. How  $E_{rep}$  changes with temperature and chloride concentration at an average pH is illustrated by the model graph created in Design-Expert, presented in Figure 6.4.



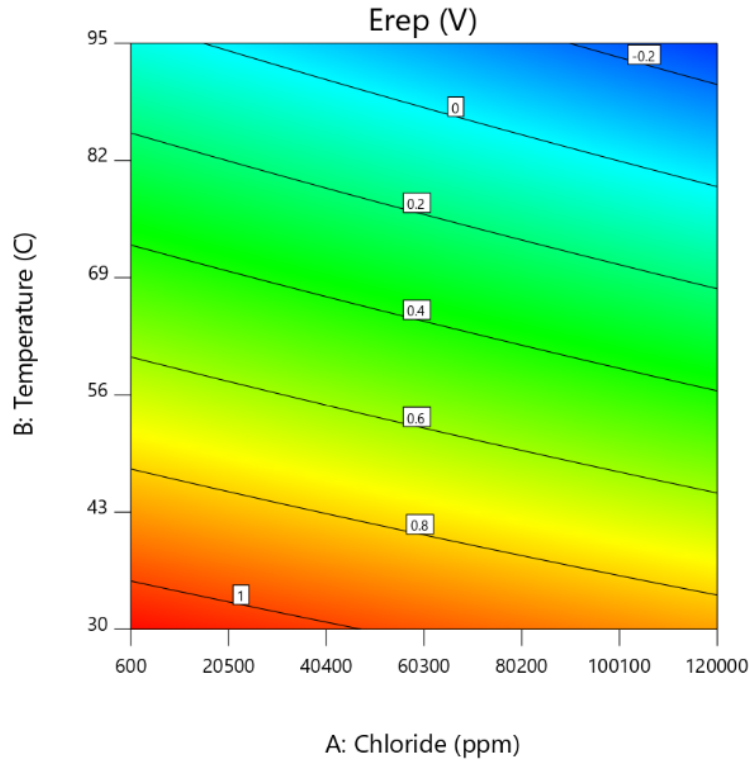


**Figure 6.4:** Change in  $E_{rep}$  with chloride concentration and temperature for DSS at pH 6.0, created in Design-Expert.

## 6.3 Effect of pH

### 6.3.1 AISI 316L stainless steel

Common for the tests conducted with 316L at 95 °C are that OCP and  $E_{corr}$  increased at lower pH values, regardless of the chloride concentration. For the tests conducted at 30 °C, the difference in OCP and  $E_{corr}$  for tests conducted with 600 ppm was small, while the potentials increased with increasing pH for the tests conducted with 120 000 ppm chloride. There is therefore no clear trend regarding change in OCP and  $E_{corr}$  with pH, for the pH range tested.

There is also no clear trend regarding change in  $E_{crev}$  and  $E_{rep}$  within the tested pH range. For the tests conducted in electrolytes with 600 ppm and 120 000 ppm chloride at 95 °C, both  $E_{crev}$  and  $E_{rep}$  decreased with decreasing pH. This indicates that crevice corrosion is easier initiated and it is more difficult for the surface to repassivate when the pH is low. This result agrees with the fact that the passive film will be weakened in an acidic solution [5] and become thinner [39], as stated in Section 2.4.3. A weaker passive film makes it easier to initiate crevice corrosion crevice corrosion. The tests conducted with 120 000 ppm at 30 °C showed similar results, with the exception of one of the tests purged with  $CO_2$ , presented in Table 5.19. As stated in Section 5.1, the results regarding this test condition deviated a lot, as there was a significant difference in obtained  $E_{rep}$  values within the parallel. The tests conducted with electrolytes with 5000 ppm chloride at 95 °C and 600 ppm chloride at 30 °C showed the opposite results. Both  $E_{crev}$  and

$E_{rep}$  increased with decreasing pH. The obtained results show no clear trend regarding the effect of pH on the corrosion properties of 316L at the test conditions tested. As the effect of pH on  $E_{crev}$  and  $E_{rep}$  varies, it seems like other factors may have bigger effect than the pH change. These factors may be differences on the sample surfaces, difficulties with reproduction of the tests or the fact that different setups were used for the tests conducted in the higher and lower pH ranges.

### 6.3.2 22% Cr duplex stainless steel

OCP and  $E_{corr}$  of DSS are presented in Table 5.23 - Table 5.27. Both potentials increased with increasing pH for tests conducted at 30 °C. It should however be mentioned that the result within the parallels varies, especially for the tests with 600 ppm chloride. OCP and  $E_{corr}$  decreased with increasing pH for the tests conducted with 600 ppm and 5000 ppm chloride at 95 °C, while the potentials increased with increasing pH when the chloride concentration was 120 000 ppm. As for 316L, no clear trend was observed regarding the change of OCP and  $E_{corr}$  with pH.

As presented in Table 5.23 - Table 5.27,  $E_{crev}$  values increased with decreasing pH. This with the exception of the test conducted with 5000 ppm chloride at 95 °C. The results indicate that it is more difficult to initiate crevice corrosion at lower pH values. This is the opposite effect of pH on  $E_{crev}$  that was expected, according to Section 2.4.3. As observed from the curves presented in Figure 5.4 - Figure 5.7, the difference in the potentials are however not that big, compared to the difference in potentials created when changing chloride concentration or temperature, discussed in the previous sections. The results indicate that pH has little effect on  $E_{crev}$  of DSS in the tested pH range. One possible explanation is that the difference between the pH values tested was too small. pH varied between 4.1 and 5.5 for the tests purged with CO<sub>2</sub> and 6.5 and 8.5 for the tests purged with N<sub>2</sub>. Similar results have been observed by Tzaneva [40], as stated in Section 2.4.3. The report stated that pH of the solution had little or no significant influence on the corrosion behaviour when the pH was above 2. The little influence of pH on the pitting potential was explained by the stability of the passive film. It was stated that this was probably due to the high Cr and N content in the steel [40]. To experience a more evident effect of pH, more extreme pH values should have been tested.

Obtained  $E_{rep}$  values, presented in Table 5.23 - Table 5.27 indicate that repassivation was little affected by the pH as well. Obtained  $E_{rep}$  values from tests with 600 ppm chloride at both temperatures was more or less the same regardless of the pH. For the tests conducted with 120 000 ppm chloride at 30 °C,  $E_{rep}$  was higher at lower pH. However, the difference between  $E_{crev}$  and  $E_{rep}$  was the same regardless of the pH. The increased  $E_{rep}$  seemed to be due to the higher  $E_{crev}$  for these tests, and not because it was more difficult for the surface to repassivate. For the tests conducted with 5000 ppm and 120 000 ppm chloride at 95 °C,  $E_{rep}$  increased with decreasing pH. This indicates that repassivation of the surface became more difficult when the solution had a higher pH. With that said, the obtained  $E_{rep}$  for the tests with 120 000 ppm chloride and purged with N<sub>2</sub> varied within the parallel, which makes it difficult to state how much the pH affected the repassivation.

## 6.4 Data analysis by DOE

In addition to create model graphs, Design-Expert was also used to evaluate the effect of the parameters tested. To evaluate the significance each parameter had in the model, Design-Expert used Analysis of variance (ANOVA). ANOVA is a collection of statistical models and provides a statistical analysis of the data [5][60]. The p-values for the independent variables, i.e. temperature, chloride content and pH, are calculated by the software. If the p-value is smaller than the uncertainty or risk degree (which was 5% in this case), a significant correlation between the independent and the dependent variable exist [5]. The corrosion properties obtained from the anodic CPP curves are the dependent variables. A Two Factor Interaction (2FI) model was chosen, as this model was the best fit.

Based on the ANOVA results for the 2FI model, temperature was the most significant model term regarding  $E_{crev}$  for 316L, followed by the chloride concentration. Chloride concentration had the most significant effect on  $E_{rep}$  for 316L, followed by the temperature. Temperature and chloride concentration were the only parameters recognized as significant by the software regarding  $E_{crev}$  and  $E_{rep}$  for 316L, based on their p-values.

As for 316L, ANOVA results for the 2FI model showed that for DSS temperature and chloride concentration were the significant model terms regarding  $E_{crev}$  and  $E_{rep}$ . Temperature and chloride concentration were equally significant regarding their effect on both potentials, as their p-values were equal.

Analysis of the obtained corrosion values, completed with ANOVA in Design-Expert showed that pH was not a significant model term for either of the corrosion properties discussed above. pH was recognized as not significant by the software due to the terms p-value. This was the case for both 316L and DSS.

## 6.5 Surface characterization

### 6.5.1 AISI 316L stainless steel

The surface characterization included overview images, used to obtain percentage of the surface consisting of crevices at the different test conditions. The results, presented in Table 5.28 indicate that the samples tested at 30 °C obtained a higher crevice percentage. The anodic CPP curves recorded for the 316L samples had a larger hysteresis loop for the tests at 30 °C compared to the tests at 95 °C. The corrosion attacks are dependent of the charge,  $Q$ . The charge is dependent on both the anodic current and time the anodic current goes through the sample. As can be observed from the curves tested at 30 °C, these curves used longer total time to first reach maximum current after reaching  $E_{crev}$  and then to reach  $E_{rep}$  after the scan direction was reversed. This have caused the more severe corrosion attacks at the sample tested at 30 °C (by using Faraday's law).

Average weight loss at each test condition, presented in Table 5.29, show that the test conditions that obtained the highest crevice percentages, test conditions 3 and 9, had the highest weight loss as well. With the exception of test condition 9 and 11, the samples tested is electrolytes purged with CO<sub>2</sub> experienced a higher weight loss. It is believed that this was not caused by the lower pH, but because different setups were used. The samples

exposed to an electrolyte purged with CO<sub>2</sub>, were tested with setup 2. At these tests, the scan was reversed at a higher current, which resulted in longer time for the curves to reach maximum current and may have caused the more severe corrosion attacks.

### 6.5.2 22% Cr duplex stainless steel

Percentage of the DSS sample surface consisting of crevices at the different test conditions, presented in Table 5.30, was higher for the samples exposed to lower chloride concentrations. The same explanation used regarding the higher percentage obtained for 316L samples exposed to 30 °C also applies in this case. At lower chloride concentrations, the anodic current went through the sample for a longer amount of time. This may be the reason these samples experienced more extensive surface changes.

Average weight loss at each test condition, presented in Table 5.29, indicates that the corrosion attacks observed on the samples tested at test condition 1 and 3 were shallow. These test conditions obtained the highest crevice percentage, but not as great weight loss compared to the other test conditions. The results showed that the samples exposed to 95 °C had the highest weight loss. The measured crevice depths of the crevices presented in Figure 5.36 - Figure 5.39, showed that the crevice on the sample tested at 95 °C was deeper than the ones tested at 30 °C. It should however be mentioned that it is possible that deeper crevices than the selected ones has been formed on the samples during the tests.

## 6.6 Material comparison

When comparing the corrosion properties for the two materials, the results obtained during this thesis would be more comparable as these tests were conducted with the same setup. The results obtained during the specialization project were decided to be included to ensure that as many test conditions as possible were evaluated.

Considering OCP and  $E_{corr}$  obtained from the anodic CPP curves, the potentials obtained of DSS were in general more positive than those of 316L. This with the exception of a few tests, where obtained OCP and  $E_{corr}$  of DSS were more negative than those of 316 tested at the same test condition. However, the deviation within the parallels was greater than the difference in potentials between the materials regarding these tests. These results indicates that DSS has higher corrosion resistance than 316L at the tested conditions due to a more resistant passive film.

Regarding obtained  $E_{crev}$ , DSS experienced more positive potentials than 316L at all test conditions, except the tests with 600 ppm and 120 000 ppm chloride, purged with N<sub>2</sub> at 95 °C. The potentials obtained at these test conditions were almost similar for the two materials. It should be mentioned that the tests with 316L and DSS at these test conditions were conducted with different setups. The higher potentials obtained for DSS indicate that DSS has a higher resistance towards crevice corrosion, as crevices are easier initiated on 316L. Especially the tests conducted at 30 °C resulted in much higher  $E_{crev}$  for DSS compared to 316L. This indicates that at lower temperatures, DSS is much more resistant towards crevice corrosion, but this advantage becomes less evident at higher temperatures.

According to the obtained  $E_{rep}$  values, repassivation was easier obtained for DSS than 316L.  $E_{rep}$  was more positive for DSS at all test conditions compared to 316L, with exception of the tests with 120 000 ppm chloride, purged with  $N_2$  at 95 °C. The results within both the DSS and the 316L parallel at this tests condition deviated, and the overall trend showed less negative potentials for DSS. Especially the tests conducted at 30 °C resulted in much higher  $E_{rep}$  for DSS compared to 316L. This indicates that at lower temperatures, the DSS surface repassivates much easier, but as for crevice initiation, this advantage becomes less evident at higher temperatures.

Comparing the model graphs, presented in Figure 6.2 - Figure 6.4, it is clear that the change in  $E_{crev}$  and  $E_{rep}$  with temperature and chloride content are much higher for DSS than 316L. This is also illustrated by the much higher  $E_{crev}$  values obtained for DSS during the tests at 30 °C, especially. The results indicate that DSS is more affected by the change in these environmental parameters, most likely because DSS is more corrosion resistant than 316L at lower temperatures and chloride concentrations. At higher chloride concentration and temperature, the results indicates that DSS has better corrosion properties than 316L, but the difference between the corrosion resistance of the materials are considerably smaller.

The obtained results are as expected considering that DSS in general posses a higher corrosion resistance than 316L, as stated in Section 2.1. As presented in Table 4.3, DSS has higher  $PRE_N$  than 316L, which indicates that DSS has higher corrosion resistance based on the alloy composition. According to Tzaneva [40], in the pH region between 4 and 8, higher alloyed steel with higher Cr content, similar to DSS has better corrosion stability to general and pitting corrosion compared to the stainless steels with lower Cr content. This fits well with the obtained results in this thesis.

## 6.7 OCP measurements

The only OCP measurements conducted with different oxygen contents during this thesis were the tests conducted with 120 000 ppm chloride at 30 °C and 95 °C, which were carried out in electrolytes saturated with oxygen, presented in Figure 5.45 and without oxygen, presented in Figure 5.43 and Figure 5.44. The results showed an increased OCP when oxygen was present at both temperatures tested. This was the same observation done by Equinor [76] and presented in Figure 5.42 in their test.

Stable OCP values were observed for both materials during the measurements where oxygen had been removed, presented in Figure 5.40 - Figure 5.44. OCP values obtained in electrolytes with 600 ppm chloride, presented in Figure 5.40 and Figure 5.41, showed decreasing OCP with increasing temperature for both materials. The same result was observed for the OCP measurement saturated with oxygen, presented in Figure 5.45 and during the anodic CPP measurements, discussed in Section 6.1. The OCP measurements conducted with 120 000 ppm chloride without oxygen deviated from this result. OCP obtained at 95 °C, presented in Figure 5.44 obtained a higher value than expected and were close to the potentials obtained at the same test condition when the electrolyte was saturated with oxygen. It is believed that the increased potential was caused by oxygen ingress as a result of NaCl crystallizing in the gas inlet tube, blocking  $N_2$  gas from entering the electrolyte. This was the case for both tests conducted with 120 000 ppm chloride, and the uncertainty in the results makes it is difficult to discuss the effect

of chloride concentration based on the OCP measurements. The result from the anodic CPP measurements showed that chloride concentration had an effect on OCP at lower temperatures and OCP decreased with increasing concentration for the tests at 30 °C. No clear trend regarding which material that obtained the highest OCP were observed from the OCP measurements.

By examine the change in OCP with dissolved oxygen content presented in Figure 3.1, it is observed that the most severe increase in OCP occurs when oxygen is introduced to the system, even in small concentrations. After oxygen has been introduced and the dissolved oxygen content is further increased, OCP continues to increase, but not to the same extent. The reason for this behavior is that when oxygen enters the system the rate of the cathodic reaction increases. Increased oxygen content increases the cathodic reaction rate, as stated in Section 3.1.

Figure 6.5 illustrates where obtained  $E_{crev}$  and  $E_{rep}$  are positioned relative to the OCP at the different oxygen contents. OCP values are presented as dashed lines. The 100 ppb, 200 ppb and 500 ppb dashed lines correspond to the OCP measured at these oxygen contents by Equinor [76] in Figure 3.1. The line representing oxygen content < 10 ppb corresponds to the OCP measurement presented in Figure 5.42. Both the measurements presented in Figure 3.1 and in Figure 5.42 were conducted in solutions with 19 000 ppm chloride at 45 °C, with pH 7.5 and 7.1-7.8, respectively.  $E_{crev}$  and  $E_{rep}$  values obtained with 600 ppm and 120 000 ppm chloride at 30 °C and 95 °C are presented as intervals in Figure 6.5, based on minimum and maximum values from the two parallel test samples. Because the tests purged with N<sub>2</sub> had pH values closer to the pH during the OCP measurements,  $E_{crev}$  and  $E_{rep}$  obtained from these tests were considered.

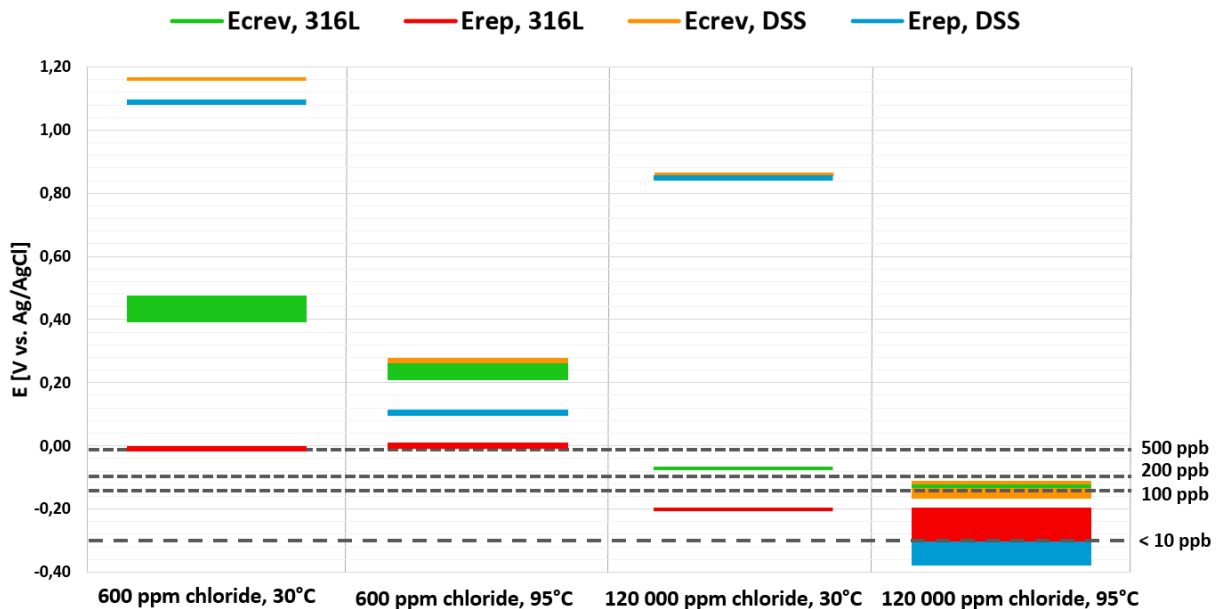


**Figure 6.5:** Illustration of obtained  $E_{crev}$  and  $E_{rep}$  from anodic CPP measurements and OCP at different oxygen contents, created by the author. OCP at 100 ppb, 200 ppb and 500 ppb oxygen are obtained from measurements conducted by Equinor, presented in Figure 3.1.

No anodic CPP tests with 19 000 ppm chloride at 45 °C were conducted, and the comparison of the OCP at the different oxygen contents will therefore not be precise.

It was established previously in the discussion that the OCP decreased with increasing temperature. For this reason, OCP at the different oxygen contents would probably be more negative at 95 °C and more positive at 30 °C, compared to the obtained potentials at 45 °C.

As observed in Figure 6.5, obtained  $E_{rep}$  for both materials in electrolytes with 120 000 ppm chloride at 95 °C, are at the same potential as the dashed line representing oxygen content < 10 ppb. OCP measured at the same test condition without oxygen, presented in Figure 5.44 was also within the  $E_{rep}$  intervals for both materials. 316L and DSS should therefore not be used at this test condition when oxygen is present, if the oxygen application limit is defined as  $E_{rep}$ . According to the illustration, DSS could be used at the other test conditions with at least 500 ppb oxygen present. 316L should have an oxygen limit between 10 ppb and 100 ppb oxygen in solutions with 120 000 ppm chloride at 30 °C, and a limit approximately at 500 ppb oxygen in solutions with 600 ppm chloride at 30 °C and 95 °C. As mentioned earlier, the potentials would most likely change with temperature and the limits are probably lower for the tests conducted at 95 °C and higher for the tests conducted at 30 °C.

No corrosion attacks were observed on the samples after the OCP measurements. Even when the test electrolyte was saturated with oxygen and the samples experienced OCP above  $E_{crev}$ , no crevices were observed. This was expected as stable OCP values were observed and was most likely due to the fact that the measurements were conducted without the crevice assembly. No pits were observed on the samples either, and can be explained by the fact that  $E_{pit}$  is more positive than  $E_{crev}$ .





## 7 Conclusion

The results after the anodic CPP measurements showed that the obtained  $E_{crev}$  values decreased with increasing chloride concentration and temperature for both 316L and DSS. Increased temperature results in decreased resistance to breakdown of the passive film and more chloride ions available increases the probability of passive film breakdown. Higher chloride concentrations and temperatures had the same effect on  $E_{rep}$ . Obtained  $E_{rep}$  from the anodic CPP curves decreased with increasing chloride concentration and temperature for both materials. Higher temperature increases the crevice tendency and makes it more difficult for the surface to repassivate. More chloride ions adsorbed on the surface makes it difficult for the passive film to be restored as well. As crevice corrosion is easier initiated and repassivation of the surface becomes more difficult, the corrosion resistance of 316L and DSS are reduced at higher chloride concentrations and temperatures. For the pH values tested, change in pH had no significant effect on  $E_{crev}$  and  $E_{rep}$ .

The results obtained using ANOVA in Design-Expert showed that temperature and chloride content were the only parameters that had a significant effect on  $E_{crev}$  and  $E_{rep}$ . Temperature had the most significant effect on  $E_{crev}$ , and chloride content had the most significant effect on  $E_{rep}$  regarding 316L. For DSS, both parameters were equally significant regarding their effect on  $E_{crev}$  and  $E_{rep}$ . DOE proved to be an important tool regarding analysis of the experimental results and procedure.

By comparing the corrosion properties obtained from the anodic CPP curves, DSS proved to be more resistant towards crevice corrosion than 316L. This is believed to be caused by the higher Cr, Mo and N content and thereby higher  $PRE_N$  of DSS.

OCP measurements showed that increased oxygen content increased OCP of the materials and brought it closer to the oxygen application limit, defined as  $E_{rep}$ . OCP of both 316L and DSS in solutions with 120 000 ppm chloride at 95 °C reached the application limit when the oxygen content was < 10 ppb. To establish oxygen application limits for 316L and DSS at the other test conditions, OCP measurements with different dissolved oxygen contents must be conducted.



## 8 Further work

This thesis studied only maximum and minimum temperature and only a few additional middle points regarding chloride concentration. To enable more accurate conclusions about the effect of the different parameters on the crevice corrosion of 316L and DSS, more tests of the same nature at concentrations and temperature between maximum and minimum should be performed. DOE should be used to extrapolate these test conditions. To investigate the effect of pH further, tests with more extreme pH values should be performed.

The effect of increasing the maximum current before reversing the scanning direction during the anodic CPP were not investigated. Whether and if so, how the change of maximum current affected the corrosion properties obtained from the curves should be investigated.

In further work OCP measurements with different oxygen contents should be conducted to define the critical oxygen content at the different test conditions.

Tests with SDSS should be conducted as well, to investigate the effect of the different parameters on SDSS and compare crevice corrosion properties for the different materials. This is important since SDSS often is used in production systems as an alternative to DSS.



## References

- [1] M. E. Edvardsen. Crevice corrosion of AISI 316L stainless steel in low oxygen environments – the effect of chloride content, pH and temperature. Specialization project report in TMT4500, Department of Materials Science and Engineering, NTNU – Norwegian University of Science and Technology, Dec. 2019.
- [2] A. A. Wahaibi, T. A. Nabhani, P. R. Flores, and N. A. Behalni. Evaluation of the effect of oxygen on CRA materials. In *Corrosion 2018*, pages 1–12, Arizona, USA, 2018. NACE International. Conference Paper.
- [3] Z Schulz, P. Whitcraft, and D. Wachowiak. Availability and economics of using duplex stainless steels. In *Corrosion 2014*, pages 1–10, USA, 2014. NACE International. Conference Paper.
- [4] A. A. Dastgerdi, A. Brenna, M. Ormellese, M. Pedferri, and F. Bolzoni. Application of DOE to study the effect of environmental parameters on localized corrosion. In *Corrosion 2019*, pages 1–9, USA, 2019. NACE International. Conference Paper.
- [5] A. A. Dastgerdi, A. Brenna, M. Ormellese, M. Pedferri, and F. Bolzoni. Experimental design to study the influence of temperature, pH, and chloride concentration on the pitting and crevice corrosion of UNS s30403 stainless steel. *Corrosion Science*, 159:1–9, 2019.
- [6] K. V. Rybalka, L. A. Beketaevaa, and A. D. Davydov. Effect of dissolved oxygen on the corrosion rate of stainless steel in a sodium chloride solution. *Russian Journal of Electrochemistry*, 54(12):1284–1287, 2018.
- [7] V. Burt. *Corrosion in the Petrochemical Industry*. ASM International, 2nd edition, 2015.
- [8] J. H. Qiu. Passivity and its breakdown on stainless steels and alloys. *Surface Interface Analysis*, 33:830–833, 2002.
- [9] J. K. Solberg. *Teknologiske metaller og legeringer*. NTNU, 2017.
- [10] M. F. McGuire. *Stainless Steels for Design Engineers*. ASM International, Ohio, 2008.
- [11] C. O. A. Olsson and D. Landolt. Passive films on stainless steels - chemistry, structure and growth. *Electrochimica Acta*, 48(9):1093–1104, 2003.
- [12] J. R. Davis. *Stainless Steels*. ASM International, Ohio, 1994.
- [13] C. R. Clayton and I. Oljefjord. Passivity of austenitic stainless steels. In *Corrosion Mechanisms in Theory and Practice*, pages 327–346. Taylor & Francis Group, 2011.
- [14] ASTM International. *A312/A312M-19 Standard Specification for Seamless, Welded, and Heavily Cold Worked Austenitic Stainless Steel Pipes*. ASTM International, West Conshohocken, PA, 2019.

- [15] ASTM International. *A182/A182M20 Standard Specification for Forged or Rolled Alloy and Stainless Steel Pipe Flanges, Forged Fittings, and Valves and Parts for High-Temperature Service*. ASTM International, West Conshohocken, PA, 2020.
- [16] J. A. Platt, A. Guzman, A. Zuccari, D. W. Thornburg, B. F. Rhodes, Y. Ossida, and B. K. Moore. Corrosion behavior of 2205 duplex stainless steel. *Am. J. Orthod. Dentofacial Orthop.*, 112(1):69–79, 1997.
- [17] L. Freire, M. A. Catarino, M. I. Godinho, M. J. Ferreira, M. G. S. Ferreira, A. M. P. Simões, and M. F. Montemora. Electrochemical and analytical investigation of passive films formed on stainless steels in alkaline media. *Cement and Concrete Composites*, 34(9):1075–1081, 2012.
- [18] R. Jiang, Y. Wang, X. Wen, C. Chen, and J. Zhao. Effect of time on the characteristics of passive film formed on stainless steel. *Applied Surface Science*, 412:214–222, 2017.
- [19] A. Kocijan, C. Donik, and M. Jenko. Electrochemical and xps studies of the passive film formed on stainless steels in borate buffer and chloride solutions. *Corrosion Science*, 49(5):2083–2098, 2007.
- [20] Vignat V., H. Zhang, O. Delrue, O. Heintz, I. Popa, and J. Peultier. Influence of long-term ageing in solution containing chloride ions on the passivity and the corrosion resistance of duplex stainless steels. *Corrosion Science*, 53(3):894–903, 2011.
- [21] S. Mischler, A. Vogel, H. J. Mathieu, and D. Landolt. The chemical composition of the passive film on Fe-24Cr and Fe-24Cr-11Mo studied by AES, XPS and SIMS. *Corrosion Science*, 32(9):925–944, 1991.
- [22] W.-C. Baek, T. Kang, H.-J. Sohn, and Y. T. Kho. In situ surface enhanced raman spectroscopic study on the effect of dissolved oxygen on the corrosion film on low carbon steel in 0.01 M NaCl solution. *Electrochimica Acta*, 46(15):2321–2325, 2001.
- [23] A. J. Sedriks. *Corrosion of Stainless Steels*. John Wiley & Sons, Ltd., New York, 2nd edition, 1996.
- [24] Z. Szklarska-Smialowska. *Pitting Corrosion of Metals*. National association of corrosion engineers, 1986.
- [25] N. J. Laycock, J. Stewart, and R. C. Newman. The initiation of crevice corrosion in stainless steels. *Corrosion Science*, 39(10–11):1791–1809, 1997.
- [26] A. J. Betts and L. H. Boulton. Crevice corrosion: review of mechanisms, modelling, and mitigation. *British Corrosion Journal*, 28(4):279–296, 1993.
- [27] ASTM International. *NACE/ASTMG193-12d Standard Terminology and Acronyms Relating to Corrosion*. ASTM International, Conshohocken, PA, 2012.
- [28] J. Kruger. Corrosion of metals: Overview. In *Encyclopedia of Materials: Science and Technology*, pages 1701–1706. Elsevier Ltd., 2nd edition, 2001.

- [29] J. D. Henderson, N. Ebrahimi, V. Dehnavi, M. Guo, D. W. Shoesmith, and J. J. Noël. The role of internal cathodic support during the crevice corrosion of Ni-Cr-Mo alloys. *Electrochimica Acta*, 283:1600–1608, 2018.
- [30] M. A. M. Ibrahim, S. S. Abd El Rehim, and M. M. Hamza. Corrosion behavior of some austenitic stainless steels in chloride environments. *Materials Chemistry and Physics*, 115(1):80–85, 2009.
- [31] S. Matsch and H. Böhni. Influence of temperature on the localized corrosion of stainless steels. *Russian Journal of Electrochemistry*, 36(10):1122–1128, 2000.
- [32] W. Bogaerts, A. Van Haute, and M. J. Brabers. Proceedings of the 8th international congress on metallic corrosion, 1981. Mainz, West Germany.
- [33] J-H. Wang, C. C. Su, and Z. Szklarska-Smialowska. Effects of  $\text{Cl}^-$  concentration and temperature on pitting of AISI 304 stainless steel. *Corrosion Science*, 44(10):732–737, 1988.
- [34] A. U. Malik, P. C. Mayan Kutty, N. A. Siddiqi, I. N. Andijani, and S. Ahmed. The influence of pH and chloride concentration on the corrosion behaviour of AISI 316L steel in aqueous solutions. *Corrosion Science*, 33:1809–1827, 1992.
- [35] A. J. Sedriks. Plenary lecture—1986: Effects of alloy composition and microstructure on the passivity of stainless steels. *Corrosion*, 42(7):376–389, 1986.
- [36] V. Hospadaruk and J. V. Petrocelli. The pitting potential of stainless steels in chloride media. *Journal of The Electrochemical Society*, 113(9):878–883, 1966.
- [37] C.T. Kwok, H.C. Man, and L.K. Leung. Effect of temperature, pH and sulphide on the cavitation erosion behaviour of super duplex stainless steel. *Wear*, 211(1):84–93, 1997.
- [38] A. Fattah-alhosseini and S. Vafaeian. Effect of solution pH on the electrochemical behaviour of AISI 304 austenitic and AISI 430 ferritic stainless steels in concentrated acidic media. *Egyptian Journal of Petroleum*, 24(3):333–341, 2015.
- [39] V. Marcus, P. and Maurice and H.-H. Strehblow. Localized corrosion (pitting): A model of passivity breakdown including the role of the oxide layer nanostructure. *Corrosion Science*, 50(9):2698–2704, 2008.
- [40] B. Tzaneva. Effect of pH on the corrosion behaviour of high nitrogen stainless steel in chloride medium. *Journal of Chemical Technology and Metallurgy*, 48(4):383–390, 2013.
- [41] J. A. Wharton and R. J. K. Wood. Influence of flow conditions on the corrosion of AISI 304L stainless steel. *Wear*, 256(5):525–536, 2004.
- [42] T. Shibata and Y. Zhu. The effect of flow velocity on the pitting potential of anodized titanium. *Corrosion Science*, 37(2):343–346, 1995.
- [43] T. R. Beck and S. G. Chan. Experimental observations and analysis of hydrodynamic effects on growth of small pits. *Corrosion*, 37(11):665–671, 1981.

- [44] G. J. Jr Danek. The effect of sea-water velocity on the corrosion behavior of metals. *Naval Engineers Journal*, 78(5):763–769, 1966.
- [45] B. W. Brown, H. H. Lu, and D. J. Duquette. Effect of flow rates on localized corrosion behavior of 304 stainless steel in ozonated 0.5 N NaCl. *Corrosion*, 48(12):970–975, 1992.
- [46] M. Fabbicino and G. V. Korshin. Changes of the corrosion potential of iron in stagnation and flow conditions and their relationship with metal release. *Water Research*, 62:136–146, 2014.
- [47] J. C. Velázquez, J. C. Cruz-Ramirez, A. Valor, V. Venegas, F. Caleyó, and J. M. Hallen. Modeling localized corrosion of pipeline steels in oilfield produced water environments. *Engineering Failure Analysis*, 79]:216–231, 2017.
- [48] R. P. W. M. Jacobs, R. O. H. Grant, J. Kwant, J. M. Marqueine, and E. Mentzer. Composition of produced water from shell operated oil and gas production in the north sea. In *Produced water*, pages 13–21. Springer, 1992.
- [49] M Iannuzzi, E. Hornus, and M. Salasi. Crevice corrosion. *ASTM-books*, pages 1–74, 2019.
- [50] ASTM International. *G48-11(2015) Standard Test Methods for Pitting and Crevice Corrosion Resistance of Stainless Steels and Related Alloys by Use of Ferric Chloride Solution*. ASTM International, West Conshohocken, PA, 2015.
- [51] ASTM International. *150-18 Standard Test Method for Electrochemical Critical Pitting Temperature Testing of Stainless Steels and Related Alloys*. ASTM International, West Conshohocken, PA, 2018.
- [52] ASTM Standard. *G61-86 Standard Test Method for Conducting Cyclic Potentiodynamic Polarization Measurements for Localized Corrosion Susceptibility of Iron-, Nickel-, or Cobalt-Based Alloys*. ASTM Standard, 1986 (Reapproved 2018).
- [53] T. Bellezze, G. Giuliani, and G. Roventi. Study of stainless steels corrosion in a strong acid mixture. Part 1: cyclicpotentiodynamic polarization curves examined by means of an analytical method. *Corrosion Science*, 130:113–125, 2018.
- [54] S. Esmailzadeh and H. Aliofkhaezai, M. Sarlak. Interpretation of cyclic potentiodynamic polarization test results for study of corrosion behavior of metals: A review. *Protection of Metals and Physical Chemistry of Surfaces*, 54(5):976–989, 2018.
- [55] C. J. Park and Y. H. Lee. Initiation and repassivation of crevice corrosion of type 444 stainless steel in chloride solution. *Metals and Materials International*, 10(5): 447–451, 2004.
- [56] M. Iannuzzi. How to determine pitting and repassivation potentials. <https://www.aboutcorrosion.com/2014/04/13/howto-determine-pitting-and-repassivation-potentials/>, 2014. Accessed: 18.12.2019.





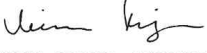


- [57] G. S. Frankel. Pitting corrosion. *ASM Handbook*, 13S:237, 2008.
- [58] F. Westad. Introduction to experimental design. Camo Analytics, 2019. DOE Workshop at Equinor Porsgrunn, Norway.
- [59] G. W. Oehlert. A first course in design and analysis of experiments. Retrieved from the University of Minnesota Digital Conservancy, <http://hdl.handle.net/11299/168002>, 2010. Accessed: 10.04.2020.
- [60] D. C. Montgomery. *Design and Analysis of Experiments*. John Wiley & Sons, Inc., Hoboken, NY, 9th edition, 2017.
- [61] E. Bardal. *Corrosion and protection*. Springer, London, UK, 2004.
- [62] L Chen, J. Hu, X. Zhong, Q. Zhang, Y. Zheng, Z. Zhang, and D. Zeng. Corrosion behaviors of Q345R steel at the initial stage in an oxygen-containing aqueous environment: Experiment and modeling. *Materials*, 11:1–19, 2018.
- [63] E. E. Stansbury and R. A. Buchanan. *Fundamentals of Electrochemical Corrosion*. ASM International, Materials Park, Ohio, 2000.
- [64] M. K. Sawford, B. G. Ateya, A. M. Abdullah, and H. W. Pickering. The role of oxygen on the stability of crevice corrosion. *J. Electrochem. Soc.*, 149(6):B198–B205, 2002.
- [65] W. Lynes. The oxygen concentration cell as a factor in the localized corrosion of metals. *J. Electrochem. Soc.*, 103(8):467–474, 1956.
- [66] R. D. Angal. *Principles and Prevention of Corrosion*. Alpha Science International, Oxford, United Kingdom, 2010.
- [67] H. H. Uhlig, D. N. Triadis, and M. Stern. Effect of oxygen, chlorides, and calcium ion on corrosion inhibition of iron by polyphosphates. *J. Electrochem. Soc.*, 102(2):259–266, 1955.
- [68] S. H. Mameng, A. Bergquist, and E. Johansson. Corrosion of stainless steel in sodium chloride brine solutions. *NACE Corrosion*, pages 1–12, 2014.
- [69] X. Yue, L. Zhang, D. Li, H. Honda, M. Lu, Z. Wang, and X. Tang. Effect of traces of dissolved oxygen on the passivation stability of super 13Cr stainless steel under high CO<sub>2</sub>/H<sub>2</sub>S conditions. *International Journal of Electrochemical Science*, 12:7853–7868, 2017.
- [70] Z. Feng, X. Cheng, C. Dong, L. Xu, and Li. X. Effects of dissolved oxygen on electrochemical and semiconductor properties of 316L stainless steel. *Journal of Nuclear Materials*, 407(3):171–177, 2010.
- [71] S. D. Kapusta. Oxygen reduction on stainless steels in aerated brines. In *Corrosion 2004*, pages 1–18, USA, 2004. NACE International. Conference Paper.
- [72] S. Wang, D. Liu, N. Du, Q. Zhao, S. Liu, and J. Xiao. Relationship between dissolved oxygen and corrosion characterization of X80 steel in acidic soil simulated solution. *International Journal of Electrochemical Science*, 10:4393–4404, 2015.

- [73] ISO 21457. *Petroleum, petrochemical and natural gas industries - Materials selection and corrosion control for oil and gas production systems*. International Organization for Standardization, 2010.
- [74] S. Olsen and J. I. Skar. Materials selection for oil and gas production systems – use of ISO 21457. In *Corrosion 2013*, pages 1–12, USA, Texas, 2013. NACE International. Conference Paper.
- [75] N. Larché, P. I. Nice, C. H. Van Der Zwaag, T. Nesse, L. Scoppio, H. Amaya, Y. Matsuda, M. Fiocchi, and M. Thierry. Evaluation of the corrosion risk of duplex stainless steel UNS S82551 in treated seawater injection service. *NACE International*, pages 1–19, 2017.
- [76] M Duparc, J. I. Skar, and S. M. Hesjevik. OCP vs. DO. Equinor unpublished data.
- [77] ASTM International. *G5-14e1 Standard Reference Test Method for Making Potentiodynamic Anodic Polarization Measurements*. ASTM International, West Conshohocken, PA, 2014.
- [78] *Development of new method to characterize the durability of stainless steels to crevice attack in natural and treated seawaters (CREVCORR)*. European Union Fifth Framework Programme (GROWTH type), 2000–2003. Ref: G5RD-CT-2000-00139.
- [79] U. Kivisäkk, B. Espelid, and D. Féron. *Methodology of Crevice Corrosion Testing for Stainless Steels in Natural and Treated Seawaters: (EFC 60)*, chapter 4.1 Optimisation of Test Parameters of Importance for Crevice Corrosion Testing, pages 17–20. Maney Publishing, 2010.
- [80] Alicona. Infinitefocus. <https://www.alicon.com/products/infinitefocus/>. Accessed: 28.05.2020.
- [81] Imagej downloads. <https://imagej.net/Downloads>. Accessed: 09.12.2019.
- [82] S. H. Mamen, R. Pettersson, and J. Y. Jonson. Limiting conditions for pitting corrosion of stainless steel EN 1.4404 (316L) in terms of temperature, potential and chloride concentration. *Materials and Corrosion*, 68(3):272–283, 2017.
- [83] A. Igual Muñoz, J. García Antón, S. López Nuévalos, J. L. Guiñón, and V. Pérez Herranz. Corrosion studies of austenitic and duplex stainless steels in aqueous lithium bromide solution at different temperatures. *Corrosion Science*, 46(12):2955–2974, 2004.
- [84] P. T. Jakobsen and E. Maahn. Temperature and potential dependence of crevice corrosion of AISI 316Lcd stainless steel. *Corrosion Science*, 43(9):1693–1709, 2001.
- [85] L. Peguet and A. Gaugain. Localized corrosion resistance of duplex stainless steels: methodology and properties; a review paper. *Revue de Métallurgie*, 108(4):231–243, 2011.

# A Appendix

## A.1 Material certificate AISI 316L samples

|  |   |  |                               |  |       |  |   |   |   |       |  |
|--|---|--|-------------------------------|--|-------|--|---|---|---|-------|--|
|   |   | <b>INSPECTION CERTIFICATE 3.1</b><br>DIN EN 10204 3.1                  |                               | Certificate No.<br>Zeugnis Nr.<br>N° du certificat<br><b>749747/001</b>  |       | Page<br>Seite<br>Page<br><b>1 (01)</b>                             |   |   |   |       |  |
| Delivery address, Empfänger, Lieu de livraison<br><b>SALES OPS SWEDEN</b><br><b>FL CONSIGNÉE</b><br><b>ABRAMSONS VÄG 2</b><br><b>635 10 ESKILSTUNA</b><br><b>SVERIGE</b>               |   |  |                               | <b>OUTOKUMPU NORDIC AB</b><br><br><b>PO BOX 1134</b><br><b>631 80 ESKILSTUNA</b><br><b>SVERIGE</b>   |       |  |   |   |   |       |  |
| Requirements, Anforderungen, Exigences<br><b>EN 10088-4:2009</b><br><b>AD 2000 W2, W10 &amp; EN 10028-7:2007</b><br><b>ASTM A240/A240M</b><br><b>ASME SA-240/SA-240M II A ED. 2015</b> |   |  |                               | Our Order No.<br>Unser Auftrag Nr.<br>Notre commande n°<br><b>300394759</b>  |       | Your order, Ihre Bestellung, Votre commande<br><b>101178 / CDF</b> |   |   |   |       |  |
| Product, Erzeugnisform, Produit<br><b>SHEET, STAINLESS STEEL</b>   |   |  |                               | Mark of Manufacturer<br>Zeichen des Lieferwerkes<br>Signe de producteur<br>outokumpu    |       | Process<br>Er schmelzungsart<br>Mode de fusion<br><b>AOD</b>       | Inspector's stamp<br>Zeichen d. Sachverst.<br>Poicon de l'expert<br> |   |   |       |  |
| Grade, Werkstoff, Nuance<br><b>1.4432 1.4436 TYPE 316L</b>   |   |  |                               | Tolerances Toleranzen, Tolérances<br><b>EN ISO 9445-2</b>  |       |  |   |   |   |       |  |
| Marking, Kennzeichnung, Marquage<br><b>1.4432 2B</b>   |   |  |                               | Marks, Versandzeichen, Marques   |       |  |   |   |   |       |  |
| Line<br>Reihe<br>Ligne   | Item<br>Position<br>Poste   | Charge-test No.<br>Schmelz-Probé Nr.<br>Coulée n°                      | Size, Abmessungen, Dimensions |  |       | Quantity<br>Stückzahl<br>Nombre                                    | Weight, Gewicht, Poids  | Finish<br>Ausführung<br>Fini<br>EN/ASTM | <br>14<br>0045-CPR-0567   |       |  |
| 1  | 1   | 63388 4  | 2,0 X 1500 X 3000 MM          |  |       | 30   | 2098 KG   | 2B                                      |   |       |  |
| Charge no.<br>Schmelz Nr.<br>Coulée n°   |   | Chemical composition, Chemische Zusammensetzung, Composition chimiques |                               |  |       |  |   |   |   |       |  |
|  |   | C %  | Si %                          | Mn %   | P %   | S %  | Cr %  | Ni %                                    | MO %  | N %   |  |
| 63388  |   | 0,018  | 0,46                          | 1,29   | 0,034 | <.001  | 17,0  | 10,6                                    | 2,52  | 0,052 |  |
| Line<br>Reihe<br>Ligne   | Mechanical properties, Mechanische Eigenschaften, Caractéristiques mécaniques |  |                               | Tensile test, Zugversuch, Essai de traction  |       |  |   |   |   |       |  |
|  | Sample ID<br>Proben ID<br>Echantillon   | Rp0.2<br>MPa   | Rp1.0<br>MPa                  | Rm<br>MPa  | %     | A50<br>%   | A80<br>%  | Hardness<br>Härte, Duraté<br>HBW        | <b>ISO 6892-1:2009 A224</b><br><b>SAMPLES PERPENDICULAR TO</b><br><b>THE ROLLING DIRECTION</b><br><br><b>APPROVED ACC. TO</b><br><b>AD2000-W0 WITH</b><br><b>VERIFICATION OF THE</b><br><b>UNIFORMITY OVER THE</b><br><b>STRIP LENGTH. CERTIFIED</b><br><b>ACC. TO PED 2014/68/EU BY</b><br><b>TUV NORD REG. NO. 0045.</b><br><b>DOPS ACC. TO CPR</b><br><b>AVAILABLE ON THE WEB</b><br><b>PAGE BY STEEL NUMBER</b> |       |  |
| 1  | 01  | 298  | 329                           | 614  | 51    | 50   | 158   |   |   |       |  |
|  | 02  | 291  | 322                           | 609  | 52    | 51   | 155   |   |   |       |  |
| Identify test, Verwechslungsprüfung, Contrôle d'identification   |   |  |                               | OK   |       |  |   |   |   |       |  |
| Sizes, Abmessungen, Dimensions   |   |  |                               | OK   |       |  |   |   |   |       |  |
| Surface, Oberfläche, Surface   |   |  |                               | OK   |       |  |   |   |   |       |  |
| Test of intergran. corros. Prüfung auf interkrist. Korros. Test de corros. intercris.  |   |  |                               | OK   |       |  |   |   |   |       |  |
| EN ISO 3651-2 A: OK  |   |  |                               |  |       |  |   |   |   |       |  |
| EN 10088-2:2014/1.4432, 1.4436<br>HEAT TREATMENT 1070 C  |   |  |                               | We certify that the above mentioned products comply with the terms of the order contract.<br>Wir bestätigen, dass die Lieferung den Vereinbarungen der Bestellannahme entspricht.<br>Nous certifions que les produits énumérés ci-dessus sont conformes aux prescriptions de la commande.<br><br>This test certificate is made by controlled ADP-system and is valid without signature.<br>Dieses Zeugnis wurde von einem überprüften Datenverarbeitungssystem erstellt und ist ohne Unterschrift gültig.<br>Ce certificat a été établi par un système informatique contrôlé et est valide sans signature. |       |  |   |   |   |       |  |
|  |   |  |                               | <b>Outokumpu Stainless Oy</b><br><br><br>Authorized inspector<br>Werkssachverständiger<br>Inspecteur autorisé<br><b>MIRVA KUJANSUU</b>  |       |  |   |   |   |       |  |
|  |   |  |                               | FI-95490 Tornio, Finland<br>Tel. +358 16 4521, email certificate.tornio@outokumpu.com,<br>www.outokumpu.com<br>Dornické: Tornio, Finland. Business Identity Code 0823315-9   |       |  |   |   |   |       |  |

## A.2 Material certificate 22% Cr DSS samples



**CERTIFICATE - ZEUGNIS - CERTIFICAT**  
**EN 10204-3.1**  
**2499789-EN**

Invoice No. Page  
 Rechnung Nr. Seite  
 N° de facture Page  
 6610/1000659551 1/1

Business Unit / QCM  
 Avesta Works / Johan Nordström

Date Datum Date  
 17-Apr-2018

Load, Ladung, Charge No  
 DE/168302

Acknowledged ID, Bestätigung, Commande ID  
 6610/300471709

|  |   |   |   |
|--|---|---|---|
| Your ref, Ihre Ref., Votre ref<br>test samples for OSW/Mr Kaschuba.  |   | Requirements, Anforderungen, Exigences<br><b>ASTM A 240M-17</b><br><b>ASME BPVC SEC II PART A SA-240/SA-240M Ed 2017</b><br><b>EN 10088-2:2014</b><br><b>EN 10028-7:2016</b><br><b>NORSOK Standard M-630, Ed 6, MDS D45, Rev 5</b><br><b>ASTM A 480</b> |   |
| Buyer, Besteller, Acheteur<br>Outokumpu Nirosta GmbH<br>Oberschlesienstr. 16<br>DE 47807, Krefeld<br>GERMANY |   |   |   |
| Consignee, Empfänger, Lieu de livraison<br>Outokumpu Nirosta GmbH  |   |   |   |
| Mark of Manufacturer<br>Zeichen des Lieferwerkes<br>Signe de producteur<br>                                  | Process<br>Erschmelzungsart<br>Mode de fusion<br><b>E+AOD</b> | Inspector's stamp<br>Zeichen des Sachverständigen<br>Poicon de l'expert<br>   | Grade, Werkstoff, Nuance<br>Outokumpu Forta DX 2205<br>UNS S31803<br>UNS S32205<br>1.4462 |

Product, Erzeugnisform, Produit  
 Stainless Steel Cold Rolled, Coil-Plate  
 finish 2E, pickled, cut edge

| Line<br>Reihe<br>Ligne | Item<br>Position<br>Poste | Heat-Lot No<br>Schmelze-Lot Nr<br>Coulée n° - Lot No | Size<br>Abmessungen<br>Dimensions | Pieces<br>Stückzahl<br>Nombre | Quantity / Unit<br>Menge / Einheit<br>Quantité / Unité |
|------------------------|---------------------------|--|-----------------------------------|-------------------------------|--|
| 1                      | 1                         | 580907-004   | 3,00 X 1500 X 3000 mm             | 9                             | 948 KG   |

| Chemical composition – Chemische Zusammensetzung – Composition chimiques |      |     |      |      |      |       |      |      |      |     |      |      |
|--|------|-----|------|------|------|-------|------|------|------|-----|------|------|
|  | C    | Si  | Mn   | P    | S    | Cr    | Ni   | Mo   | Nb   | Cu  | Co   | N    |
| Heat   | .018 | .34 | 1.33 | .027 | .001 | 22.53 | 5.68 | 3.15 | .011 | .30 | .130 | .178 |

Radioactive contamination check acc. IAEA recommendations: **Approved**

| Test results – Prüfergebnisse – Résultats des essais (1N/mm <sup>2</sup> = 1 MPa) F = Front – Anfan – Debut B = Back – Ende – Fin T = Transverse – Quer – Travers |      |        |        |       |    |    |     |     |      |  |
|---|------|--------|--------|-------|----|----|-----|-----|------|--|
| Test Ref  | Temp | RP 0.2 | RP 1.0 | RM    | A5 | 2" | HB  | FEH |      |  |
|   | °C   | N/MM2  | N/MM2  | N/MM2 | %  | %  | HB  | %   |      |  |
| Min   | +20  | 500    | 700    | 20    | 25 |    |     |     | 35.0 |  |
| Max   |      |        |        | 950   |    |    | 293 |     | 55.0 |  |
| F T   | +20  | 648    | 732    | 852   | 32 | 31 | 251 |     | 49.0 |  |
| B T   |      | 638    | 726    | 846   | 33 | 32 | 249 |     | 50.0 |  |

**Corrosion acc. EN ISO 3651-2C: Approved**  
**PREN: Cr + 3,3Mo + 16N = 35.8**  
**Heat treatment / Solution annealed: Material temp minimum 1120 °C / Quenched (forced air + water)**  
**All supplied items fulfill the heat treatment requirements, including time, temperature and speed, acc. to the qualified procedure**  
**QTR No: 2205 - 2014**  
**Corrosion acc. ASTM G 48-A 30 °C - 24H: Approved**  
**Intermetallic phases and/or precipitates acc. to NORSOK MDS D45 Rev. 5: No indications**  
**Steel grade verification (PMI-spectroscopic): Approved**  
**Marking, visual insp. and gauge measurement: Approved**  
**Certified acc. Pressure Equipment Directive (2014/68/EU) by TÜV CERT-Certification body for pressure equipment of the TÜV NORD Systems; notified body, reg-no. 0045.**  
**Microstructure acc to ASTM A 923-A: Approved**

Outokumpu Stainless AB Telephone: + 46 (0)226 811 73  
 Business Area Europe Fax: + 46 (0)226 816 46  
 AVESTA WORKS V.A.T no: SE556001874801  
 SWEDEN  
 Regoffice: Stockholm SWEDEN, Regno: 556001-8748

This material is found to comply with order requirements  
  
 Joakim Johansson  
 Authorized Inspector

### A.3 Percentage crevices

Selected images obtained with IFM and analyzed in ImageJ are presented in Figure A.1-A.4, to illustrate how the crevice percentage at each test condition were obtained. For this purpose, images of samples tested at test condition 6 and 12 were chosen.

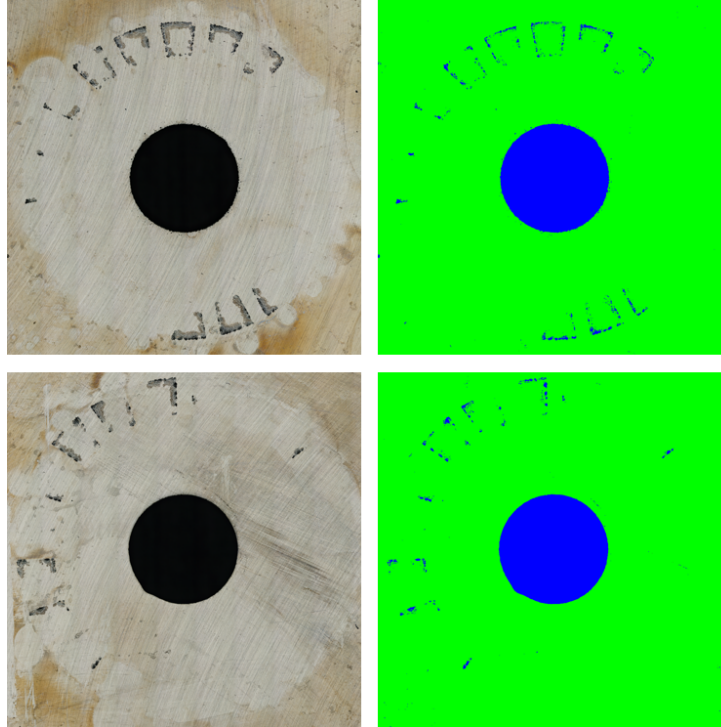


**Figure A.1:** Images of the surface of a 316L sample (both sides) tested in electrolyte with 5000 ppm chloride and pH 5.7-7.0 at 95 °C, obtained with IFM and analyzed in ImageJ.

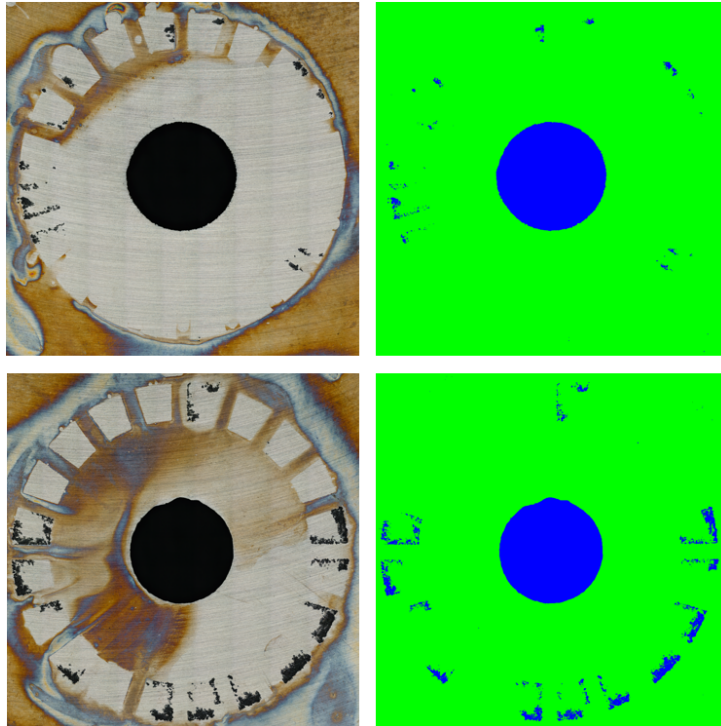


**Figure A.2:** Images of the surface of a DSS sample (both sides) tested in electrolyte with 5000 ppm chloride and pH 7.2-8.2 at 95 °C, obtained with IFM and analyzed in ImageJ.

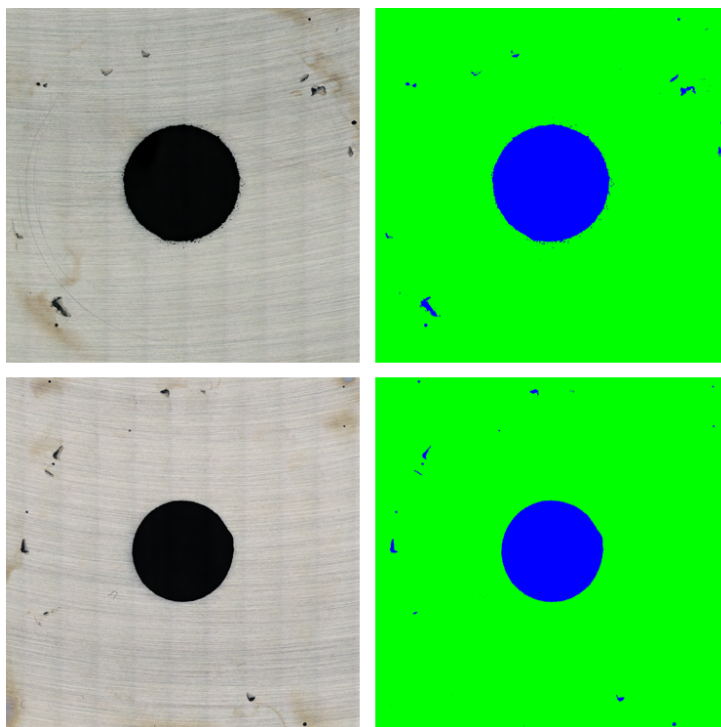


**Figure A.3:** Images of the surface of a 316L sample (both sides) tested in electrolyte with 120 000 ppm chloride and pH 4.8-5.0 at 95 °C, obtained with IFM and analyzed in ImageJ.

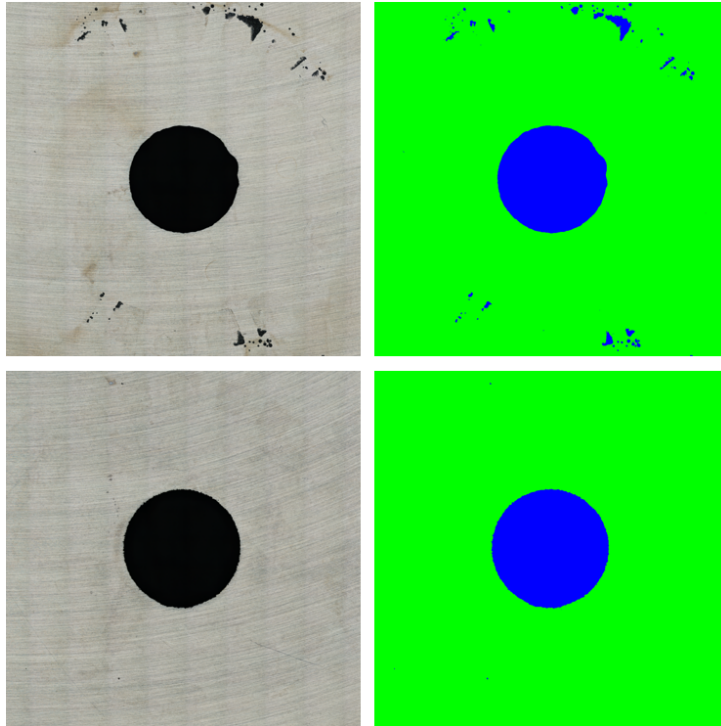


**Figure A.4:** Images of the surface of a DSS sample (both sides) tested in electrolyte with 120 000 ppm chloride and pH 4.9-5.0 at 95 °C, obtained with IFM and analyzed in ImageJ.

